

# **Probing the origin of two population electron hypotheses in large scale X-ray jet of Active Galaxies**

Thesis submitted to

**University of Calicut**

for the award of the degree of

**Doctor of Philosophy in Physics**

Under the Faculty of Science

by

**Amal Abdulrahman**

Under the guidance of

**Prof. P. A. Subha**



**Postgraduate and Research Department of Physics**

**Farook College (Autonomous)**

Farook College Rd, Kozhikode, Kerala, India-673632

**May, 2024**

*This thesis is dedicated to..*



**JISHNA E**

*1996-2024 and then Forever...*

Health Researcher | Economic Demographer | Social Scientist  
International Institute for Population Sciences, Mumbai

*Farook College's proud alumni whose charm, warmth and kindness shall remain in us forever. Through her perseverance, Jishna not only broke the barriers of her own circumstances but also paved the way for others to follow. From the quiet outskirts of her village in Feroke, she became a force of change, proving that even the humblest beginnings could lead to extraordinary achievements. Her story was a testament to the power of education, resilience, and the belief that one person could indeed change the world.*



Postgraduate and Research Department of Physics  
Farook College (Autonomous)  
Kozhikode, Kerala, India -673632


---

## Certificate

Certified that the work presented in this thesis titled "**Probing the origin of two population electron hypotheses in large scale X-ray jet of Active Galaxies**" is a bonafide work done by **Mrs. Amal Abdulrahman** under my guidance in the Postgraduate and Research Department of Physics, Farook College (Autonomous), University of Calicut and that this work has not been included in any other thesis submitted previously for the award of any degree.

Place: Farook College

Date:

  
Prof. P. A. Subha  
Supervising Guide

PG & Research Department of Physics  
Farook College (Autonomous)

**Prof. P. A. SUBHA**  
**Research Supervisor**  
**Department of Physics**  
**Farook College**  
**Kozhikode - 673 632.**



Postgraduate and Research Department of Physics  
Farook College (Autonomous)  
Kozhikode, Kerala, India -673632

---

## Candidate's Declaration

I hereby declare that the work presented in the thesis entitled "**Probing the origin of two population electron hypotheses in large scale X-ray jet of Active Galaxies**" is based on the original work done by me under the guidance of **Prof. P. A. Subha** and has not been included in any other thesis submitted previously for the award of any degree. The contents of the thesis are undergone plagiarism check using "iThenticate" software at C.H.M.K. Library, University of Calicut, and the similarity index found within the permissible limit. I also declare that the thesis is free from AI generated contents.

**Amal Abdulrahman**

**Place: Farook College**

**Date:**

**Prof. P. A. Subha**  
**Supervising Guide**

**PG & Research Department of Physics**  
**Farook College (Autonomous)**

**Prof. P. A. SUBHA**  
**Research Supervisor**  
**Department of Physics**  
**Farook College**  
**Kozhikode - 673 632.**





Postgraduate and Research Department of Physics  
Farook College (Autonomous)  
Kozhikode, Kerala, India -673632

---

## Certificate

This is to certify that the corrections and suggestions recommended by the adjudicators have been incorporated in the thesis of Amal Abdulrahman, research scholar under my supervision and that the contents in the thesis and the soft copy are one and same.

Place: Farook College

Date:

Prof. P. A. Subha

Supervising Guide

PG & Research Department of Physics

Farook College (Autonomous)

**Prof. P. A. SUBHA**  
**Research Supervisor**  
**Department of Physics**  
**Farook College**  
**Kozhikode - 673 632.**

# Acknowledgements

---

This thesis is the outcome of a dream of myself and many people who love and care for me. I would like to thank every person who was indeed a part and parcel of this *Journey*.

I am extremely happy to express my deepest love and gratitude to my mentor and guide **Prof. P. A. Subha**, who has been pivotal from the very beginning of my Ph. D. Journey. It was her goodwill and support that motivated me to complete this thesis on time. Subha ma'am is inspirational with her dedication to science and research. Her vision for the Department of Physics of Farook College is evident through her engagements. Developing the department into a research department, she has published papers in multitudes of fields. I am privileged and lucky enough to be your last and final official Ph. D. student. Dear ma'am, this journey was rich with every conversation we had within the subject and out of it and I enjoyed every moment throughout.

I am grateful to my collaborator **Dr. Sunder Sahayanathan** (Scientist, Astrophysical Science Division, BARC Mumbai) for all his commitments and dedication to the successful completion of this thesis. My wish to pursue research in astrophysics came to reality through your guidance. I am extremely happy that I got you as my mentor to teach the basics of research and astrophysics. You were always available for every communication, even though we worked online. I feel lucky to be your student and your wisdom and expertise have helped me a lot. You are as energetic as an AGN Sunder and your energy will surely spread across space and time.

The Journey of Ph. D. for me is like planting a seed. The seed needs fertile soil and favourable conditions for its proper growth. Day by day, the seed develops and sprouts into a seedling. The consistent care makes it grow into a fully developed plant. Dear Sunder and Subha ma'am, your care and unwavering support made it possible for me to complete my Ph. D. I wish, the plant we have grown together shall blossom and spread fragrance. I hope the time and energy spent by both of you shall become useful and fruitful.

I express my immense gratitude to Dr. Aysha Swapna (Principal, Farook College) and Dr. Naseer K. A (Former Principal, Farook College) for all the technical and academic help during the course. My sincere gratitude to Prof. M. M. Musthafa (Department of Physics, University of Calicut), Prof. Mohamed Shahin Thayyil (Department of Physics, University of Calicut) and Prof. T Mohamed Nishad (Convener, Research promotion council, Farook College) for their guidance and support. I extend my sincere gratitude to Mr. Midhun Shah (Head, Dept. of Physics) and Dr. Sulfikkarali N. K. (Research Coordinator of the Department) for their constant support and cooperation. My special thanks to Dr. K. K. Abdulla (Former HOD, Department of Physics) for his encouragement and warm presence. I am also thankful to all the faculty members, technical staff and other staff in the department. The time spent in the staff room, the food and tea we had together, the conferences and programs we conducted.. all added colours to my life spent at the campus. Special thanks to Mr. Mohammed Naseef (Faculty, Dept. of Physics), for being my companion in the astro research.

I wish you the very best for your future research endeavour.

I offer my thanks to Bhabha Atomic Research (BARC), Mumbai and Inter-University Center for Astronomy and Astrophysics (IUCAA), Pune for their vision and support in promoting astrophysics research in colleges and universities. The IUCAA-sponsored AGN meeting held at Farook College, during August 2022 was a milestone in my research life giving the opportunity to interact and collaborate with faculties and researchers across the nation working in my area of research. My special thanks to Gulab Dewangan (Professor, IUCAA), C. S Stalin (Professor, IIA) along with Sunder Sahaynathan for facilitating a fruitful workshop as a part of the AGN meeting. I happily remember the moments shared with all the faculties, researchers and students during the meeting. Farook College has indeed benefitted from these activities and we hope the college will flourish in astro research in upcoming years. My special thanks to Dr. Vaidehi S Paliya (IUCAA) for his academic interactions whenever needed. You were always available for any communication and your insights shared during your visit to Calicut University were helpful. I thank Frank Reiger (Heidelberg University, Germany), Nilay Bhat (BARC Mumbai) and Dr. Subhir Bhattacharya (BARC Mumbai) for their valuable insights during my research. Special mention to Dr. Zahoor Malik for the input and support during the second published work. I also thank all the unknown reviewers for their valuable comments and suggestions regarding the published works. I gratefully acknowledge the financial support (UGC-JRF) provided by the University Grants Commission (UGC), Govt of India.

I am thankful to my co-researchers (at the Dept. of Physics, Farook College) Remi, my sister Thasneem, Jubeer sir and Sreeshna for all the help and support throughout the course. Your company was integral to the successful completion of my thesis. It was really interesting to share each other our research works, even though we worked on different fields in physics. I wish you all a bright future ahead. The 'Blazar group' was the most helpful gang during my research. Every discussion and every meeting we had indeed helped me grow in the subject. A group of people spread across the nation, working in the same field under the guidance of Sunder brought diversity and exchange of culture in the group. More than a group, at times it felt like a family. Zahir Shah, Pranju, Rukaiya, Sitha, Baheeja, Amina, Habeeb, Zahoor, Aaqib, Athar, Soumya, Athira, Sajad, Reshma and Naseef.. I feel fortunate to connect with all of you. The trips we had during conferences were memorable and added colours to this Journey. My special thanks to Rosey Di and Alvin (Mumbai) for their love and support. Thanks to Susmita Das (Presidency University, Kolkata) and Janhavi Bhagel (NCRA, Pune) for the fond memories during the IAU meeting at Kathmandu. I also remember my project students who helped me understand my subject better. I thank all researchers in various departments at Farook College especially my friends at the Commerce department. I thank all the teaching faculties, and all the staffs at office, library, informatics centre, and all other staff at Farook College. I express my love to all the students at Farook College with whom I had a great time interacting on various things. Special mention to Vibez music club and Team TEDxFarook College.

It would not be complete, without thanking my family who have been my greatest support system throughout life. I thank my Mom ( mother-in-law) Jameela for taking all the pains to take care of my two children throughout this journey. Without her support and kindness, this wouldn't

have been possible for me. I love you to the core and let's conquer the heights together. At this point, I remember two important people in my life. My mother (Umma) Asiya and father (Uppa) Abdulrahman. At the age of 4, when I was only half way learning my swimming, my dad left me alone at one corner of the pond in my home. I still remember the struggle I had in reaching the other end of the pond, but I managed to swim and then I knew, I learned swimming. His courage and trust helped me achieve everything in my life. My mother on the other hand taught me the lessons to move ahead in life, whatever the barriers. You both are my best support pillars. I thank my dad (father-in-law), Abdulla for all the positive vibes he created at home in conquering heights after my marriage. Your presence made my journey easier. My love and hugs to Salva, Manna, Hiba, Julu, Jawad, Nooh, Noor, Nezam, Musheer, Adil and little Eminu for being the support system. Special mention to Chirag family for being a second home during the submission of my thesis. Happily remembering everyone at Othayoth family. Gafoorka, Shaheertha, Najmecha, Naseerka, Nisi, Alikka, Sini, Shahidka and every kid starting from Najad, Nashwah, Naveed, Hamdan, Hawwah, Rayyan, Neha, Maryam, Haadi, Fathima, Nabhan, Hannah and Haathim. Your support and encouragement were instrumental in completing this thesis. Special thanks to Noorjamma, Jasmin and Wardah for their heartfelt support. Remembering Kunjuppa, Muthu and the whole Variankandy family.

My intense love and hugs to my partner, Javed Islam. We knew the journey would be tough. But your push was the first step in achieving the UGC-JRF and the research career started with that. Your positive outlook towards life made this journey accelerated. The two children we grew together during this time add colours. Jibu and Asbi, Ummi love you a lot. I dunno how much trouble you had during these years. But, Ummi tried her best to spend quality time with you. I saw you growing independent and supporting Ummi to achieve her dreams. You both are my best babies. Much Love.

**(Amal Abdulrahman)**

# Contents

---

<b>Dedication</b>	<b>ii</b>
<b>Acknowledgments</b>	<b>vi</b>
<b>List of Publications</b>	<b>xii</b>
<b>List of Conference Presentations</b>	<b>xiii</b>
<b>Abstract</b>	<b>xv</b>
<b>Malayalam Abstract</b>	<b>xvi</b>
<b>List of Figures</b>	<b>xvii</b>
<b>List of Tables</b>	<b>xix</b>
<b>List of Abbreviations</b>	<b>xx</b>
<b>1 Active Galactic Nuclei and their Jets</b>	<b>1</b>
1.1 Active Galactic Nuclei . . . . .	1
1.1.1 Morphology of AGN . . . . .	2
1.1.2 Classification of AGN . . . . .	3
1.1.3 Unification of AGN . . . . .	5
1.2 The jet of AGN . . . . .	7
1.2.1 Superluminal motion . . . . .	7
1.3 AGN Jet on smaller and larger scales . . . . .	8
1.3.1 The Inner jet . . . . .	9
1.4 Large-scale Jets of AGN . . . . .	10
1.4.1 AGN Jet Features . . . . .	10
1.4.2 The Jet Pool . . . . .	13
1.5 Thesis Outline . . . . .	14
<b>2 Particle Distribution and Emission Mechanism in AGN Jets</b>	<b>16</b>
2.1 Introduction . . . . .	16
2.2 Particle Distribution in AGN jets . . . . .	17
2.2.1 Power-law Particle Distribution . . . . .	17

2.2.2	Particle distribution under synchrotron losses . . . . .	18
2.3	Non-thermal Radiative Mechanisms . . . . .	20
2.3.1	Synchrotron emission . . . . .	20
2.3.2	Inverse-Compton Radiation . . . . .	23
2.4	Relativistic Beaming & Jet Assymetry . . . . .	27
2.5	Equipartition Magnetic Field . . . . .	29
2.6	EBL and Gamma-ray Attenuation . . . . .	30
<b>3</b>	<b>High Energy Emissions from Large scale Jets of AGN: Recent Advancements</b>	<b>31</b>
3.1	Introduction . . . . .	31
3.2	The Resolved Jet: Multiwavelength Observations and Theories . . . . .	32
3.2.1	The Emission Mechanism . . . . .	32
3.2.2	<i>Fermi</i> /LAT observations: Implications on IC/CMB emission model . . . . .	34
3.2.3	The spine-sheath model for AGN Jets . . . . .	35
3.2.4	Positional offset . . . . .	35
3.2.5	X-ray Variability . . . . .	37
3.2.6	Polarization . . . . .	38
3.3	MHD Simulations of large-scale jet . . . . .	38
3.4	VHE emission from large-scale jets . . . . .	39
3.5	Conclusions . . . . .	39
<b>4</b>	<b>Advection of Accelerated Electrons in Radio/X-ray Knots of AGN Jets</b>	<b>40</b>
4.1	Introduction . . . . .	40
4.2	The Two-Population Model . . . . .	41
4.2.1	Synchrotron Spectrum . . . . .	43
4.3	Results and Discussion . . . . .	45
<b>5</b>	<b>X-ray Emission from Large Scale Jets of AGNs at High Redshifts</b>	<b>50</b>
5.1	Introduction . . . . .	50
5.2	Source Selection . . . . .	51
5.2.1	J1510+5702 (GB 1508+5714) . . . . .	51
5.2.2	J1421-0643 (PKS 1418-064) . . . . .	52
5.3	Electron Acceleration and Advection Model . . . . .	52
5.4	Results and Discussion . . . . .	53
<b>6</b>	<b>Probing IC/CMB Interpretation for the X-ray Knots of AGN through VHE Observations</b>	<b>58</b>
6.1	Introduction . . . . .	58
6.2	Source Selection . . . . .	59
6.3	Emission Models . . . . .	61
6.3.1	Source Parameters . . . . .	62

6.4	Results and Discussion . . . . .	63
<b>7</b>	<b>Summary and Recommendations</b>	<b>71</b>
7.1	Summary . . . . .	71
7.2	Recommendations . . . . .	73
	<b>Bibliography</b>	<b>75</b>

# List of Publications

---

## Publications relevant to this thesis:

- [1] **Amal A. Rahman**, Sunder Sahayanathan, and P. A Subha, 2022, Advection of Accelerated Electrons in Radio/X-ray Knots of AGN Jets, Monthly Notices of Royal Astronomical Society (MNRAS), Volume 515, Pages 1410–1415 (Rahman et al., 2022).
  - [2] **Amal A. Rahman**, Sunder Sahayanathan, Zahoor Malik and P. A Subha, 2023, Probing IC/CMB interpretation for the X-ray knots of AGN through VHE observations, Monthly Notices of Royal Astronomical Society (MNRAS), Volume 524, Pages 3335-3343 (Rahman et al., 2023).
  - [3] **Amal A. Rahman**, Sunder Sahayanathan and P. A Subha, 2024, X-ray emission from large scale jets of AGNs at high redshifts, Journal of High Energy Astrophysics (JHEAP), Volume 42, Pages 156-162 (Rahman et al., 2024a).
  - [4] **Amal A. Rahman**, Sunder Sahayanathan and P. A Subha, 2024, Electron acceleration and advection model for the high energy emission from the large scale jet of AGNs, Proceedings of Science HEPRO VIII(2024) 017 (Rahman et al., 2024b).
-



# List of conference presentations

---

## International

- [1] 30th Young Scientists' Conference on Astronomy and Space Physics, Kyiv, Ukraine, *oral presentation*, April 2024.
- [2] HEPRO VIII: High Energy Phenomena in Relativistic Outflows, Institut d'Astrophysique de Paris and Observatoire de Paris, Paris, France, *oral presentation*, October 2023.
- [3] International Astronomical Union Symposia 375: The Multimessenger Chakra of Blazar Jets, Kathmandu, Nepal, *oral presentation*, December 2022.

## National

- [1] Young Astronomers Meet-2024, Christ (Deemed to be University), Bangalore, Karnataka, *poster presentation*, March 2024.
- [2] International Conference on Theoretical and Experimental Physics, Farook College(Autonomous), Kozhikode, Kerala, *oral presentation*, February 2024.
- [3] Sullamussalam International Conference, Sullamussalam Science College, Areekode, Kerala, *oral presentation*, February 2024.
- [4] 9th Regional Astronomy Meeting, MCNS, Manipal Academy of Higher Education, Karnataka, *oral presentation*, January 2024.
- [5] 41st meeting of Astronomical Society of India (ASI), IIT Indore, *oral presentation*, March 2023.
- [6] IUCAA sponsored Three Day Southern Regional Astronomers Meeting on 'Research in Astronomy: Opportunities and challenges', RSET, Cochin, Kerala, *oral presentation*, February 2023.
- [7] AMALIT International Conference, Amal College of Advanced Studies, Nilambur, Malappuram, Kerala, *oral presentation*, January 2023.
- [8] IUCAA sponsored 4th National Conference on "High Energy Emission from AGN", Farook College, Calicut University, *oral presentation & LOC*, August 2022.
- [9] 40th meeting of Astronomical Society of India (ASI), IIT Roorkee, Uttarakhand, *poster presentation*, March 2022.

[10] Theoretical Aspects of High Energy Emission from AGN, Kashmir University, Srinagar, *invited talk*, July 2021.

[11] International Conference on Theoretical and Experimental Physics, Farook College(Autonomous), Kozhikode, kerala, *poster presentation*, February 2020.

---

# Abstract

---

Active Galactic Nuclei (AGN) are one of the most energetic sources in the universe. These galaxies host a supermassive black hole at their centre. Most of the AGNs are observed to host a relativistic jet that can extend up to kilo-parsec/mega-parsec scales and is powered by supermassive black holes. In this thesis, we study the hard X-ray emission from the kilo-parsec scale jet of active galactic nuclei, which cannot be attributed to the synchrotron emission mechanism from the electron distribution responsible for the radio/optical emissions. Alternatively, two interpretations are proposed; the inverse Compton scattering of cosmic microwave background photons by the relativistic synchrotron-emitting electrons in the jet (IC/CMB model) or synchrotron emission from a second electron population. The IC/CMB interpretation of X-ray emission, on the other hand, suggests significant gamma-ray emission from the kilo-parsec scale jets. However, the non-detection of gamma-ray flux from these galaxies by *Fermi*/LAT disfavors this interpretation rather advocates the second population of electrons as a possible cause for X-ray emission. Here, we explore the possible origin of the second population, particularly considering a scenario where the high-energy electrons from the sites of particle acceleration advect into the jet medium. This advected electron distribution is significantly different from the accelerated electron distribution and satisfies the requirements of the second electron population. We find that the multi-spectral component (MSC) emission from these large-scale AGN jets can be explained by the synchrotron emission from the accelerated and the advected electron distribution. Nevertheless, the IC/CMB model was accepted for sources at higher redshifts due to the increase in CMB energy density with redshift. Recent gamma-ray flux upper limits of high redshift sources, namely J1510+5702 and J1421-0643, do not comply with the IC/CMB predictions. Application of the electron acceleration and advection models to these sources can interpret their MSC jet emission. Irrespective of the *Fermi* results, further stringent constraints on the IC/CMB model can be put forth from the very high energy (VHE) observations. The IC/CMB emission model is extrapolated to VHE and then compared with the sensitivity of the upcoming Cherenkov Telescope Array Observatory. We find candidate sources whose IC/CMB spectrum falls within its detection threshold, and future observations by CTAO have the potential to validate the high-energy emission process from the large-scale AGN jet.

**Key words:** galaxies: active, galaxies: jets, X-rays: galaxies, radiation mechanisms: non-thermal, gamma-rays: galaxies

## സാരം

പ്രബന്ധത്തിലെ ഏറ്റവും ഊർജ്ജ കേന്ദ്രീകൃത സ്രോതസ്സുകളിൽ ഒന്നാണ് ആക്ടിവ് ഗാലക്സിക് ന്യൂക്ലിയസ് അഥവാ എ.ജി.എൻ. ഈ ഗാലക്സികളുടെ കേന്ദ്രത്തിൽ ഒരു സൂപ്പർമാസീവ് തമോഗർത്തം നിലനിൽക്കുകയും അതിന്റെ ഫലമായി നിരവധി എ.ജി.എൻ-കളിൽ കിലോ-പാർസെക്/മെഗാ-പാർസെക് സ്കെയിലുകളിൽ വരെ നീണ്ടു നിൽക്കുന്ന ആപേക്ഷിക ജെറ്റുകൾ നിരീക്ഷിക്കപ്പെടുകയും ചെയ്യുന്നു. ഈ പ്രബന്ധത്തിൽ എ.ജി.എന്നിലെ കിലോ-പാർസെക് ജെറ്റിൽ നിന്നും പ്രവഹിക്കുന്ന ഹാർഡ് എക്സ്റേ എമിഷനാണ് പഠനവിധേയമാക്കിയത്. റേഡിയോ/ഒപ്റ്റിക്കൽ പ്രസാരണത്തിന് കാരണമായ ഇലക്ട്രോൺ വിതരണത്തിൽ നിന്നുള്ള സിൻക്രോട്രോൺ എമിഷൻ പ്രക്രിയയിലൂടെ കിലോ-പാർസെക് ജെറ്റുകളിൽ നിരീക്ഷിച്ചു വരുന്ന ഹാർഡ് എക്സ്റേ പ്രസാരണം വിശദീകരിക്കുക സാധ്യമല്ല. നിലവിൽ രണ്ട് മാതൃകകളാണ് ഈ നിരീക്ഷണത്തെ വിശദീകരിക്കാനായി മുന്നോട്ടുവെക്കപ്പെട്ടിട്ടുള്ളത്. ജെറ്റിൽ നിന്നുള്ള ആപേക്ഷിക സിൻക്രോട്രോൺ-എമിറ്റിംഗ് ഇലക്ട്രോണുകൾ വഴി കോസ്മിക് മൈക്രോവേവ് പാശ്ചാത്തല ഫോട്ടോണുകളുടെ വിപരീത കോംപൂൺ വിസരണം (IC/CMB മോഡൽ) ആണ് ഇതിൽ ഒന്നാമത്തേത്. മറ്റൊരു ഇലക്ട്രോൺ പോപ്പുലേഷനിൽ നിന്നുള്ള സിൻക്രോട്രോൺ പ്രസാരണം ആണ് രണ്ടാമത്തേത്. ഒന്നാമത്തെ മാതൃക പ്രകാരം കിലോ-പാർസെക് ജെറ്റുകളിൽ നിന്നും നിർണ്ണായകമായ ഗാമാ കിരണങ്ങളുടെ പ്രസാരണത്തെ മുൻകൂട്ടി കാണാൻ കഴിയുന്നു. എന്നാൽ, വർഷങ്ങൾ നീണ്ട ഫെർമി/LAT ഗാമാ-റേ ടെലിസ്കോപ്പുകൾ വഴിയുള്ള നിരന്തര നിരീക്ഷണങ്ങളിൽ ഈ ഗാലക്സികളിൽ നിന്നുള്ള ഗാമാ കിരണങ്ങൾ കാണാൻ കഴിഞ്ഞില്ല. ഇത് നിരീക്ഷിക്കപ്പെടാത്തത് മേൽപ്പറഞ്ഞ നിഗമനത്തെ സാധൂകരിക്കുന്നില്ല. അതിനാൽ മറ്റൊരു അനുമാനമായ, രണ്ടാം ഇലക്ട്രോൺ പോപ്പുലേഷൻ പ്രസാരണം എക്സ്റേ എമിഷന് കാരണമാകുന്നു എന്ന സൂചന നൽകുന്നു. ജെറ്റിലെ കണികാത്വരണമുള്ള സ്ഥാനങ്ങളിൽ നിന്ന് പുറപ്പെടുന്ന ഉന്നതോർജ്ജമുള്ള ഇലക്ട്രോണുകൾ ജെറ്റ് മാധ്യമത്തിലൂടെ പ്രവാഹകൈമാറ്റം ചെയ്യുന്ന അവസ്ഥ ഉണ്ട്. ഈ പ്രത്യേകസാഹചര്യം പരിഗണിച്ച് കൊണ്ടുള്ള രണ്ടാം പോപ്പുലേഷന്റെ ഉത്ഭവം പ്രതിപാദിക്കുന്ന ഒരു പുതിയ മാതൃക ഈ പ്രബന്ധം മുന്നോട്ടുവെക്കുന്നു. ഈ പ്രവാഹകൈമാറ്റത്തിലെ ഇലക്ട്രോൺ വിതരണം, ത്വരിതപ്പെടുത്തപ്പെട്ട ഇലക്ട്രോൺ വിതരണത്തിൽ നിന്നും തികച്ചും വ്യത്യസ്തമാണ്. മാത്രമല്ല, ഇത് രണ്ടാം ഇലക്ട്രോൺ പോപ്പുലേഷന്റെ ഉപാധികൾ പാലിക്കുന്നുവെന്നും പഠനം തെളിയിക്കുന്നു. ഇത്തരത്തിൽ രൂപാന്തരപ്പെട്ട രണ്ട് ഇലക്ട്രോൺ വിതരണത്തിൽ നിന്നുമുള്ള സിൻക്രോട്രോൺ പ്രസാരണമാണ് എ.ജി.എന്നിലെ ജെറ്റുകളിൽ നിന്ന് വരുന്ന റേഡിയോ-ഒപ്റ്റിക്കൽ-ഹാർഡ് എക്സ്റേ പ്രസാരണത്തിന് കാരണമാകുന്നത് എന്ന് ഗവേഷണം വിശദീകരിക്കുന്നു. എന്നിരുന്നാലും, റെഡ് ഷിഫ്റ്റിന് അനുസൃതമായുള്ള CMB ഊർജ്ജസാന്ദ്രതയിലെ മാറ്റം വിദൂരങ്ങളിൽ (കൂടിയ റെഡ് ഷിഫ്റ്റ്) നിലനിൽക്കുന്ന സ്രോതസ്സുകൾക്ക് IC/CMB മാതൃക സീകാര്യമാക്കുന്നു. എന്നാൽ, J1510+5702, J1421-0643 തുടങ്ങിയ വിദൂര സ്രോതസ്സുകളിൽ നിന്നുള്ള ഗാമാ-റേ ഫ്ലൂക്സിൻ നിലവിലെ ഉയർന്ന പരിധികൾ IC/CMB മാതൃകയിലെ പ്രവചനങ്ങൾ പാലിക്കുന്നില്ല. ഈ സ്രോതസ്സുകളിൽ, മേൽപറഞ്ഞ രണ്ടു ഇലക്ട്രോൺ മാതൃകകൾ വിധേയമാക്കുമ്പോൾ അവയുടെ റേഡിയോ-ഒപ്റ്റിക്കൽ-എക്സ്റേ പ്രസാരണം വിശദീകരിക്കാൻ സാധിക്കും. ഫെർമി ഗാമാ-റേ ടെലിസ്കോപ്പ് നിരീക്ഷണങ്ങൾക്ക് പുറമെ, IC/CMB മാതൃകയെ കൂടുതൽ ആഴത്തിൽ പഠിക്കാൻ വളരെ ഉയർന്ന ഗാമാ-റേ ഊർജ്ജ (VHE) നിരീക്ഷണങ്ങളിൽ നിന്ന് സാധ്യമാകുന്നു. IC/CMB മാതൃക VHE ലേക്ക് എക്സ്റാപൊളേറ്റ് ചെയ്യുകയും തുടർന്ന് ചെറൻകോവ് ടെലിസ്കോപ്പ് അറേ ഒബ്സർവേറ്ററിയുടെ (CTAO) സംവേദനക്ഷമതയുമായി താരതമ്യപ്പെടുത്തുന്നതിലൂടെ IC/CMB സ്നേഹം CTAO യുടെ നിരീക്ഷണ പരിധിക്കുള്ളിൽ വരുന്ന സ്രോതസ്സുകളെ കണ്ടെത്തുന്നു. ഇതുവഴി, ലാർജ് സ്കെയിൽ എ.ജി.എൻ ജെറ്റിൽ നിന്നുള്ള ഉന്നതോർജ്ജ പ്രസാരണ പ്രക്രിയയെ വിശദീകരിക്കാൻ CTAO യുടെ ഭാവി നിരീക്ഷണങ്ങൾക്ക് കഴിയുന്നു.

# List of Figures

---

1.1	Normal galaxy verses AGN . . . . .	1
1.2	Morphology of AGN . . . . .	2
1.3	AGN Taxonomy . . . . .	4
1.4	Structure of AGN . . . . .	6
1.5	AGN Unification . . . . .	6
1.6	Superluminal motion . . . . .	7
1.7	The dependance of apparent velocity on viewing angle . . . . .	8
1.8	Montage of M87 on all scales . . . . .	9
1.9	Illustration of Unified models of AGN . . . . .	11
1.10	The FR I and FR II radio galaxies . . . . .	12
1.11	The knots of AGN jets . . . . .	12
1.12	Pictor A observed at different wavebands . . . . .	13
1.13	Bent jet of NGC 1265 . . . . .	13
1.14	X-shaped jet of XRG J0725+5835 . . . . .	14
2.1	The schematic of particle distribution . . . . .	18
2.2	Synchrotron power function . . . . .	21
2.3	Synchrotron spectrum from a power-law distribution of electron . . . . .	23
2.4	Inverse Compton scattering . . . . .	24
2.5	Single and dual jet . . . . .	28
2.6	The schematic of pair-production . . . . .	30
3.1	SED of the knots of M 87 and 3C 273 . . . . .	33
3.2	Modelling the SED of the jet of PKS 1136-135 . . . . .	34
3.3	Comparison of IC/CMB model with <i>Fermi</i> gamma-ray flux upper limits . . . . .	35
3.4	Transverse jet profile of 3C 273 . . . . .	36
3.5	Radio/X-ray positional offset of 3C 273 knots . . . . .	37
4.1	The schematic diagram of knot . . . . .	42
4.2	The advected electron distribution at different $R > R_0$ . . . . .	44
4.3	Advected electron population for different $\zeta$ in the case of knot A . . . . .	44
4.4	The electron distribution for the knot A of 3C 273 . . . . .	45
4.5	Observed broadband SEDs of the knots of 3C 273 together with the model curves . . . . .	46
5.1	Observed broadband SED along with model curves . . . . .	54

6.1	Large-scale knots falling within the detection threshold of CTAO . . . . .	64
6.2	Large-scale knots that do not fall within the detection threshold of CTAO . . . . .	65
6.3	Large scale knots that do not fall within the detection threshold of CTAO-continued	66
6.4	Large scale knots that do not fall within the detection threshold of CTAO-continued	67

# List of Tables

---

4.1	Fit parameters of radio-optical-X-ray spectrum of the knots of 3C 273 . . . . .	47
5.1	Model parameters corresponding to Figure 5.1 . . . . .	57
6.1	List of AGNs with Jet Knots/components included in our source list . . . . .	60
6.2	Fit parameters of radio-optical-X-ray spectrum . . . . .	68

# List of Abbreviations

---

<b>3C</b>	Third Cambridge Catalogue of Radio Sources
<b>3FGL</b>	The <i>Fermi</i> /LAT 4-Year Point Source Catalog
<b>4FGL</b>	The <i>Fermi</i> /LAT 8-Year Point Source Catalog
<b>ACIS</b>	Advanced CCD Imaging Spectrometer
<b>AGN</b>	Active Galactic Nuclei
<b>ATNF</b>	Australia Telescope National Facility
<b>BLR</b>	Broad Line Region
<b>BLRG</b>	Broad Line Radio Galaxy
<b>CDQ</b>	Core-dominated Quasar
<b>CTA</b>	Cherenkov Telescope Array
<b>CTAO</b>	Cherenkov Telescope Array Observatory
<b>CXC</b>	Chandra X-ray Center
<b>EBL</b>	Extragalactic Background Light
<b>ESA</b>	European Space Agency
<b>ESO</b>	European Southern Observatory
<b>FR 0</b>	Fanaroff-Riley 0
<b>FR I</b>	Fanaroff-Riley I
<b>FR II</b>	Fanaroff-Riley II
<b>FSRQ</b>	Flat Spectrum Radio Quasar
<b>HESS</b>	High Energy Stereoscopic System
<b>HST</b>	Hubble Space Telescope
<b>IC/CMB</b>	Inverse Compton scattering of Cosmic Microwave Background photons
<b>IXPE</b>	Imaging X-ray Polarimetry Explorer
<b>LAT</b>	Large Area Telescope
<b>LDQ</b>	Lobe-dominated Quasar
<b>LIRA</b>	Low-count Image Reconstruction Algorithm
<b>M 87</b>	Messier 87



<b>M100</b>	Messier 100
<b>MAGIC</b>	Major Atmospheric Gamma-ray Imaging Cherenkov Telescope
<b>MAGN</b>	Misaligned Active Galactic Nuclei
<b>MERLIN</b>	Multi-Element Radio Linked Interferometer Network
<b>MHD</b>	Magnetohydrodynamics
<b>MSC</b>	Multi-spectral Component
<b>NASA</b>	National Aeronautics and Space Administration
<b>NGC</b>	New General Catalogue
<b>NLR</b>	Narrow Line Region
<b>NLRG</b>	Narrow Line Radio Galaxy
<b>NRAO</b>	National Radio Astronomy Observatory
<b>PKS</b>	Parkes Catalogue of Radio Sources
<b>PSF</b>	Point Spread Function
<b>QSO</b>	Quasi Stellar Object
<b>RL</b>	Radio Loud
<b>RQ</b>	Radio Quiet
<b>SED</b>	Spectral Energy Distribution
<b>SMBH</b>	Supermassive Black Hole
<b>SSRQ</b>	Steep Spectrum Radio Quasar
<b>UV</b>	Ultra Violet
<b>VHE</b>	Very High Energy
<b>VLA</b>	Very Large Array
<b>VLBI</b>	Very-long-baseline Interferometry
<b>VERITAS</b>	The Very Energetic Radiation Imaging Telescope Array System

# Chapter 1

## Active Galactic Nuclei and their Jets

---

*I will give you a "celestial multiplication table." We start with a star as the unit most familiar to us, a globe comparable to the sun. Then, a hundred thousand million Stars make one Galaxy; A hundred thousand million Galaxies make one Universe. The figures may not be very trustworthy, but I think they give a correct impression.*

*- Sir Arthur Stanley Eddington*

*The Expanding Universe (Eddington, 1933)*

### 1.1 Active Galactic Nuclei

A galaxy is a gravitationally bound system that consists of stars, stellar remnants, gas, dust, and dark matter. The total luminosity of a normal galaxy is of the order of  $10^{44}$  erg/s. A small fraction of galaxies ( $\sim 5\%$ ) have highly luminous central nuclei with its core luminosity exceeding much greater than  $10^{44}$  erg/s. Such galaxies with very bright central cores that outshine the emission from the rest of their region are termed "Active Galaxies" and their nucleus is called by the name "Active Galactic Nuclei (AGN)".

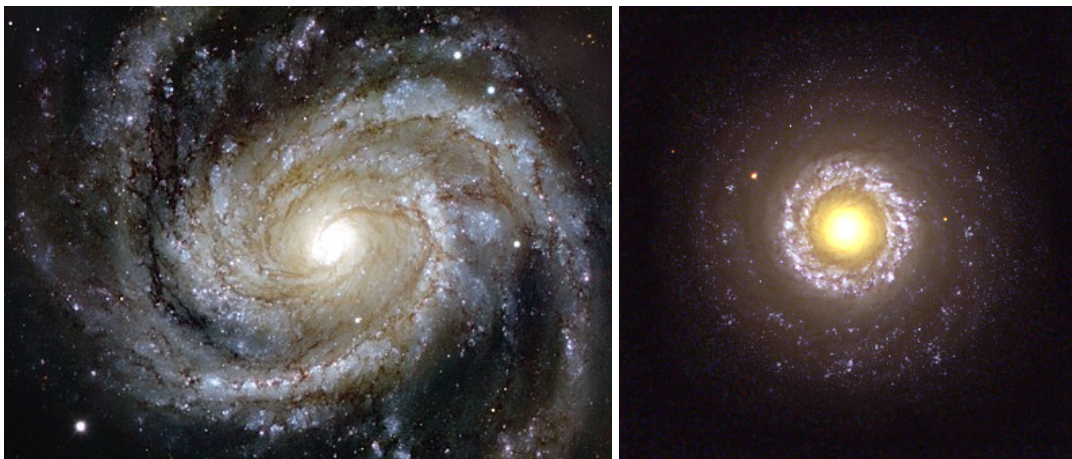


**Figure 1.1:** Left: Normal galaxy Messier 100 (M100). Image credits: ESO. Right: Active galaxy NGC 7742. Image credits: HST.

## 1.1.1 Morphology of AGN

AGNs are diverse in their morphological features. They are observed with differences in their structure and size. However, based on the features that are frequently noticed, the main morphological feature of AGN can be developed as follows:

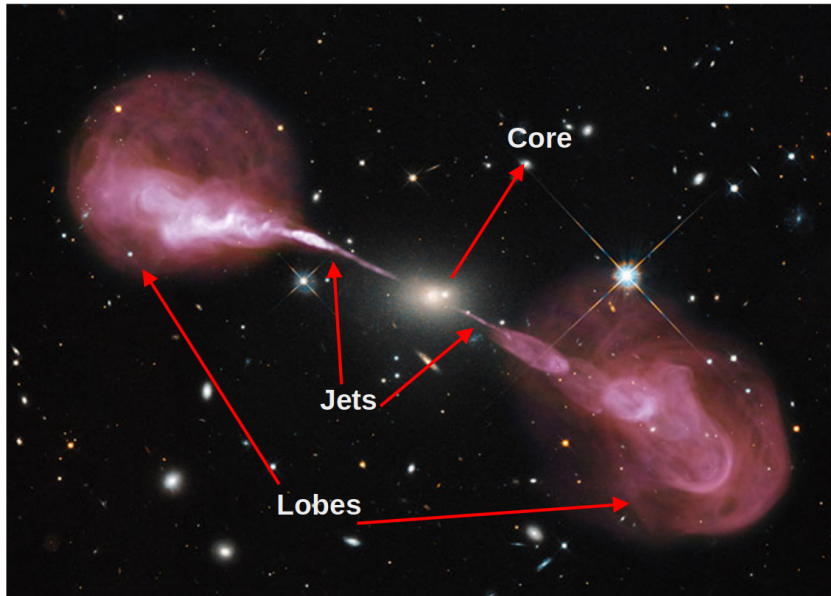


**Figure 1.2:** Radio galaxy Hercules A: Composite image of HST (optical) and VLA (radio) observations.

- **Core**

Cores are the compact and luminous radio component that coincides with the nucleus of the associated active galaxy. Usually, they are unresolved and generally found in all quasars and the majority of radio galaxies. Their power-law spectrum is flat and has an index of less than 0.5.

- **Lobes**

Extended regions of radio emission observed on both sides of the galaxy's nucleus. Lobes occur at large distances from the core up to kilo-parsec to mega-parsec scales. Their spectrum is steep, with an index greater than 0.5. The regions of local intensity maxima found in lobes are called hotspots.

- **Jets**

The region connecting compact core and outer lobes of AGN are called jets. They extend from parsec to mega-parsec scales. The bright emission regions embedded in the jets are called knots.

## 1.1.2 Classification of AGN

The most important source of information about any astronomical object is the light emitted from it. Numerous telescopes collect these photons, and valuable information is extracted. Active galaxies are observed in all wavelengths extending from radio to VHE gamma-rays. This diverse information in varied wavelengths opens windows to different aspects of AGN physics. The tremendous increase in observation has led to a proliferation of AGN classes in recent years. In this scenario, it is essential to dig out the truly inherent and fundamental characteristics of AGNs using the available observations. In the following sections, radio-emitting AGN and their main categories are discussed.

### Radio Quiet and Radio Loud AGN

Based on the ratio of their radio luminosity ( $L_r$ ) to the optical luminosity ( $L_o$ ), the radio-emitting AGNs are broadly categorised as Radio Loud (RL) and Radio Quiet (RQ). Strittmatter et al. (1980) demonstrated this bimodal pattern in the radio loudness of quasars (radio loudness,  $R = \frac{L_r}{L_o}$ ). However, the demarcating value for classification to RL and RQ was controversial for decades. Kellermann et al. (1989) analysed 114 bright quasars, calculated this ratio and confirmed the distribution to be bimodal. According to their classification, RQs have an R-value in the range of 0.1 and 1, whereas, RLs have it between 10 and 1000. Later, Shastri et al. (1993) suggested the R-value of 10, calculating the luminosity of the sources in the 5 GHz and optical B band (4450 Å). Subsequently, several other observations and analyses supported the two population descriptions (Stocke et al., 1992; Goldschmidt et al., 1999; Jiang et al., 2007). However, many studies later found the continuous distribution of  $\log(R)$  without apparent gaps separating RL and RQ AGN (White et al., 2000; Lacy et al., 2001; Wals et al., 2005; Rafter et al., 2009; Bonchi et al., 2013). Even though decades have passed, no clear consensus has been drawn on this dichotomy. Considering the condition  $R \geq 10$ , nearly 10-15% of AGN can be classified as radio-loud. These radio emissions are dominated by the powerful relativistic jets in AGN.

### Types of AGN

Depending on the characteristics of UV/optical spectra, both RL and RQ AGN have been classified as Type 1 and Type 2. The galaxies with bright continua and broad emission lines due to the presence of hot and high-velocity gas fall in the Type 1 AGN. Whereas, AGN that exhibits narrow line emission falls in the Type 2 category. The AGNs with unusual behaviour are categorised as Type 0.

The commonly observed RQ AGN are Seyfert galaxies, first identified by Carl Seyfert in 1943. Seyferts generally have the morphology of spiral galaxies and host a bright nucleus whose luminosity is comparable to the whole galaxy. However, different from quasars, their host galaxies are distinctly observed. Based on the emission lines in their spectra, they are classified as Seyfert I (Type 1) and Seyfert II (Type 2).

- Seyfert I: These Seyfert galaxies emit a strong continuum ranging from far infrared to X-ray. Their spectra have broad emission lines with a width of a few thousand kilometres per second.

Radio Loudness	Optical emission line properties		
	Type 2 (Narrow line)	Type 1 (Broad line)	Type 0 (Unusual)
Radio Quiet	Seyfert 2	Seyfert 1 QSO	
Radio Loud	NLRG { FR I FR II	BLRG SSRQ FSRQ	Blazars { BL Lacs FSRQ
	Decreasing angle to the line of sight $\longrightarrow$		

**Figure 1.3:** A simplified scheme of AGN Taxonomy. Image credits: Padovani (1997)

- Seyfert II: These Seyfert galaxies show weak continuum emissions with narrow emission lines of the order of a few hundred kilometres per second.

The Radio Loud AGN are broadly classified based on their emission properties as Narrow Line (Type 2), Broad Line (Type 1) and Blazars (Type 0). The galaxies with narrow line features are further divided into two based on their radio morphology: Fanaroff-Riley I and II.

- Fanaroff-Riley I (FR I): These sources are extended, featuring lobes, jets, and a core. Their jets are usually symmetric and are found to be fainter at their outer extreme. They are referred to as edge-darkened sources because of this characteristic.
- Fanaroff-Riley II (FR II): Compared to FR I radio galaxies, FR II sources are more luminous and they have knotty jets and lobes with hot spots. The intensity of FR II falls off towards the nucleus and hence they are called edge-brightened sources. They usually have one-sided and well-collimated jets.
- Fanaroff-Riley 0 (FR 0): Recently discovered new types of radio sources, with characteristics comparable to FR I and FR II galaxies. These objects are distinguished by the criterion of their lack of extended radio emission not reaching up to the kpc scale as in FR Is and IIs (Baldi & Capetti, 2009; Baldi et al., 2018). Baldi et al. (2015) finds these sources to be more core-dominated by a factor of 30 larger when compared to FR I. According to Ghisellini (2011), this developing source class is known as 'FR 0' radio galaxies and they have similar nuclear features as FR I galaxies but hundreds of times less power in the extended emission. The FR 0 population dominates radio galaxies in the local universe, outnumbering FR I and II (Baldi et al., 2018).

The Radio Loud Broad-line galaxies comprise Broad Line Radio Galaxies (BLRG) and Radio Quasars. Based on their spectral index values, the Radio Quasars are divided into two: Steep Spectrum Radio Quasar (SSRQ) and Flat Spectrum Radio Quasar (FSRQ).

- Broad Line Radio Galaxies (BLRG): These galaxies have continuum spectra and emission lines that resemble Seyfert 1 galaxies. These galaxies differ from Radio Quasars in their luminosity. BLRGs are less luminous compared to the others.
- Steep Spectrum Radio Quasar (SSRQ): Radio Quasars with their radio spectral index  $\geq 0.5$ .
- Flat Spectrum Radio Quasar (FSRQ): Radio Quasars with their radio spectral index  $\leq 0.5$ .

A few AGNs show unusual spectral characteristics and are classified as Type 0. No radio-quiet sources fall into this category. The peculiar behaviour of these sources is often attributed to the small angle to the line of sight of the AGN jet. The Type 0 AGNs include BL-Lacertae (BL Lac) objects and FSRQs. Both feature common properties like rapid variability, high and variable polarization, superluminal motion, etc. Hence, they are collectively called Blazars.

- BL-Lacertae (BL Lac): Radio-loud AGN that lacks (or found weak) emission or absorption features in their spectrum. They have a strong nuclear continuum with a high degree of polarization, and their spectral continuum extends from radio to  $\gamma$ -ray energies. They show rapid flux variability, with few detected even at TeV energies.

### 1.1.3 Unification of AGN

The observational evidence suggests the presence of a supermassive black hole at the centre of active galaxies. The immediate environment of this blackhole includes tori of dust and gas, which get accreted into it and form the accretion disk. Radiations are emitted in different wavelengths as the matter accretes toward the black hole. Moreover, AGN is observed to host a relativistic jet normal to the disk's plane powered by the supermassive black hole. This highly collimated jet extends to a kilo-parsec/mega-parsec scale distance away from the galaxy's core. The region around the parsec scale distance in the jet produces broader emission lines from AGN and is hence termed a Broad Line Region (BLR), and the region responsible for narrow emission lines is termed the Narrow Line Region (NLR). The broadening considered here is the Doppler broadening, usually associated with the temperature of the material. Figure 1.4 shows the schematic diagram of the structure of an AGN.

Different classes of AGN share many common observational properties, which led to the idea of unifying all these classes as variants of objects belonging to the same population. The orientation hypothesis is the most established theory of AGN Unification. According to it, the observational distinctions between the classes of AGN are due to the difference in orientations of the jet in the sky plane to the line of sight of the observer, as shown in Figure 1.5 (Antonucci, 1993; Urry & Padovani, 1995).

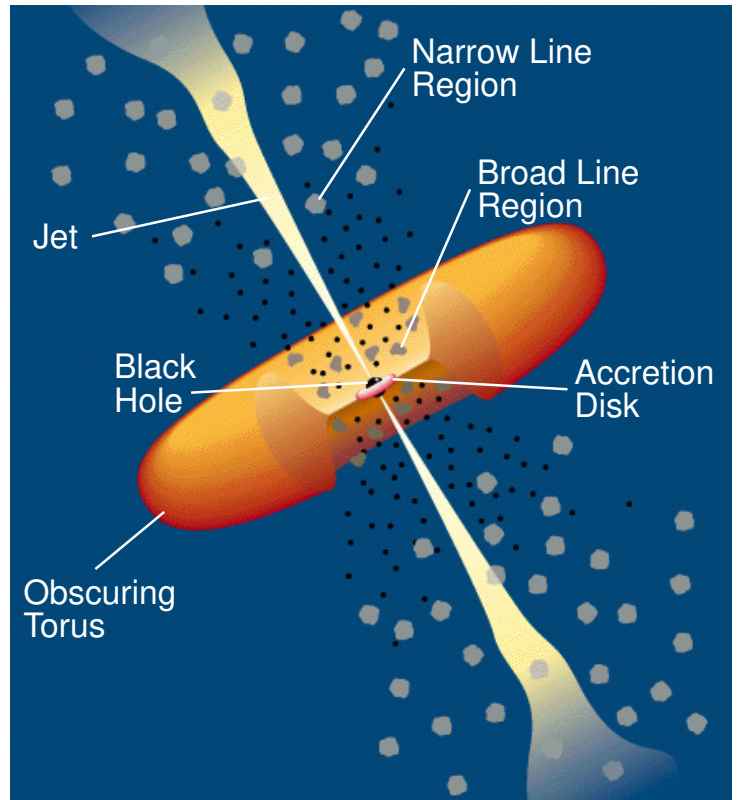


**Figure 1.4:** Schematic diagram of the structure of AGN (Urry & Padovani, 1995). Image Credit: NASA.

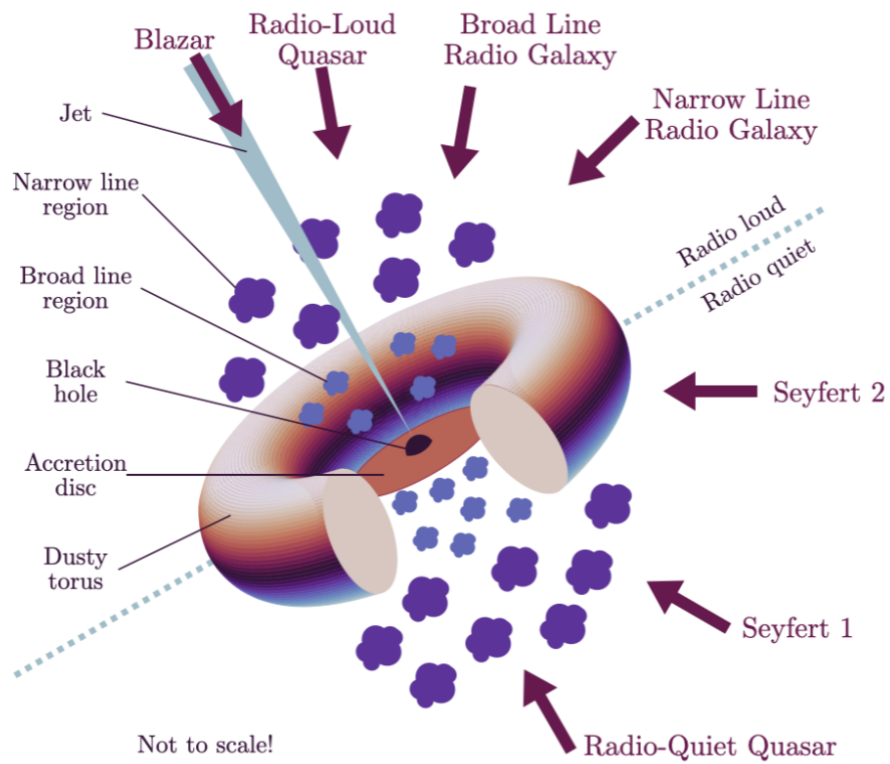


**Figure 1.5:** AGN Unification. Image credits: Urry & Padovani (1995)



## 1.2 The jet of AGN

The region of radiation that connects the central compact core of an AGN to its outer extended lobes is referred to as the jet. Jets can be observed across a wide range of energies, from radio to TeV gamma-rays. They can be one-sided or two-sided and can stretch from just a few parsecs to mega-parsec scales. The primary function of these jets is to transport energetic particles from the nucleus of the AGN to the large-scale radio structures at relativistic velocities. As these collimated jets eject blobs of plasma, they appear to move at superluminal velocities, as a result of the highly relativistic motion of the blobs viewed along the direction of travel.

### 1.2.1 Superluminal motion

In many AGNs, it has been observed that jet components move at a velocity greater than that of light. This phenomenon, known as superluminal motion, is attributed to the bulk relativistic flow at an angle close to the line of sight (Rees, 1966). Let us consider a blob ejected with a velocity of 'v' from a stationary source.  $\theta$  is the angle of ejection with respect to the observer's line of sight at 'O', as shown in Figure 1.6. If the blob emits a signal for a duration  $\delta t$ , measured from the frame of the

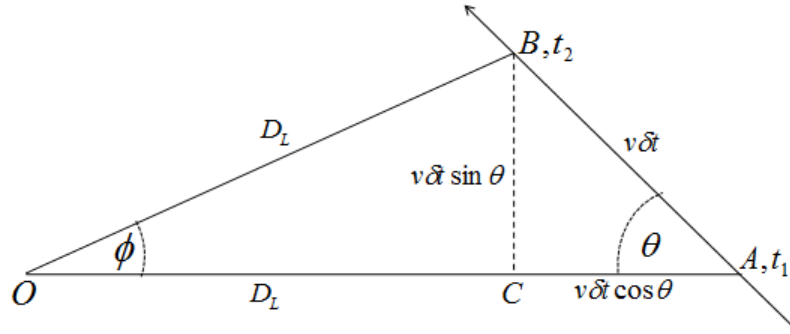


**Figure 1.6:** Diagram for deriving the relativistic explanation of superluminal motion in AGN jets; image credits: Wikipedia.

stationary source, then the distance travelled by the blob is  $v\delta t$ . At time  $t_1$ , a light ray is emitted by the blob from point A, and another ray leaves the blob at time  $t_2 = t_1 + \delta t$  from point B. These rays from A and B reach the observer at O during the time  $t_1^*$  and  $t_2^*$ , respectively. The angle  $\phi$  is small enough that distances OB and OC can be considered equal. Then, time  $t_1^*$  and  $t_2^*$  can be calculated as

$$t_1^* = t_1 + \frac{D_L + v\delta t \cos \theta}{c} \quad (1.2.1)$$

$$t_2^* = t_2 + \frac{D_L}{c} \quad (1.2.2)$$

The time interval  $\delta t^*$  between the observations is given by,

$$\delta t^* = t_2^* - t_1^* = t_2 - t_1 - \frac{v\delta t \cos \theta}{c} = \delta t(1 - \beta \cos \theta) \quad (1.2.3)$$



where  $\beta = \frac{v}{c}$ . The distance  $BC \approx \phi D_L = v \delta t \sin \theta$ . Therefore, apparent transverse velocity along BC is given by,

$$v_T = \frac{\phi D_L}{\delta t^*} = \frac{v \sin \theta}{1 - \beta \cos \theta} \quad (1.2.4)$$

And hence,

$$\beta_a = \frac{v_T}{c} = \frac{\beta \sin \theta}{1 - \beta \cos \theta} \quad (1.2.5)$$

Figure 1.7 gives insight into the dependence of apparent velocity on the viewing angle and the actual

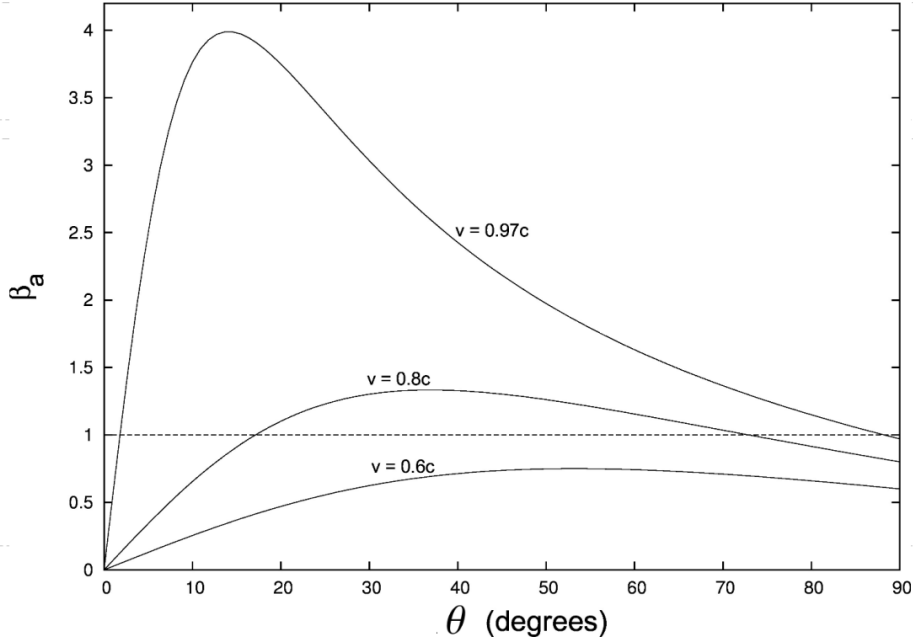


**Figure 1.7:** Dependence of apparent velocity of a relativistically moving blob (in units of  $c$ ) on the viewing angle of the observer. The actual speeds of the blob corresponding to the curves are  $0.6c$ ,  $0.8c$  and  $0.97c$ .

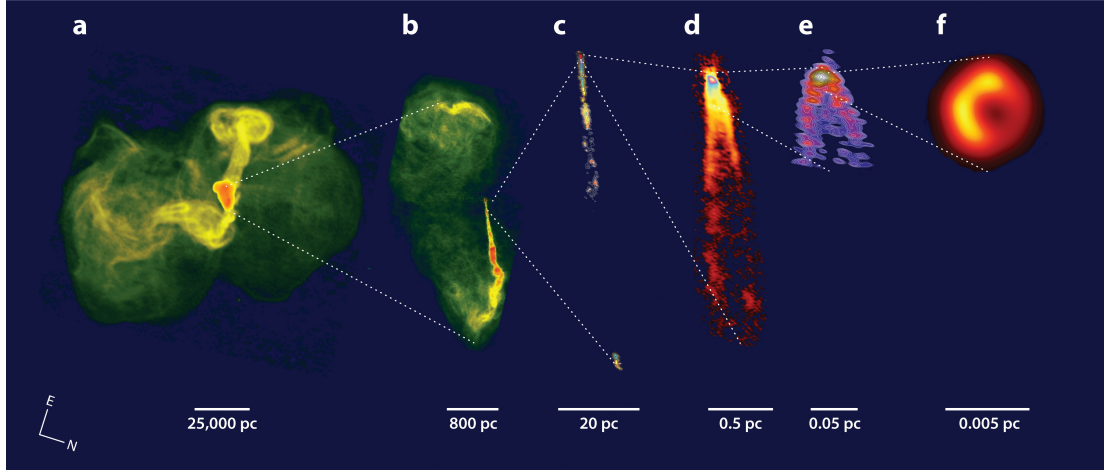
speed of the blob. It is evident that the apparent speed exceeds the velocity of light when the blob moves at relativistic speeds and closer to the line of sight.

### 1.3 AGN Jet on smaller and larger scales

The jets of Active Galactic Nuclei (AGN) act as channels that allow matter and energy from the central engine of the galaxy to flow outwards. These jets extend from a distance of a few parsecs to a few mega-parsecs, and understanding the physical processes associated with their formation, structure, and propagation poses a significant challenge in astrophysics (Begelman et al., 1984). The collimation, complex dynamics of the jet and its interaction with the environment as it propagates from smaller to larger scales is not known very well.

Two major models have been proposed for the production of AGN jets. The first model is the Blandford-Znajek process, which suggests the formation of jets around a spinning supermassive black hole by extracting energy from its rotation (Blandford & Znajek, 1977). The second model,

known as the Blandford-Payne mechanism, suggests that the production of jets is driven by magneto-hydrodynamic winds associated with the inner regions of the accretion disk (Blandford & Payne, 1982). Recent observational advancements have made it possible to observe the jet in all possible angular scales. The properties and behaviour of jets differ significantly on smaller and larger scales, and the connection between these regions is yet to be explored. Figure 1.8 illustrates the structure of the M 87 jet from kilo-parsec to milli-parsec scales.



 Blandford R, et al. 2019.  
Annu. Rev. Astron. Astrophys. 57:467–509

**Figure 1.8:** Montage of M87 (FR I radio galaxy) on all scales. (a) Lobe jet and outer lobes; (b) galaxy jet and inner lobes; (c) black hole jet; (d) innermost jet; (e) jet launching region near supermassive black hole; and (f) inner accretion disk and black hole. For detailed descriptions see Blandford et al. (2019).

The radio-loud or jetted AGNs (Padovani, 2017), with their strong relativistic jets, are among the most powerful sources in the universe. The jets are observed in ranges of energies from radio to VHE gamma rays. The last decade witnessed remarkable advancements in the multi-wavelength observations of AGNs because of the *Fermi* gamma-ray space telescope and ground-based gamma-ray telescopes like H.E.S.S., MAGIC and VERITAS. The observational evidence has advanced our understanding of their multi-wavelength spectral energy distribution (SED), variabilities and polarization. This has significantly constrained the emission models associated with AGNs.

### 1.3.1 The Inner jet

The highly polarised and rapidly variable emissions from the blazars are generally attributed to the relativistic jet at the inner region of AGN pointing close to the observer’s line of sight (Urry & Padovani, 1995). This non-thermal emission is produced close to the central black hole at distances less than 0.1 pc and extends from radio to TeV gamma-ray energies. Blazars are also proposed candidate sources for the origin of astrophysical neutrinos (Mannheim, 1993; Tavecchio & Ghisellini, 2015). At smaller jet angles, relativistic effects amplify the non-thermal emission over the thermal radiation from the BLR or disk. The jet flow is accelerated and collimated close to the

black hole (distance  $\sim 10^{-4}$  pc), and starts to dissipate power at distances  $\sim 0.1$  pc. Further ahead of this region (distance  $> 1$  pc), the jet propagates with small dissipation. The blazar emissions are generally assumed to be from this inner jet of AGNs.

The sub-milliarcsecond-scale imaging of AGN at radio wavelengths has broadened our understanding of the parsec-scale jet structures and magnetic field evolution (Blandford et al., 2019). These findings have been critical in driving the magnetohydrodynamics (MHD) simulations, which has greatly improved our understanding of jets. The dynamic nature of jet flow coupled with the complicated interactions between hydrodynamics, magnetic fields, radiation transfer and curved spacetime have made numerical simulations an increasingly important tool for theoretical investigation of jet (Davis & Tchekhovskoy, 2020; Komissarov & Porth, 2021).

## 1.4 Large-scale Jets of AGN

The giant collimated outflows of plasma (or jet) can extend up to kpc/Mpc from the core of AGN. Curtis (1918) described the first jet discovered as "*a curious straight ray lies in a gap in the nebulosity in p.a. 20 degrees, apparently connected with the nucleus by a thin line of matter*". This extended feature from the elliptical galaxy M 87 was a curiosity until the advent of radio telescopes with good angular resolution and sensitivity in the 1960s. The radio observations carried out later exhibited the extended structures with jets and hotspots from many other galaxies as well. Even after half a century of intensive studies based on the radio observations of these sources, no consensus is reached on the composition, formation, and collimation of these jets.

Active galaxies can be classified based on the orientation of their relativistic jets to the line of sight of the observer as described in the unification model (sec.1.1.3). According to this model, blazars are those active galaxies whose jets are aligned towards the observer. Because of this orientation, the galaxy's bright central region is observed in all wavebands with extreme properties. They exhibit variability in different timescales and are thought to be sources of ultra-high energy cosmic rays. The active galaxies whose jet is oriented at a larger angle to the observer's line of sight are categorised as Misaligned Active Galactic Nuclei (MAGN). These galaxies reveal their extended jet morphology as opposed to the compact core-dominated shape of blazars. Fig.1.9 shows the orientation of the jet in blazars and MAGNs.

The radio-loud MAGNs are further classified as FR I (edge-darkened) and FR II (edge-brightened) based on the distance of the brightest point from the central core (refer 1.1.2). The examples of FR Is are M 87, 3C 15, 3C 31, M 84, Cen A etc. A few examples of MAGNs that fall in the category of FR II are 3C 17, 3C 33, 3C 111, 3C 265 etc. Fig. 1.10 shows the image of FR I and FR II type AGNs.

### 1.4.1 AGN Jet Features

#### Lobes

The region at the extremes of the jet, where the jets terminate and release their energy and

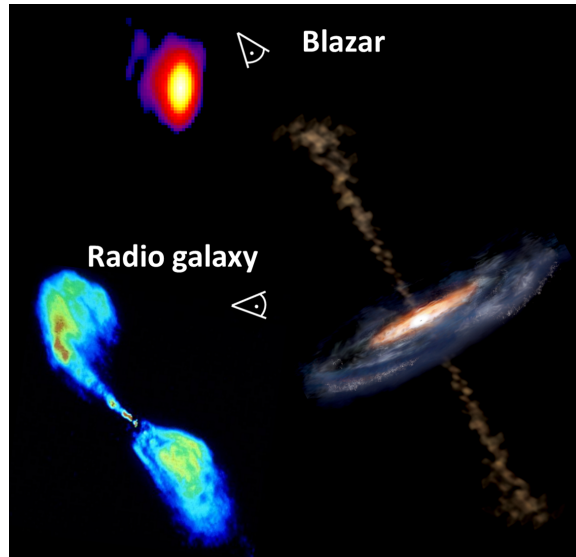


**Figure 1.9:** Illustration of AGN unification model: Blazars Vs Misaligned Active Galactic Nuclei (MAGN). The AGN with supermassive black hole, accreting disk and perpendicular jets appear different when viewed at different angles. Image adapted from Urry & Padovani (1995); Burns & Price (1983).

momentum into the ambient intergalactic medium is called Lobes (see Fig 1.2). The radio spectrum of these lobes is usually steep and polarized, suggesting synchrotron emission and efficient cooling of relativistic particles.

### Hot spots

Hot spots (see Fig. 1.10) are regions of enhanced emission in the lobes that are often collinear with the central core, giving the jet its edge-brightened nature. These hot spots are considered a defining characteristic of Fanaroff Riley class I & II radio sources (Carilli et al., 1995). In the regions of the hotspots, the jet hits the ambient medium and converts the bulk kinetic energy of the beam into random energy through the shock formed at the collision. The energetic particles are accelerated at the shock and diffuse from the hot spot to the lobe.

### Knots

The bright emission regions embedded along the length of the AGN jet are called Knots (see the well resolved knots of 3C 273 in optical wavebands namely; A1, A2 etc. in Fig. 1.11). Their enhanced brightness is usually attributed to the acceleration of charged particles at the shock present in the jet and the emissions associated with it. Knots are observed in radio, optical and X-ray energies. Many of them exhibit superluminal motion, which is often considered as the evidence for their relativistic flow. Most of the knots have strongly polarized emission, with polarisation angles usually perpendicular to the jet axis. Their spectrum is non-thermal (power-law) in nature and this suggests synchrotron emission from the relativistic distribution of charged particles as the origin of low energy (radio-to-optical) radiation in the knots.

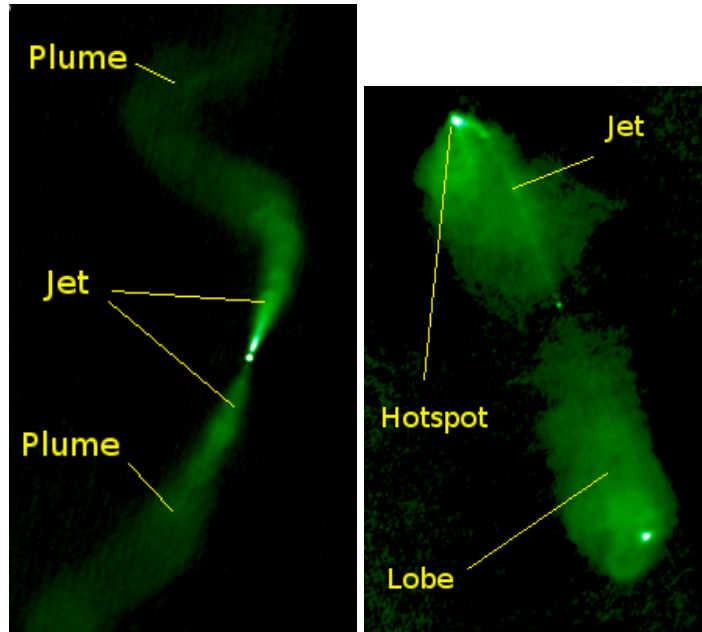


**Figure 1.10:** The FRI and FR II radio galaxies. Left: FRI radio galaxy 3C 31. Right: FR II radio galaxy 3C 98. Image credits: Wikipedia.

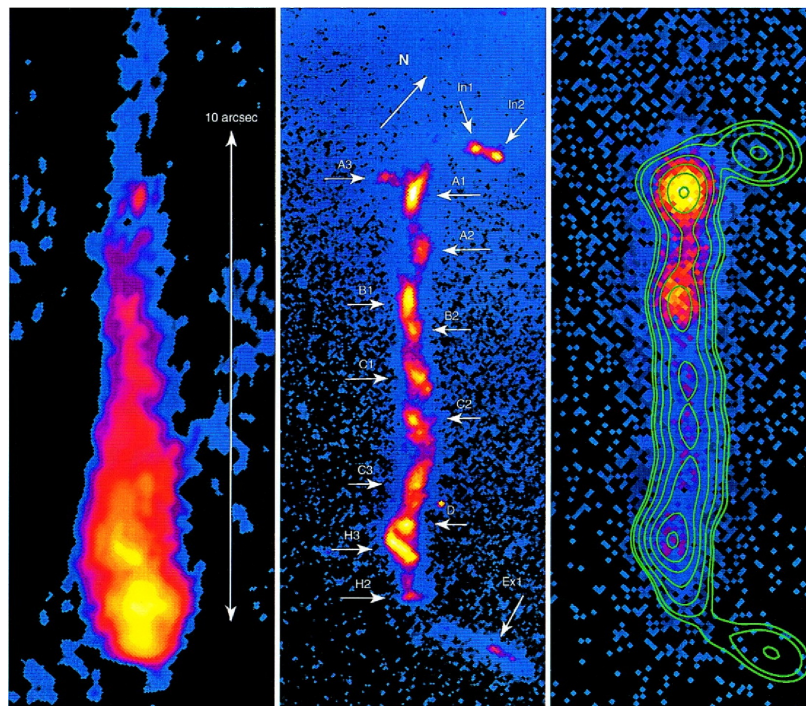


**Figure 1.11:** The knots of 3C 273 jet. left: radio image by MERLIN, middle: optical image by HST and right: X-ray image by *Chandra* with optical contour overlaid (Marshall et al., 2001)

The X-ray and high energy emissions from the knots are often interpreted as an extension of synchrotron emission described above or by the inverse Compton scattering of soft target photon fields by the relativistic particles (See Chapter 2 for detailed explanations). The target photon field for the inverse Compton scattering can be synchrotron photons present in the jet or photon fields outside

the jet. Synchrotron emission from a second electron population is also suggested as a radiation mechanism for the high energy emissions in knots.

## 1.4.2 The Jet Pool

The large-scale jets of AGN appear in wide varieties of shapes and sizes, some straight and some bent. These jets look different in various wavebands, as shown in Fig. 1.12. For instance, the jet of M 87 extends 1.5 kiloparsecs away from the galactic core, whereas the large-scale jet of 3C 273 is approximately 61 kiloparsecs long. The X-ray jet of Pictor A extends up to 100 kpc distance from the core.

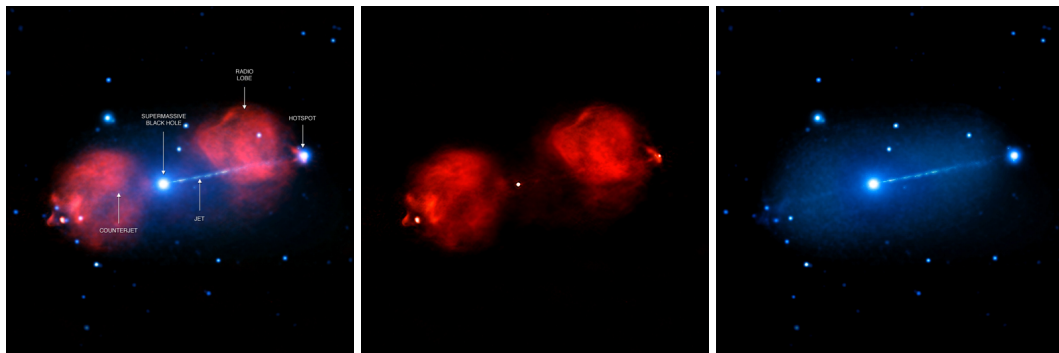


**Figure 1.12:** Pictor A observations at different wavebands. Left: The composite image in radio (red) and X-ray (blue) light. Middle: The radio image. The X-ray image (right) shows continuous X-ray emission over a distance of 570,000 light years. Credit: X-ray: CXC, Radio: ATNF

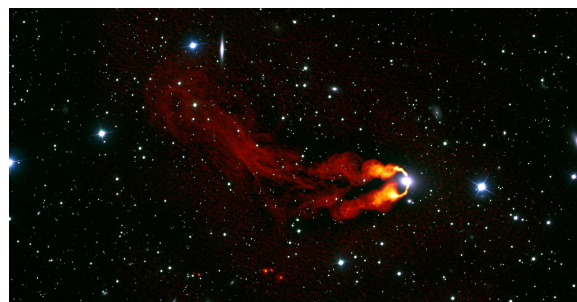


**Figure 1.13:** Radio image of the bent jet of NGC 1265. Image credit: NRAO.

Even though radio galaxies are majorly classified as FRI, FR II and FR 0, a minority of them are found with other unique morphological features. They include Ring-shape, X-shape, W-shape, S-shape or Z-shape, Double Double, Tri-axial, and other Hybrid morphologies (Proctor, 2011). The difference in morphology of radio galaxies can be a result of variations in the host galaxy conditions or the surrounding environment (Miraghaei & Best, 2017). One of the interpretations for the 'U-shaped' jet of NGC 1265 (Fig. 1.14) is the ram pressure exerted by the external gas (O'Dea & Owen, 1986). The origin of 'X-shaped' radio galaxies (XRGs) are attributed to the existence of dual active nuclei at their centre. According to Yang et al. (2022), XRGs that feature two pairs of



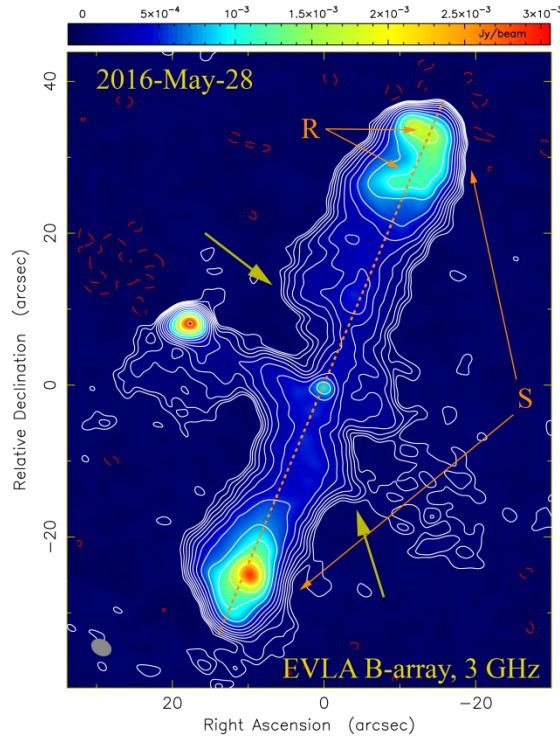


**Figure 1.14:** VLA image of XRG J0725+5835 (Yang et al., 2022)

unaligned radio lobes are due to the jet re-orientation happening due to the presence of a companion galaxy. Recently, deep/machine learning has been employed in radio astronomy for morphological classification (Ndung'u et al., 2023). These techniques can help to uncover the hidden features of a large number of data.

## 1.5 Thesis Outline

This thesis presents the recent findings related to the high energy emission from the large-scale jet of active galactic nuclei and the origin of two population electron hypotheses. The detection of hard X-ray emission from the kilo-parsec scale jet of active galactic nuclei cannot be interpreted as the synchrotron emission mechanism from the electron distribution responsible for the radio/optical emission. The X-ray emission when interpreted as an IC/CMB process, the Compton spectral component will peak at GeV energy. The non-detection of significant gamma-ray flux from these large-scale jets by *Fermi* disfavoured this model, particularly at low redshifts. Alternately, synchrotron emission from a different electron population is suggested. However, the X-ray emissions from the jet of AGN at high redshift are usually interpreted as IC/CMB, due to the increase in CMB photon density. On the other hand, recent *Fermi*  $\gamma$ -ray flux upper limit estimates on jet emission from the high redshift sources question the validity of the IC/CMB model. In such scenarios, the synchrotron emissions from two spatially separated electron populations are capable of explaining this multi-spectral component emission from the AGN knots. In this work, we study the origin of such two-population electron distributions in the large-scale jet of AGN.

The thesis comprises 7 chapters. The following is a brief description of each chapter:

- **Chapter 1** briefly introduces the fundamental concepts related to active galaxies (AGN) and their jets that extend from sub-parsec to kpc/Mpc scales.
- **Chapter 2** presents a brief description of the non-thermal electron distribution, namely, power law and broken power law. The various non-thermal emission mechanisms used to interpret the multi-wavelength emission observed in the AGN jet are also discussed in this chapter. This chapter also briefly describes the equipartition magnetic field and the attenuation of VHE photons by the EBL which has been used in our work.
- In **Chapter 3**, a detailed literature review on the recent advancements related to the high energy emission from large-scale jets of AGN is presented. An in-depth study on the hard X-ray emission from large scale jet, the failure of IC/CMB model to interpret high energy emission: implications of *Fermi*/LAT observations, radio-X-ray positional offsets in knots, X-ray variability of jet emission, and polarization are presented in this chapter. Moreover, recent studies on the MHD simulations and VHE emission associated with large-scale jets of AGN are also discussed.
- Various observational features in the X-ray and gamma-ray energies presented in the previous chapter suggest synchrotron emission from a second electron distribution as the possible origin of high energy emission in large-scale AGN jets. In **Chapter 4** we examine the possible origin of these two populations. We propose a model considering the advection of electrons from the sites of particle acceleration in AGN knots. This advected electron distribution is significantly different from the accelerated electron distribution and satisfies the requirement of the second electron population. The synchrotron emission from the accelerated and the advected electron distribution can successfully reproduce the observed radio-to-X-ray fluxes of the knots of 3C 273 (Rahman et al., 2022)
- In **Chapter 5** we discuss the X-ray emission from the large-scale jet at high redshifts. IC/CMB model was accepted for these sources due to the increase in CMB energy density with redshift. However, recently estimated gamma-ray flux upper limits of two high redshift sources ( $z > 3.5$ ), namely J1510+5702 and J1421-0643, do not comply with the IC/CMB predictions. We apply the electron acceleration and advection model to these sources to explain their MSC jet emissions (Rahman et al., 2024a).
- In **Chapter 6** we study the IC/CMB model for the high energy emission from large-scale jets to predict the VHE gamma-ray emission from them. We found candidate sources whose IC/CMB spectrum falls within the detection threshold of the Cherenkov Telescope Array Observatory (CTAO) (Rahman et al., 2023).
- In **Chapter 7** we summarise the results of this thesis and present the recommendations for future research.



# Chapter 2

## Particle Distribution and Emission Mechanism in AGN Jets

---

*"Light brings us the news of the Universe. Coming to us from the sun and the stars it tells us of their existence, their positions, their movements, their constitutions and many other matters of interest. Coming to us from objects that surround us more nearly it enables us to see our way about the world: we enjoy the forms and colours that it reveals to us, we use it in the exchange of information and thought. ....These greatly differing phenomena are all manifestations of one principle, the magnificent inclusiveness of which has grown clearer continuously as we have studied the nature of light. ....Even the atoms themselves seem to fall, in certain aspects, within the same great category. Light, therefore, using the full meaning of the word, transmits energy which is the mainstay of life, and gives to living beings the power of observation: and it is akin to the matter of which all things animate and inanimate are made. The universe is its sphere of action. We do it no more than justice when we speak of the Universe of Light."*

**- William Henry Bragg**

*The Universe of Light* (Bragg & Bragg, 1962)

### 2.1 Introduction

This chapter discusses the terminologies related to particle distribution and various emission mechanisms relevant to our work. The Fermi acceleration processes in AGN jets result in the formation of a non-thermal electron distribution which is often interpreted as a power-law particle distribution (Kardashev, 1962). Under synchrotron losses, the high-energy particles cool faster and the distribution takes the form of a broken power-law. Section 2.2 briefly describes the mathematical formulation associated with the production of power-law and broken power-law particle distribution. The power-law spectra observed over a broadband energy range in AGN jets suggest the non-thermal nature of radiation. The Multi-Spectral Component (MSC) emission from large-scale jets of AGN is generally understood to be via synchrotron and inverse Compton origin. The hard X-ray emission observed in some of the jets is interpreted using IC/CMB mechanisms. In Section 2.3, the approximate emissivity equations governing the synchrotron, synchrotron self Compton (SSC) and IC/CMB emissions due to a non-thermal electron distribution are explained. Section 2.5 briefly discusses the equipartition magnetic field used to constrain the source parameters in our work. Lastly, the

gamma-ray flux attenuation due to EBL absorption is discussed. Throughout this thesis, the VHE gamma-ray spectra have been corrected for the EBL absorption.

## 2.2 Particle Distribution in AGN jets

The Spectral Energy Distribution (SED) of AGN extends from radio to VHE gamma-ray. This demands the presence of highly energetic particles in the jet medium. The promising mechanism by which particles are accelerated to these energies is the ‘‘Fermi mechanism’’ suggested by Enrico Fermi (Fermi, 1949). As the universe is electrically neutral, no charged particle can be accelerated by electrostatic forces. However, astronomical objects have magnetic fields and can create magnetic inhomogeneities in space. These magnetic irregularities are associated with moving clouds in the interstellar medium. The magnetic inhomogeneities (magnetic mirrors) scatter the charged particles and eventually accelerate them which is generally called Fermi acceleration. When the motion of magnetic mirrors are random, the charged particles gain energy through multiple collisions, which is called stochastic acceleration (second order Fermi acceleration).

The particles in the AGN jet can also be accelerated at the shock front, which is a discontinuity in a medium initiated by the perturbation in a supersonic fluid flow. The particles crossing this shock front from upstream to downstream or vice versa get energised. This process is called shock acceleration (first order Fermi acceleration). A plasma flow through a viscous medium can result in a velocity shear. Particles are accelerated when scattered between different velocity layers by magnetic irregularities (Berezhko, 1981). Such acceleration is called shear acceleration. A detailed discussion of all the acceleration processes mentioned above is presented in Rieger et al. (2007) and Sunder Sahayanathan (2011).

### 2.2.1 Power-law Particle Distribution

The observed power-law spectra of an AGN extending from radio to VHE gamma-ray suggest that the emission is non-thermal and the underlying particle distribution is power-law. The energy of a relativistic particle is given by,  $E = \gamma mc^2$ , where  $\gamma$  is the Lorentz factor associated with it. The rate of acceleration of the particle can be parametrised as,

$$\frac{d\gamma}{dt} \propto \frac{\gamma}{t_a} \quad (2.2.1)$$

where  $t_a$  is the acceleration time scale. Solving the above equation we get,

$$\gamma(t) = \gamma_0 \exp(t/t_a) \quad (2.2.2)$$

This indicates that the energy of the particles grows exponentially with time. Now, let us consider a region of interest where the particles are being accelerated (Figure 2.1). Considering a mono-energetic injection of particles (at energy  $\gamma_0$ ) into the region, the accelerator accelerates them at the

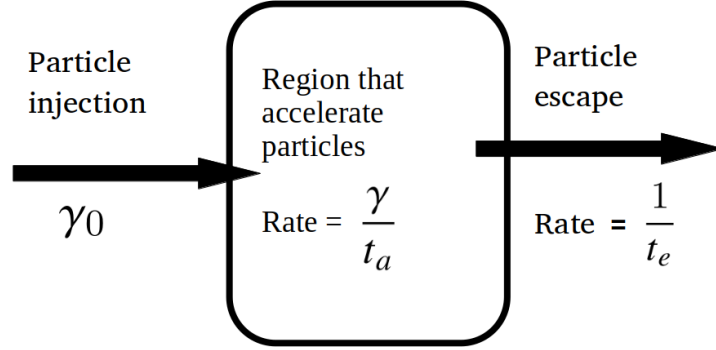


**Figure 2.1:** The schematic diagram representing the formation of particle distribution in AGN jet.

rate of  $\frac{\gamma}{t_a}$  (constant acceleration time scale  $t_a$ ). There is a finite probability for the particles to escape from the region with characteristic escape time  $t_e$ . The kinetic equation governing the evolution of the particle distribution is given by (Ginzburg & Syrovatskii, 1964),

$$\frac{\partial N(\gamma, t)}{\partial t} + \frac{\partial}{\partial \gamma} [P(\gamma) N(\gamma, t)] = Q - \frac{N(\gamma, t)}{t_e} \quad (2.2.3)$$

where  $P(\gamma)$  is the rate of change of energy and  $Q \equiv Q_0 \delta(\gamma - \gamma_0)$  is the injection spectrum. Under steady state and considering only energy gain i.e.,  $P(\gamma) = \frac{\gamma}{t_a}$  equation 2.2.3 becomes

$$\frac{d}{d\gamma} \left[ \frac{\gamma}{t_a} n(\gamma) \right] = Q_0 \delta(\gamma - \gamma_0) - \frac{n(\gamma)}{t_e} \quad (2.2.4)$$

For  $\gamma > \gamma_0$ , above equation becomes

$$\frac{d}{d\gamma} [\gamma n(\gamma)] = -\frac{t_a}{t_e} n(\gamma) \quad (2.2.5)$$

Solving equation 2.2.5, we get

$$n(\gamma) = K \gamma^{-p} \quad (2.2.6)$$

where  $K$  is the normalisation constant and  $p = (1 + \frac{t_a}{t_e})$ .

## 2.2.2 Particle distribution under synchrotron losses

The relativistic particles interact with the astrophysical magnetic fields and lose their energy via synchrotron emission. For a particle of Lorentz factor  $\gamma$ , the pitch angle averaged synchrotron

energy loss rate in a magnetic field  $B$  is given by (Rybicki & Lightman, 1986)

$$\begin{aligned} P(\gamma) &= \frac{4}{3} \sigma_T c \beta^2 \gamma^2 U_B \\ &= \eta \gamma^2 \end{aligned} \quad (2.2.7)$$

where,  $\sigma_T = \frac{8\pi r_0^2}{3}$  and  $U_B = \frac{B^2}{8\pi}$  are the Thomson cross section and magnetic energy density respectively. The equation governing the particle distribution can now be expressed as

$$\frac{d}{d\gamma} \left[ \left( \frac{\gamma}{t_a} - \eta \gamma^2 \right) n(\gamma) \right] = -\frac{n(\gamma)}{t_e} \quad (2.2.8)$$

The particles can be accelerated to maximum energy  $\gamma_{\max}$  when  $\left( \frac{\gamma_{\max}}{t_a} - \eta \gamma_{\max}^2 \right) = 0$ . Hence,

$$\gamma_{\max} = \frac{1}{\eta t_a} \quad (2.2.9)$$

For particles with energy  $\gamma < \gamma_{\max}$ , acceleration dominates whereas for particles with  $\gamma > \gamma_{\max}$ , the loss term dominates and particles do not get accelerated further. Hence the solution will be

$$n(\gamma) \approx K \gamma^{-p} \Theta(\gamma_{\max} - \gamma) \quad (2.2.10)$$

where  $\Theta$  is the Heaviside function.

When the accelerated particles encounter only the synchrotron loss rate, then the equation takes the form

$$\frac{d}{d\gamma} [-\eta \gamma^2 n(\gamma, t)] = K \gamma^{-p} \Theta(\gamma_{\max} - \gamma) \quad (2.2.11)$$

Solving the above equation, we get

$$n(\gamma) = K' \gamma^{-(p+1)} \quad (2.2.12)$$

Hence, the synchrotron cooling steepens the particle spectrum by index 1.

The characteristic synchrotron cooling time scale can be obtained from equation 2.2.7 as

$$t_{\text{cool}}(\gamma) = \frac{1}{\eta \gamma} \quad (2.2.13)$$

If there is a finite probability for the particle to escape from the region and expressing this time scale as  $t_b$ , we get the energy of the particle  $\gamma_b$  for which  $t_b = t_{\text{cool}}(\gamma)$ . For the case of  $\gamma_b < \gamma_{\max}$ , it results in the formation of a broken power-law particle distribution with the indices  $p$  and  $p+1$ . The particles with energy  $\gamma < \gamma_b$  will escape the system before being cooled and hence will preserve the index  $p$ . On the other hand, particles with energy  $\gamma > \gamma_b$  will cool before escaping the system and hence maintain the index  $p+1$ . Hence, the broken power-law particle distribution can be expressed

as

$$n(\gamma) \sim \begin{cases} \gamma^{-p} & \gamma_0 < \gamma < \gamma_b \\ \gamma^{-(p+1)} & \gamma_b < \gamma < \gamma_{\max} \end{cases} \quad (2.2.14)$$

## 2.3 Non-thermal Radiative Mechanisms

Broadband emissions from active galactic nuclei (AGN) consist of both thermal and non-thermal radiation. However, non-thermal emissions are more prominent in blazars, particularly in large-scale AGN jets. Jets radiate via synchrotron, synchrotron self-Compton (SSC), and other external Compton emission mechanisms. In the following section, these topics are briefly discussed. For a detailed derivation and explanation, please refer to Blumenthal & Gould (1970); Rybicki & Lightman (1986).

### 2.3.1 Synchrotron emission

Charged particles emit radiation when a magnetic field accelerates them. When the particle moves at a non-relativistic velocity, the radiation emitted is simple and is called cyclotron radiation. This radiation is emitted at a single frequency equal to the frequency of the particle's gyration in the magnetic field. However, when the particle's velocity approaches relativistic scales, the frequency spectrum becomes broad and extends beyond the gyration frequency. This type of radiation is known as synchrotron radiation. The synchrotron radiative power emitted by an electron of energy  $\gamma$  with velocity  $\beta (= v/c)$  moving at an angle  $\alpha$  (pitch angle) with respect to uniform magnetic field  $B$  is given by

$$P(\gamma) = \frac{2}{3} r^2 c \gamma^2 \beta^2 B^2 \sin^2 \alpha \quad (2.3.1)$$

where  $r = \frac{e^2}{m_e c^2}$  is the classical electron radius. Equation 2.3.1 can be averaged over all  $\alpha$  to calculate the synchrotron power for relativistic isotropic electron distribution given by,

$$P(\gamma) = \frac{4}{3} \sigma_T c \gamma^2 \beta^2 U_B \quad (2.3.2)$$

where  $U_B = B^2/8\pi$  is the energy density of magnetic field and  $\sigma_T$  is the Thomson cross-section. The synchrotron spectrum emitted by an electron of energy  $\gamma m_e c^2$  with pitch angle  $\alpha$  is given by (Blumenthal & Gould, 1970);

$$P_{syn}(\gamma, \nu) = \frac{\sqrt{3} e^3 B \sin \alpha}{m_e c^2} F\left(\frac{\nu}{\nu_c}\right) \quad (2.3.3)$$

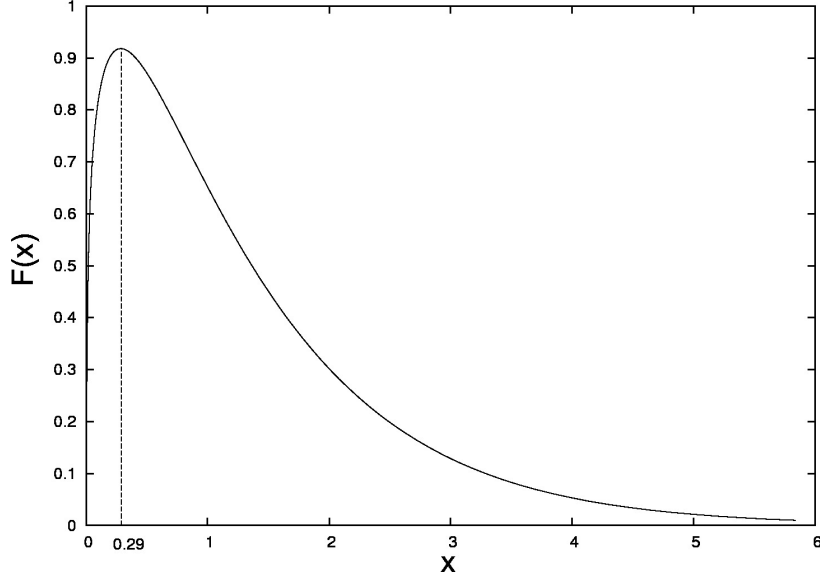


**Figure 2.2:** Synchrotron power function.

Here,  $F$  is the synchrotron power function defined as

$$F(x) = x \int_x^{\infty} K_{5/3}(\xi) d\xi \quad (2.3.4)$$

and  $K_{5/3}$  is the modified Bessel function of order  $5/3$ ,  $\nu$  is the frequency of the emitted photon and  $\nu_c$  is the critical frequency of radiation given by,

$$\nu_c = \frac{3 e B \gamma^2}{4\pi m_e c} \sin \alpha \quad (2.3.5)$$

The spectral shape is determined by  $F(x)$  with its peak at  $x \approx 0.29$  (Figure 2.2). The single particle emission spectrum can be expressed using equation 2.3.2 as,

$$P_{syn}(\gamma, \nu) = \frac{4}{3} \beta^2 \gamma^2 c \sigma_T U_B \phi_\nu(\gamma) \quad (2.3.6)$$

where  $\phi$  is a function of  $\gamma$  and  $\nu$  satisfying the condition,

$$\int_0^{\infty} \phi_\nu(\gamma) d\nu = 1 \quad (2.3.7)$$

The function  $\phi$  can be approximated to a Dirac delta function (to the orders of unity), considering the shape of the spectrum (Figure 2.2)

$$\phi_\nu(\gamma) \rightarrow \delta(\nu - \gamma^2 \nu_L) \quad (2.3.8)$$

where  $\nu_L = eB/2\pi m_e c$  is the Larmor frequency.

For an isotropic power-law electron distribution of the form,

$$N(\gamma) = k \gamma^{-p} \quad \gamma_{min} < \gamma < \gamma_{max} \quad (2.3.9)$$

the radiation energy emitted per second per frequency for  $\gamma_{max} \gg \gamma_{min}$  can be expressed as (Blumenthal & Gould, 1970)

$$\frac{dE}{d\nu dt} \approx \frac{4\pi k e^3 B^{(p+1)/2}}{m_e c^2} \left( \frac{3e}{4\pi m_e c} \right)^{(p-1)/2} a(p) \nu^{-(p-1)/2} \quad (2.3.10)$$

where the function  $a(p)$  depends on the particle's spectral index. Accordingly, the synchrotron spectrum is a power-law with index  $(p - 1)/2$ .

A synchrotron emission is accompanied by an absorption process called synchrotron self-absorption (SSA). In this process, a charged particle in a magnetic field absorbs a photon and gets energized. Moreover, this can induce the charged particle to emit in a frequency and direction of the photon itself known as stimulated emission or negative absorption. The synchrotron self-absorption coefficient is given by Ghisellini & Svensson (1990) as:

$$\kappa_\nu = -\frac{1}{8\pi m_e \nu^2} \int \frac{N(\gamma)}{\gamma (\gamma^2 - 1)^{1/2}} \frac{d}{d\gamma} [\gamma(\gamma^2 - 1)^{1/2} P_{syn}(\gamma, \nu)] \quad (2.3.11)$$

The specific intensity ( $I_\nu$ ) of synchrotron radiation for a source with uniform properties and zero background illumination is computed using the radiative transfer equation as (Shu, 1991)

$$I_\nu = S_\nu(1 - e^{-\tau_\nu}) \quad (2.3.12)$$

$S_\nu (= j_\nu/\kappa_\nu)$  is the synchrotron source function and  $\tau_\nu$  is the optical depth defined over a distance  $s$  as

$$\tau_\nu = \int_s \kappa_\nu ds' \quad (2.3.13)$$

The synchrotron emissivity ( $j_\nu$ ) for an isotropic emission is given by

$$J_\nu = \frac{1}{4\pi} \int_{\gamma_{min}}^{\gamma_{max}} P_{syn}(\gamma, \nu) N(\gamma) d\gamma \quad (2.3.14)$$

The synchrotron self absorption coefficient associated with a power-law distribution of particle (equation 2.3.9), is given by (Shu, 1991)

$$\kappa_\nu \propto B^{\frac{p+2}{2}} \nu^{-\frac{(p+4)}{2}} \quad (2.3.15)$$

It is possible that a source may behave optically thick ( $\tau_\nu > 1$ ) at low frequencies and optically thin ( $\tau_\nu < 1$ ) at high frequencies. From equations 2.3.6, 2.3.14 and 2.3.15 we find that the source

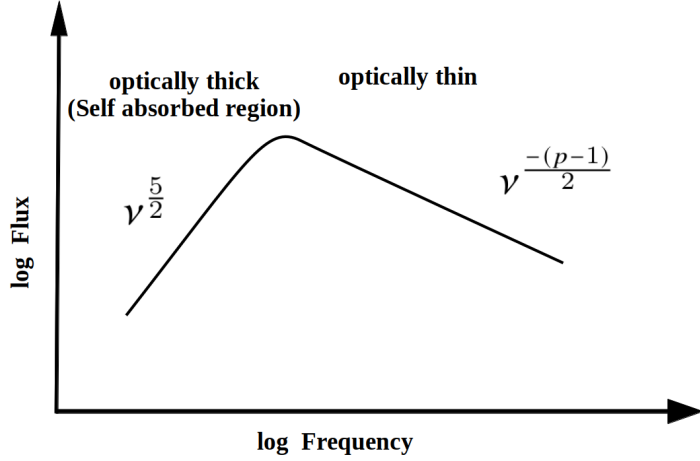


**Figure 2.3:** Synchrotron spectrum from a power-law distribution of electron

function  $S_\nu$  for the optically thick region will be a power-law of the form

$$S_\nu \propto \nu^{\frac{5}{2}} \quad (2.3.16)$$

The synchrotron spectrum follows a broken power-law, shifting from  $\nu^{\frac{5}{2}}$  at lower frequencies to  $\nu^{-\frac{(p-1)}{2}}$  at high frequencies. The frequency at which index variation occurs is known as synchrotron self-absorption frequency. For AGN jet emission, this frequency is observed to be within a few gigahertz range.

### 2.3.2 Inverse-Compton Radiation

Compton scattering is the mechanism by which high-energy (or hard) photons scatter low-energy electrons. Conversely, low-energy (or soft) photons are scattered off by high-energy (relativistic) electrons; this effect is known as inverse Compton scattering (Figure 2.4). Depending on the energy of the incident photon ( $\epsilon$ ) in comparison to the electron rest mass energy ( $m_e c^2$ ), the scattering cross section can be either Thomson or Klein-Nishina.

- **Thomson cross section** ( $\gamma\epsilon \ll m_e c^2$ ): When the energy of an incident photon is much smaller than the rest mass energy of an electron (in the electron's rest frame), the recoil of the electron can be ignored. In this case, the energy of the photon remains unchanged in the electron's reference frame. The associated differential Thomson cross section for this scenario is given by:

$$\frac{d\sigma_T}{d\Omega} = \frac{1}{2} r_e^2 (1 + \cos^2 \theta) \quad (2.3.17)$$

Here  $r_e$  and  $\theta$  are the classical electron radius and angle between the incident and the scattered photon directions, respectively. The scattered photon energy ( $\epsilon_s$ ) can be shown as (Blumenthal



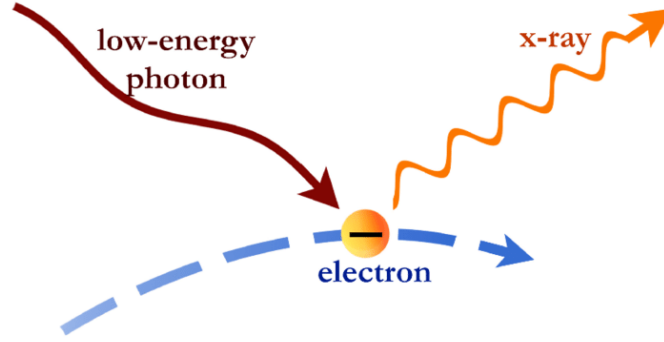


**Figure 2.4:** Inverse Compton scattering: collision of an energetic electron with a photon can increase the energy of the photon.

& Gould, 1970)

$$\epsilon_s \approx \gamma^2 \epsilon \quad (2.3.18)$$

Compared to the electron energy, this gain is minimal and hence a small fraction of energy is lost by the electron in each scattering.

- **Klein-Nishina cross section** ( $\gamma\epsilon \gtrsim m_e c^2$ ): When the energy of an incident photon is comparable with the rest mass energy of an electron (as observed in the electron's rest frame), the recoil of the electron becomes significant. In such scenarios, the scattering cross section includes quantum effects and is described by the Klein-Nishina differential cross section given as:

$$\frac{d\sigma_{KN}}{d\Omega} = \frac{r_e^2}{2} \frac{\epsilon_s^2}{\epsilon^2} \left( \frac{\epsilon}{\epsilon_s} + \frac{\epsilon_s}{\epsilon} - \sin^2 \theta \right) \quad (2.3.19)$$

where  $\epsilon$  and  $\epsilon_s$  are the energies of the incident and the scattered photon, respectively. The scattered photon energy, in this case, is

$$\epsilon_s \approx \gamma m_e c^2 \quad (2.3.20)$$

Therefore, in the Klein-Nishina regime, the entire energy of the electron is lost to the photon in a single scattering.

The power lost by an electron (or the radiative power emitted) due to inverse Compton scattering of an isotropic soft photon distribution is (Rybicki & Lightman, 1986)

$$P_{IC} = \frac{4}{3} \beta^2 \gamma^2 c \sigma_T U_{ph} \quad (2.3.21)$$

Here,  $U_{ph}$  is the soft target photon energy density and assumes scattering occurs in Thomson regime. Comparison of the above power (2.3.21) with the one emitted in synchrotron emission (2.3.2), we get

$$\frac{P_{syn}}{P_{IC}} = \frac{U_B}{U_{ph}} \quad (2.3.22)$$

In the Klein-Nishina regime, the power lost by an electron can be computed using

$$P_{IC,KN} = \int \int (\epsilon_s - \epsilon) \frac{dN}{dt d\epsilon_s} d\epsilon_s \quad (2.3.23)$$

where  $\frac{dN}{dt d\epsilon_s}$  is the emission rate of the scattered photon per frequency as given in Blumenthal & Gould (1970).

The soft target photons responsible for the inverse Compton process can be either internal or external to the jet (Boettcher et al., 1997). On the basis of this, the process is classified as follows:

### Synchrotron Self Compton (SSC)

In this process, the electron population, which is responsible for the synchrotron emission in the jet, scatter off the synchrotron photons (already in the jet) to higher energies (Ginzburg & Syrovatskii, 1965; Tavecchio et al., 1998). This has been discussed in detail in Ginzburg & Syrovatskii (1965); Tavecchio et al. (1998).

Using the Klein-Nishina formula, one can get the single particle Compton emissivity resulting from the scattering of the isotropic synchrotron photons as (Blumenthal & Gould, 1970; Jones, 1968)

$$P_{SSC}(\gamma, \nu_s) = \frac{3\pi\sigma_T\nu_s}{\gamma^2} \int_{x_1}^{x_2} \frac{I_{syn}(\nu_i)}{\nu_i^2} f(\nu_i, \nu_s, \gamma) d\nu_i \quad \text{erg/s/Hz} \quad (2.3.24)$$

where,  $I_{syn}$ ,  $\nu_i$ ,  $\nu_s$ ,  $x_1$  and  $x_2$  are the synchrotron specific intensity, incident photon frequency, scattered photon frequency, lower and higher limits on incident photon frequency respectively. The SSC emissivity due to a given electron distribution  $N(\gamma)$  will be

$$J_{SSC}(\nu) = \frac{1}{4\pi} \int_{\gamma_{min}}^{\gamma_{max}} P_{SSC}(\gamma, \nu) N(\gamma) d\gamma \quad \text{erg/cm}^3/\text{s/Hz/Sr} \quad (2.3.25)$$

Similar to the synchrotron scenario, an approximate analytical solution for SSC emissivity in the Thomson domain can be derived by considering the single particle emissivity as (Sahayanathan & Godambe, 2012)

$$P_{SSC}(\gamma, \nu) = \frac{4}{3}\beta^2\gamma^2 c\sigma_T \int_{\nu_{syn}^{min}}^{\nu_{syn}^{max}} U(\xi) d\xi \Psi_\nu(\xi, \gamma) \quad (2.3.26)$$

where,

$$U_{\text{ph}} = \int_{\nu_{\text{syn}}^{\text{min}}}^{\nu_{\text{syn}}^{\text{max}}} U(\xi) d\xi \quad \text{erg/cm}^3 \quad (2.3.27)$$

is the synchrotron photon energy density and the function  $\Psi_\nu(\xi, \gamma)$  meets the condition

$$\int_0^\infty \Psi_\nu(\xi, \gamma) d\nu = 1 \quad (2.3.28)$$

In the Thomson regime, the scattered photon frequency is approximately  $\gamma^2\xi$ . Hence, we can express  $\Psi_\nu(\xi, \gamma)$  as

$$\Psi_\nu(\xi, \gamma) \rightarrow \delta(\nu - \gamma^2\xi) \quad (2.3.29)$$

The approximate SSC emissivity considering equation (2.3.25) will then be,

$$J_{\text{SSC}}(\nu) \approx \frac{1}{3\pi} c \sigma_T \int_{\gamma_{\text{min}}}^{\gamma_{\text{max}}} U\left(\frac{\nu}{\gamma^2}\right) N(\gamma) d\gamma$$

### External Compton (EC)

In this mechanism, the photons that are produced outside the emission region (or outside the jet) are scattered off to high energies by the inverse Compton process. This photon field includes thermal photons from the accretion disk, cosmic microwave background radiation, broad emission line photons and/or the IR photons from the dusty torus (Dermer & Schlickeiser, 1993; Sikora et al., 1994; Tavecchio et al., 2000).

A general case can be considered assuming an isotropic soft photon target distribution being scattered off to high energies by a distribution of relativistic electrons. However, in the context of the AGN jet, these considerations are inappropriate as the plasma sees an anisotropic target photon distribution when the emission region moves down the jet at relativistic speed as an effect of Doppler boosting. For example, let us consider the spherical emission region, moving down the jet with bulk Lorentz factor,  $\Gamma$  and making an angle  $\theta_o$  with the line of sight of the observer. For simplicity, let us consider a monochromatic and isotropic target photon distribution in the central source frame ( $u_{iso}$ ). The energy density of this target photon distribution in the emission region frame will be

$$u_{er} = \Gamma^2 u_{iso} \quad (2.3.30)$$

In the emission region frame, the target photon energy will peak at  $\epsilon_{er} \approx \Gamma\epsilon^*$ , where  $\epsilon^*$  is the energy of the external photon field. The inverse Compton emissivity associated with a power-law distribution of particles (2.2.6) at photon energy  $\epsilon$  emitted in a direction  $\omega$  is given by,

$$J_{\text{EC}}(\epsilon, \omega) \approx \frac{c\sigma_T u_{\text{iso}} K}{8\pi\epsilon^*} [\Gamma(1 + \mu)]^{1+\alpha} \left(\frac{\epsilon}{\epsilon^*}\right)^{-\alpha} \quad (2.3.31)$$

where  $\mu = \cos\theta$ , with  $\theta$  being the angle between jet and emitted photon;  $\alpha = (p - 1)/2$ . As the scattering here is under the Thomson regime; the above equation is valid for photon energies in the limits given by,

$$\gamma_{\text{min}}^2 \leq \frac{\epsilon}{\Gamma\epsilon^*(1 + \mu)} \leq \gamma_{\text{max}}^2 \quad (2.3.32)$$

Here,  $\Gamma(1 + \mu)$  can be represented in terms of Doppler factor  $\delta$ , the velocity of the emission region along jet ( $v$ ) and  $\theta_0$  as

$$\Gamma(1 + \mu) = \delta \frac{(1 + \cos\theta_0)}{1 + v/c} \quad (2.3.33)$$

### IC/CMB Mechanism

In this mechanism, the inverse Compton scattering of photons of the cosmic microwave background (CMB) with the particle distribution results in radiation. The IC/CMB spectral component can be estimated by considering CMB distribution as a monochromatic photon field and a delta-function approximation for single particle emissivity (Dermer & Menon, 2009; Sahayanathan et al., 2018).

$$J_{\text{IC/CMB}}(\nu) \approx \frac{c\sigma_T U_{\text{CMB}}}{8\pi\nu_*} \sqrt{\frac{\Gamma\nu(1 + \mu)}{\nu_{\text{CMB}}}} N \left[ \sqrt{\frac{\nu}{\Gamma\nu_{\text{CMB}}(1 + \mu)}} \right] \quad (2.3.34)$$

Here,  $\nu_{\text{CMB}}$  and  $U_{\text{CMB}}$  are the frequency and energy density of the CMB photon field,  $\Gamma$  is the bulk Lorentz factor of the jet, and  $\mu$  is the cosine of the jet viewing angle measured in the proper frame of the AGN. The relativistic boosting increases the energy density of the CMB in the jet frame, given by

$$U_{\text{CMB}} = 4 \times 10^{13} (1 + z)^4 \Gamma^2 \quad \text{erg/cm}^3 \quad (2.3.35)$$

where  $z$  is the redshift of the source.

## 2.4 Relativistic Beaming & Jet Assymetry

In the case of AGNs, the apparent luminosity of the source is modified due to relativistic effects and is often referred to as relativistic beaming/ Doppler beaming/ Doppler boosting. The physical effects like light aberration and the Doppler effect can cause the beaming in relativistically moving objects (Ghisellini, 2000). When light aberration results in the concentration of radiation along the object's direction of motion, the Doppler effect alters the radiation energy by red/blue shift. The time interval

of radiation measured by an observer on earth ( $\Delta t_{obs}$ ) is different from the actual time interval in the emitting frame ( $\Delta t_{em}$ ) due to photon arrival time effects. They are related by,

$$\Delta t_{obs} = \Gamma(1 - \beta \cos \theta) \Delta t_{em} = \frac{\Delta t_{em}}{\delta_D} \quad (2.4.1)$$

where  $\Gamma \left( = \frac{1}{\sqrt{1-\beta^2}} \right)$ ,  $\theta$  and  $\delta_D$  are the Lorentz factor, viewing angle and the Doppler factor respectively. When the jet of an AGN is directed towards the observer, the radiation that is observed is shifted to higher energies, which is represented by the equation,  $\nu_{obs} = \delta_D \nu_{em}$ . Moreover, as a result of this phenomenon, the luminosity of the observed emission ( $L_{obs}$ ) is observed to be higher than the actual emitted radiation ( $L_{em}$ ), given by:

$$L_{obs} = \delta_D^\alpha L_{em} \quad (2.4.2)$$

The parameter  $\alpha$  is a jet characteristic with a value greater than 1. The effect of beaming is noticeable in the images of the AGN jet (Fig. 2.5). The jet that is pointing towards the observer appears bright in contrast to the one pointing away, which is often fainter or not visible at all (for instance, the jet of M 87). However, both the jets of 3C 31 have similar brightness which indicates that their jets are oriented at right angles to the line of sight of the observer.

The jets of AGN are either observed one-sided or two-sided with asymmetries in shape and length due to the effect of beaming. Assuming the central engine of an AGN produces two jets, the one moving towards the observer will show enhanced brightness. Whereas the counter-jet moving away from the observer will be dimmed or appear invisible. Ghisellini et al. (1993) express the ratio

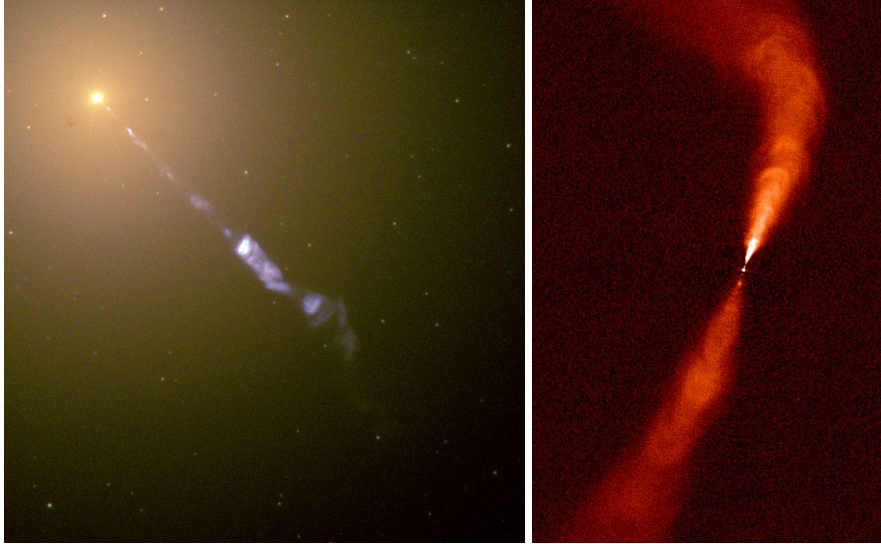


**Figure 2.5:** Left: The single jet of M 87 (Image credits: HST). Right: The two jets of 3C 31 (Image credits: NRAO).

of the flux of the jet ( $F_{jet}$ ) and counter jet ( $F_{c-jet}$ ) as

$$J = \frac{F_{jet}}{F_{c-jet}} = \left( \frac{1 + \beta \cos \theta}{1 - \beta \cos \theta} \right)^p \quad (2.4.3)$$

where  $\beta$  and  $\theta$  are the bulk velocity (in units of  $c$ ) and viewing angle of the jet, respectively. The  $p$ -value can be  $2 + \alpha$  (in case of a continuous jet flow) or  $3 + \alpha$  (for a moving isotropic source), where  $\alpha$  is the power-law spectral index of intrinsic jet flux. This ratio ( $J$ ) can be expressed in terms of  $\beta_a$  as:

$$J = (\beta_a^2 + \delta_D^2)^p \quad (2.4.4)$$

Here,  $\delta_D$  is the Doppler boosting factor as mentioned in equation 2.4.1.

## 2.5 Equipartition Magnetic Field

Consider a source of volume  $V$  with power law particle distribution cooling in a magnetic field  $B$ . Then the total energy ( $U_{tot}$ ) of a source is the sum of energies associated with particles ( $U_p$ ) and magnetic field ( $U_B$ ).

$$U_{tot} = U_p + U_B \quad (2.5.1)$$

The magnetic field ( $B_{min}$ ) corresponds to the minimum value of the total energy of the system is obtained by solving

$$\left( \frac{\partial U_{tot}}{\partial B} \right)_{B=B_{min}} = 0 \quad (2.5.2)$$

The equipartition magnetic field  $B_{eq}$  corresponding to the relation  $U_p = U_B$  when compared with  $B_{min}$  differ only by a factor less than 10%.

The total energy corresponding to  $B_{eq}$  and  $B_{min}$  is given by,

$$U_{tot}(B_{eq}) = 2V \left( \frac{B_{eq}^2}{8\pi} \right) \quad \text{and} \quad (2.5.3)$$

$$U_{tot}(B_{min}) = \frac{7}{3}V \left( \frac{B_{min}^2}{8\pi} \right) \quad (2.5.4)$$

This implies,

$$U_{tot}(B_{eq}) \approx 1.01 U_{tot}(B_{min}) \quad (2.5.5)$$

Therefore, to ensure the minimum energy condition while modelling the source, equipartition value for the magnetic field is used (Burbidge, 1959; Kembhavi & Narlikar, 1999).

## 2.6 EBL and Gamma-ray Attenuation

The diffuse and isotropic radiation field in the ultraviolet to far-infrared wavelengths accumulated during the phase of the star and galaxy formation history of the universe is called the Extragalactic Background Light (EBL). After the CMB radiation, the remnant of blackbody radiation at 2.7 K during the Big Bang, EBL is the second dominant diffused background radiation in the universe. The VHE gamma rays from extragalactic sources like AGN jets, interact with EBL photons, resulting in the creation of electrons and positrons via pair production. The necessary condition for pair production is that the product of the energies of the VHE photon and EBL photon should be greater than  $(m_e c^2)^2$ . This process can be represented as,

$$\gamma_{\text{VHE}} + \gamma_{\text{EBL}} \longrightarrow e^+ + e^- \quad (2.6.1)$$

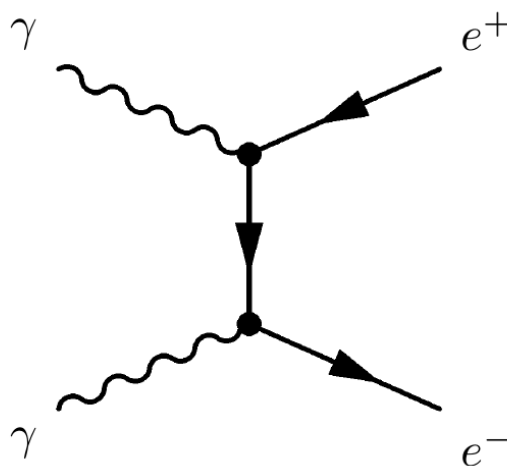


**Figure 2.6:** The schematic diagram representing pair-production

A schematic of this is shown in Figure 2.6. This interaction results in the attenuation of gamma-ray flux and influences the measured spectrum. This attenuation caused by EBL depends on the redshift of the source and energy of radiation. Various methods have been adopted to estimate the EBL density (Stecker & de Jager, 1993; Stanev & Franceschini, 1998; Mazin & Raue, 2007; Razzaque et al., 2009; Yang & Wang, 2010; Ackermann et al., 2012; Franceschini et al., 2019).

# Chapter 3

## High Energy Emissions from Large scale Jets of AGN: Recent Advancements

---

*"Radio astronomy is intimately related to high energy astronomy. Estimates of magnetic fields in the lobes of radio sources led to the recognition that TeV electrons must be present to radiate via the synchrotron mechanism. This motivated early suggestions that direct detection of celestial gamma rays might be feasible. Estimates of the energy contents of these radio lobes were extremely large, posing difficulties for explaining the origin and possible relation to the associated galaxy or quasar. The dilemma was solved by theoretical explanations of how collimated beams of particles and fields, i.e. jets, could carry energy to the lobes, and by direct imaging of these radio jets. The existence of X-ray emission from the nearest, brightest jets in Cen A, 3C273, and M87 resulted from observations by the ROSAT and Einstein X-ray telescopes, each with about 5 arcsec angular resolution. The Chandra X-ray observatory with its 0.5 arcsec resolution telescope gives a 100-fold increase in 2-dimensional imaging capability. This has led to the discovery of X-ray jets in a wide variety of astronomical systems, and in particular, has exploded the study of X-ray emission from extragalactic radio jets."*

*- Daniel A. Schwartz*

*The High-energy emission of jetted AGN (Schwartz, 2020)*

### 3.1 Introduction

Over the last two decades, there have been numerous exciting high energy observations related to the large-scale jet of AGN. The *Chandra* X-ray Telescope has been instrumental in discovering approximately 150 resolved X-ray jets (XJET database: <https://hea-www.harvard.edu/XJET/>). The X-ray luminosity associated with these jets, which span kilo-parsecs/Mega-parsecs, is mostly due to the emission from bright knots and terminal hotspots. In recent times, the Fermi Large Area Telescope (*Fermi*/LAT) observations have been widely used to estimate the flux or flux upper limit in the gamma-rays from the large-scale jet (Georganopoulos et al., 2006; Breiding, 2018). This led to a questioning of the IC/CMB interpretation for the observed phenomena. Rather, this suggests the possibility of a second electron population being responsible for high-energy emission. Another important piece of evidence that adds to the debate over the origin of X-ray emission is the positional offset observed between the location of radio and X-ray features in resolved large-scale jets (Marchenko et al., 2017). Recently, using the Low-count Image Reconstruction Algorithm (LIRA),



it has been found that out of all the knots with detectable offsets, 55% of them show X-rays peaking upstream of the radio (Reddy et al., 2021). This behaviour questions the applicability of one-zone models in the jets. Detecting X-ray variability in the large-scale jet population is another exciting finding (Meyer et al., 2023), favouring the second electron population and synchrotron emission. The acceleration and propagation of jets in active galactic nuclei (AGN) are significantly influenced by the magnetic field. The polarization observations yield important details about their magnetic field (Park & Algaba, 2022). Recent developments in polarimetric techniques can enhance our understanding of the magnetic field structures and underlying particle distribution. In the following section (section 3.2), a detailed discussion of each of these recent developments along with their possibilities and challenges are presented.

Lately, relativistic MHD simulations have been conducted widely to understand the evolution and dynamics of large-scale jets. Section 3.3 briefly describes the recent studies done in this field. Moreover, the recent detection of VHE gamma-ray emission from radio galaxies opens questions on large-scale jets as the possible origin of VHE emission. This has been briefly presented in section 3.4.

## 3.2 The Resolved Jet: Multiwavelength Observations and Theories

### 3.2.1 The Emission Mechanism

The multi-spectral component (MSC) emission from AGN knots is generally modelled using synchrotron and inverse Compton emission mechanisms depending on the hardness of the optical-to-X-ray spectral index ( $\alpha_{ox}$ ) in comparison to the radio-to-optical spectral index ( $\alpha_{ro}$ ) (Jester et al., 2006). The radio-to-optical emission is well established as a synchrotron emission from a relativistic electron distribution, losing its energy in the jet magnetic field. On the other hand, the X-ray emission process is modelled as the high-energy tail of the synchrotron spectrum when  $\alpha_{ox} > \alpha_{ro}$  (Hardcastle et al., 2001; Sambruna et al., 2002; Sahayanathan, 2008). In Fig. 3.1, the multiwavelength emission from the kilo-parsec scale knots of M87 is modelled using synchrotron emission from a broken power-law distribution of relativistic particles.

When the optical-to-X-ray spectral index is less than the radio-to-optical ( $\alpha_{ox} < \alpha_{ro}$ ), the situation demands convex (concave upward) electron distribution and the emission is attributed to inverse Compton processes or emission from a different/second electron population (Tavecchio et al., 2000; Schwartz et al., 2000; Sahayanathan et al., 2003; Atoyan & Dermer, 2004; Harris et al., 2004; Kataoka & Stawarz, 2005; Uchiyama et al., 2006; Perlman et al., 2011). The high energy emission from knots, when interpreted as the inverse Compton mechanism, the target photon field at these length scales can be either synchrotron photons (Schwartz et al., 2000); usually called as synchrotron self Compton(SSC) or the ambient cosmic microwave background radiation (Tavecchio et al., 2000; Sambruna et al., 2001); termed IC/CMB mechanism. The SSC interpretation is disfavored as it

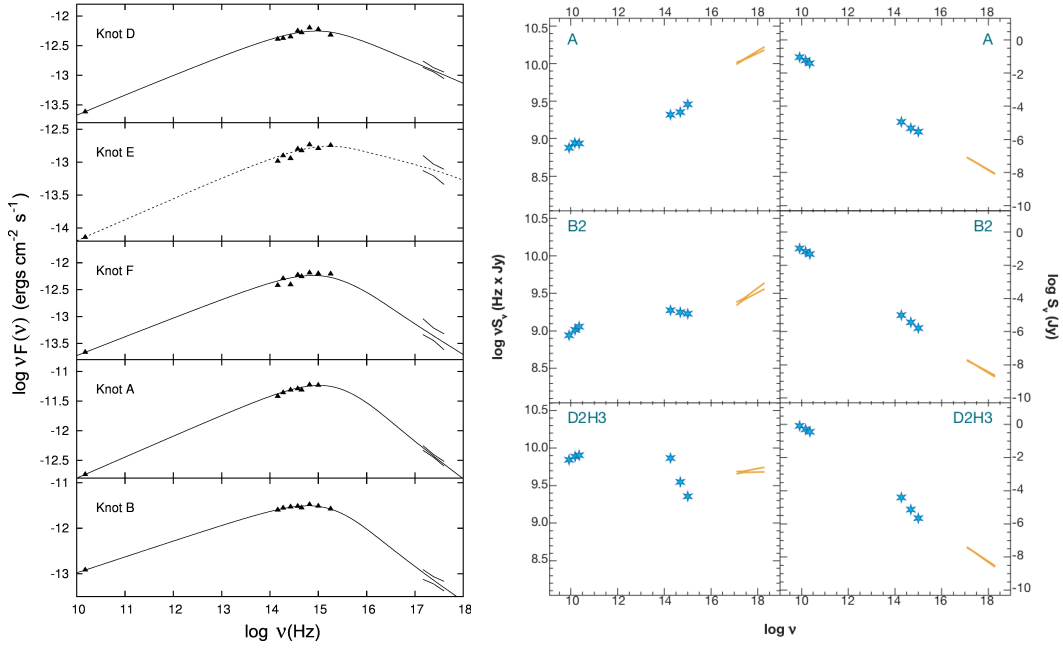


**Figure 3.1:** Left: The spectral fit for the knots of M 87 using synchrotron emission models from a power-law distribution of particles (Sahayanathan, 2008). Right: The spectral energy distribution of the knots A, B2 and D2H3 of 3C 273 (Jester et al., 2006).

demands a magnetic field that largely deviates from equipartition (Tavecchio et al., 2000; Harris & Krawczynski, 2006). However, the IC/CMB model requires the jets to be relativistic even at kpc scales so that in the knot frame, the ambient photon field is relativistically boosted to overpower the synchrotron photon energy density. Nevertheless, this interpretation can reproduce the observed X-ray flux from the knots and satisfies near equipartition magnetic field (Sahayanathan et al., 2003; Schwartz et al., 2000; Tavecchio et al., 2000). Fig 3.1 shows the harder X-ray spectral index for the knots of 3C 273 and the need for a second emission mechanism to interpret the X-ray emission.

Both IC/CMB and the synchrotron model can interpret the high energy emission from the knots with harder ( $\alpha_{ox} > \alpha_{ro}$ ) X-ray spectral index (Cara et al., 2013). Fig. 3.2 shows these models applied on the large-scale jet of PKS 1136-152. Both these interpretations demand different energy for the electrons and varied conditions on jet energetics and dynamics. The IC/CMB model requires high jet power, exceeding the Eddington luminosity, to reproduce the observed X-ray flux. However, because of its high radiative efficiency, the synchrotron interpretation neither demands the jet to be highly relativistic nor larger kinetic power (Dermer & Atoyan, 2004). However, an effective particle accelerator situated at a kpc scale distance away from the central engine of AGN is required to accelerate particles to PeV energies. Recent UV/optical polarimetric observations conducted on PKS 1136-135 noticed that many knots are highly polarised, suggesting synchrotron origin of high energy over IC/CMB (Cara et al., 2013). Therefore, distinguishing between the two possibilities is crucial for understanding the effects of quasar jets on its surrounding environment.

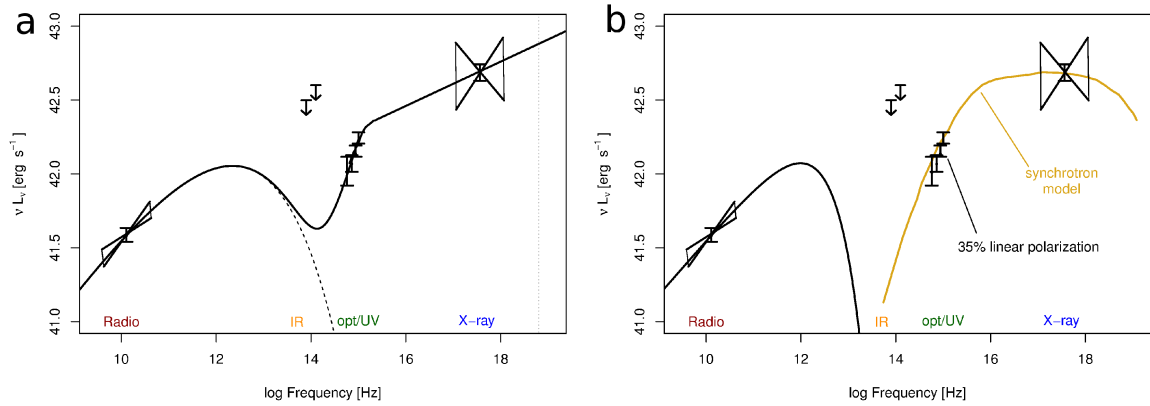


**Figure 3.2:** The observed SED (black points) of the jet of the quasar PKS 1136-135; the X-ray emission modelled using IC/CMB (a, black line) and second-synchrotron model (b, yellow line). The radio is modelled with synchrotron emission in both cases. Image credits: Cara et al. (2013); Georganopoulos et al. (2016).

### 3.2.2 *Fermi*/LAT observations: Implications on IC/CMB emission model

Modelling the X-ray knots through IC/CMB emission suggests that the spectral component peaks at  $\gamma$ -ray energies. Hence, a crucial prediction by the IC/CMB model is that the X-ray bright kpc scale jets of nearby AGN can be detectable by the *Fermi* space telescope operating at  $\gamma$ -ray energies (Georganopoulos et al., 2006). This was initially tested for 3C 273 and the *Fermi* upper limits on the gamma-ray flux from the large-scale jet (from 3 - 10 GeV) violates the IC/CMB model (Meyer & Georganopoulos, 2014). The flux upper limits were approximately a factor of ten less than the flux expected from the IC/CMB model calculated by extrapolating the UV to X-ray spectrum of knot A. This was again tested on PKS 0637-752 using six years of *Fermi* monitoring data. The study finds that the hard and steady gamma-ray emission, as expected from the IC/CMB model, is not seen in this prototype jet (Meyer et al., 2015), for which IC/CMB interpretation was first proposed for the X-ray emission (Tavecchio et al., 2000). Figure 3.3 shows the IC/CMB model curve and the *Fermi* gamma-ray flux upper limits for PKS 0637-752 and 3C 273.

*Fermi* ruled out IC/CMB interpretation of the X-ray jet in PKS 1136-135, PKS 1129-021, PKS 1354+195, and PKS 2209+080 as well (Breiding et al., 2017). The method of detecting the steady flux/upper limit from *Fermi* gamma-ray observations is described in detail in Meyer & Georganopoulos (2014) and Breiding et al. (2023). The *Fermi* Telescope cannot resolve the radiation from the core (highly variable and strong emission) or the large-scale jet (steady and low emission). To extract the steady and low level of IC/CMB gamma-ray flux, Meyer & Georganopoulos (2014) utilize the data when the core is in its most quiescent state. Lately, The IC/CMB model has been tested in 45 extragalactic X-ray jets using observational data from *Fermi*/LAT spanning ten years (Breiding et al., 2023). According to their investigation, the IC/CMB model has been ruled out for 24 MSC X-ray jets due to its overprediction for the observed gamma-ray flux in the MeV-to-GeV band. Two notable exceptions have been reported by Meyer et al. (2019). It is found that the minimum-detected gamma-ray flux level from the large-scale jet of OJ 287 and PKS 1510-089 agrees with the IC/CMB

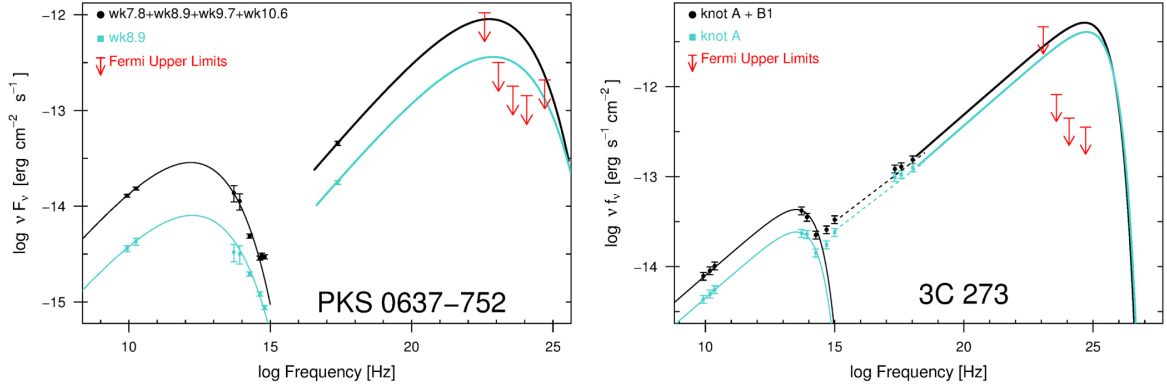


**Figure 3.3:** The observed SED (black points) of the knot/knots along with model curves and *Fermi* gamma-ray flux upper limits (left: PKS 0637-752; right: 3C 273). In both cases, even though IC/CMB model curve (second hump) predict gamma-ray emissions, it was not detected by *Fermi*.

predictions. The plateau signature observed in the recombined light curve of OJ 287 is consistent with the steady flux associated with the extragalactic jet. However, in the case of PKS 1510-089 this signature is not very evident and the measured minimum-flux can be from the core and not the jet. This can be clarified by long-term monitoring of the source.

### 3.2.3 The spine-sheath model for AGN Jets

High-resolution images of AGN jets in radio bands show a transverse jet with brighter edges than the centre spine, known as the Limb-brightened structure. This observation is typically attributed to the jet spine's higher velocity compared to its outer edge. According to Swain et al. (1998), in FR II sources, the jet emission is primarily from the shear layer. Whereas, in FR I sources, the spine emission becomes evident after the spine slows down a few kiloparsecs away from the AGN. The non-thermal X-ray emission along the large-scale jet of AGN implies that they must contain highly energetic particles (Harris & Krawczynski, 2006; Rieger et al., 2007; Georganopoulos et al., 2016). The favoured electron synchrotron explanation demands ultra-relativistic electrons with Lorentz factor of the order  $\gamma \sim 10^8$  (Sun et al., 2018). The short cooling length of these electrons (less than kpc), demands a continuous (re-) acceleration mechanism along the jet to keep the particles accelerated. One of the possible mechanisms is the stochastic and shear acceleration of particles in the stratified jet (Liu et al., 2017). More detailed discussions on the acceleration of charged particles in shearing flows are described in Rieger (2019).

### 3.2.4 Positional offset

The initial studies on knot emission were framed based on one-zone models. This proposes the emission in various frequencies (radio/optical/X-ray) to be co-spatial. It has been observed that this assumption is not valid due to changes in size and/or displacement between the radio and X-ray knots (Sambruna et al., 2004; Jester et al., 2006). In certain knots of FR II sources, X-rays that peaked

and decayed before the radio were previously documented (e.g., Kataoka et al. (2008); Clautice et al. (2016); Harris et al. (2017)) and in FR I sources, such as M87, comparable offsets between the radio and X-ray peak positions were also observed (Marshall et al., 2002).

Multiwavelength transverse and longitudinal jet structures of 3C 273 have been studied by Marchenko et al. (2017). The transverse jet profile is shown in Fig.3.4. The transverse intensity profiles of different knots reveal that the size of X-ray knots and their FUV counterparts are smaller than the widths of the corresponding segments in radio frequencies (see Fig 3.4 lower panel). Examining the longitudinal jet profile, it is found that the intensity peaks of the X-ray knots are

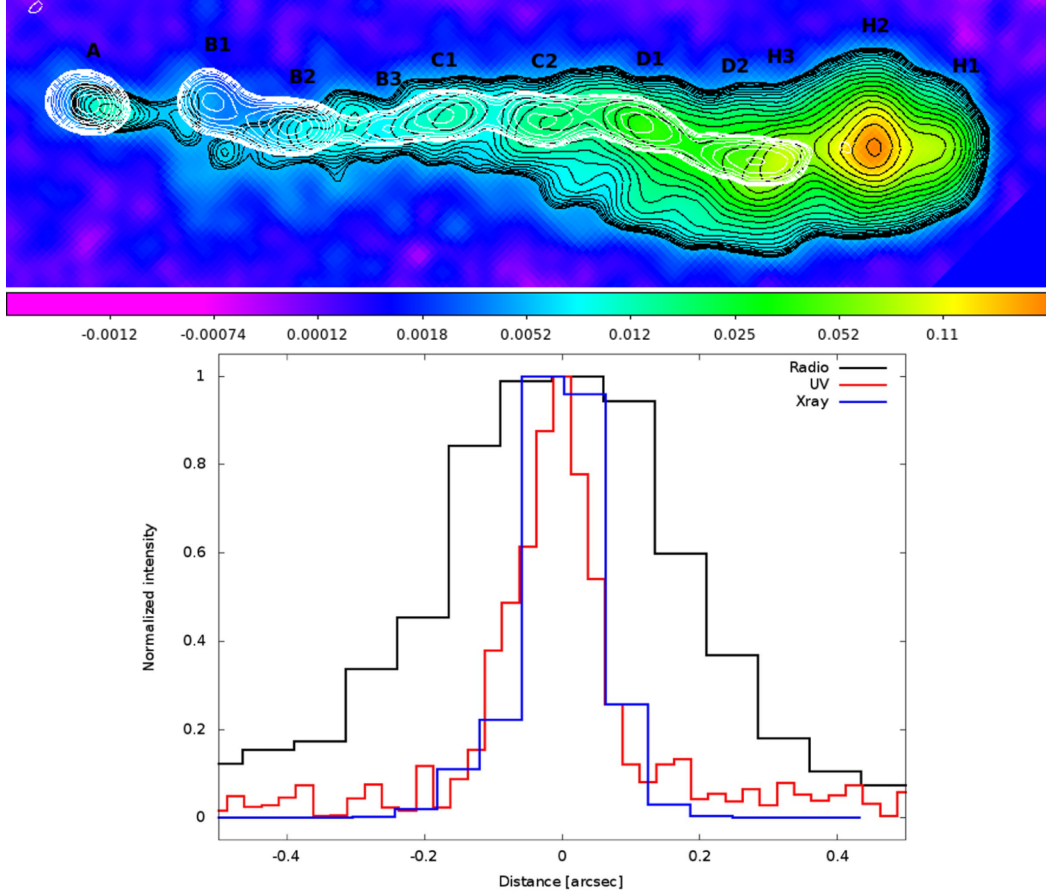


**Figure 3.4:** Upper: Transverse jet profile of 3C 273. Radio contours (black) superimposed over the deconvolved X-ray (white). Lower: The transverse intensity profile of knot A of 3C 273 at different frequencies (Marchenko et al., 2017).

located upstream of the corresponding radio intensity peaks. This positional offset is calculated using the formula

$$\Delta_{X/R} = \sqrt{(x_X - x_R)^2 + (y_X - y_R)^2} \quad (3.2.1)$$

where,  $(x_X, y_X)$  and  $(x_R, y_R)$  are the coordinates of X-ray and radio intensity peaks. The radio/X-ray offset measurements corresponding to different knots in the large-scale jet of 3C 273 is shown in Fig 3.5. Worrall (2009) suggests three possibilities associated with the longitudinal structure of knots. The X-ray intensity peak upstream of the radio peak as in 3C 273 and PKS 0637-752. The X-ray

peak is observed downstream of the radio as in 4C 19.44. In certain cases, intra-knot X-ray emission is also observed (eg: PKS 0605-085, 0838+133 and 1136-135). In a few cases, the radio and X-ray knots appear co-spatial as well.

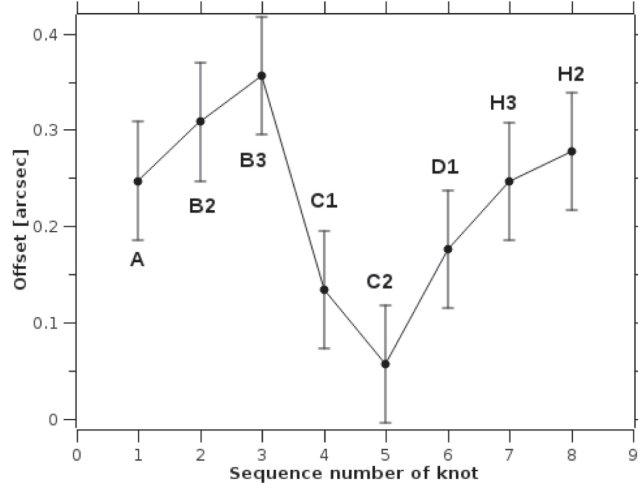


**Figure 3.5:** Positional offset between radio/X-ray intensity peaks of 3C 273 knots (Marchenko et al., 2017).

The major limitation in detecting offset in the case of knots is the low number of X-ray counts and the resulting statistics. Recently, using a statistical tool namely, Low-count Image Reconstruction and Analysis (LIRA; Esch et al. (2004); Stein et al. (2015)) offset has been detected in the low-count X-ray jets (Reddy et al., 2023). They present a comparison between the X-ray and radio maps of 164 jet components and find offsets in 57% of the sample. The knots in FR II type sources predominantly show Xf-type (X-ray upstream of radio) offsets. This X-ray peaking and decaying before the radio suggests spatially separated emitting regions.

### 3.2.5 X-ray Variability

The surprising discovery of flux variability in the X-ray jet of Pictor A (Marshall et al., 2010; Hardcastle et al., 2016) have significantly contributed to our understanding of the particle acceleration and emission mechanisms associated with kilo-parsec scale jets. A jet measuring 150 kpc long and 1 kpc wide fluctuating over a year is unusual. If the high energy emission has a synchrotron origin, the electrons that release X-rays have a synchrotron loss time of around 1200 years. This suggests that X-ray emission originates from a very tiny volume of the jet, with a characteristic magnetic field larger than the average of the jet.

Recently, Meyer et al. (2023) identified X-ray variability through their archival analysis of several observations of X-ray jets at the kiloparsec scale. The statistical analysis was done using all known X-ray jets that were imaged more than once by the Chandra Advanced CCD Imaging Spectrometer (ACIS) instrument. The observed variability in X-ray emission over timescales of months to years contradicts the predictions of the IC/CMB mechanism.

### 3.2.6 Polarization

The magnetic field plays a crucial role in the propagation and bulk acceleration of the jets of active galactic nuclei. Polarization measurements provide vital insights into the internal magnetic structures. The kilo-parsec scale jet of M 87 shows high polarization. The linear polarization images of this jet were first presented by Schmidt et al. (1978). Clear differences between the radio and optical polarization structures have been observed in the knots HST-1, D, E, and F (Perlman et al., 1999). The projected magnetic field is mostly parallel to the jet at both radio and optical wavelengths. However, it becomes perpendicular at the upstream ends of bright knots at optical wavelengths. This implies that optical emissions originate from the shocks in the jet interiors and radio emission is predominantly by the shear layers at the jet surface.

The combination of multiband imaging and polarimetry can be an effective diagnostic tool for understanding jet emission processes. The deep imaging photometry of the jet of PKS 1136-135 using the Hubble Space Telescope shows strong optical polarization, with fractional polarization exceeding 30% (Cara et al., 2013). The observed high polarization strongly disfavors the IC/CMB interpretation and suggests synchrotron origin for the jet emission for PKS 1136-135. The jet of 3C 273, PKS 0637-752 and 1150+497 shows moderately to highly polarized components in optical waveband (Perlman et al., 2020). In the case of 1150+497 and PKS 0637-752, the polarized optical emissions originate from X-ray and optical knot maxima, as seen in PKS 1136-135. Whereas in the case of 3C 273, the highly polarised emissions are observed at the jet edge in knots B2 through D and knot maxima show low polarisation. Future observations from high-angular resolution X-ray polarimeters, like the Imaging X-ray Polarimetry Explorer (IXPE, Weisskopf et al. (2022)), could provide independent evidence in probing the IC/CMB model. However, IXPE's huge PSF may limit its application to larger jets, such as Pictor A's hotspot.

## 3.3 MHD Simulations of large-scale jet

To better understand the properties of AGN jets and simulate their various morphologies (Komissarov Porth 2021), researchers have studied the problem from the hydrodynamic (HD) limit to the relativistic magneto-hydrodynamic (RMHD) extension. It is still an open question how the jet's evolution and dynamics impact the various emission mechanisms. Earlier studies used semi-analytic modelling of jet expansion to describe jet dynamics and explain observed emission (Begelman & Cioffi, 1989; Kaiser & Alexander, 1997; Bromberg & Levinson, 2009; Turner & Shabala, 2015; Harrison et al., 2018; Hardcastle, 2018). However, with advancements in numerical schemes to simulate relativistic flows, an extensive investigation has been done on the dynamics of relativistic jets as they expand into the ambient medium (Martí et al., 1997; Komissarov, 1999; Perucho & Martí, 2007; Mignone et al., 2010; Perucho et al., 2019). Mukherjee et al. (2020) examine the impact of various MHD instabilities on jet dynamics and their relationship with the choices of jet parameters. They find two major MHD instabilities that can impact jet dynamics, namely, small-scale Kelvin-Helmholtz (KH) modes and large-scale kink modes. The low power jets are susceptible to both instabilities

and higher power jets are stable in both. Meenakshi et al. (2023) investigate the impact of the jet's immediate surroundings on non-thermal synchrotron emission and polarization. Giri et al. (2023) model the X-shaped radio galaxies (XRGs) using 3D relativistic magnetohydrodynamic simulations.

### 3.4 VHE emission from large-scale jets

The extragalactic sky at high energy and very high energy gamma rays is highly dominated by blazars, the sources whose relativistic jet points towards the observer. The flux enhancement of intrinsic non-thermal emission due to relativistic Doppler boosting effects favours their detection in this regime. However, *Fermi*/LAT detected about 20 radio galaxies in the high-energy gamma range. Out of them, 6 were found as VHE emitters, which includes M 87, Cen A, NGC 1275, 3C 264, IC 310 and PKS 0625-35 (Rieger & Levinson, 2018). Among these, IC 310 and PKS 0625-35 display both radio galaxy and blazar characteristics (Rulten, 2022). Unlike blazars, the jets of the radio galaxies/misaligned AGNs are oriented at larger angles to the line of sight and hence are characterised by lesser Doppler boosting. The discovery of radio galaxies at VHE opens up insights into fundamental non-thermal emissions from gamma-ray emitting AGNs. The misaligned geometry of radio galaxies provides us with a unique view of the AGN jet and the supermassive black hole (SMBH). The detection of TeV gamma rays from such galaxies is indeed a motivation for future observations and poses further questions on jet orientation, the sites of particle acceleration and gamma-ray emission, the possibilities of knots emitting in VHE, the jet content (leptonic/hadronic) responsible for VHE gamma-ray emissions etc.

### 3.5 Conclusions

The recent X-ray (variability and polarization) and gamma-ray (*Fermi* upper limit estimates) observations associated with the kilo-parsec/Mega-parsec scale jet of AGN strongly suggest synchrotron emission from the second population of electron distribution as the possible origin for their high energy emission. The positional offset between radio and X-ray emission peaks demands the emitting regions to be not co-spatial. In **Chapter 4** of this thesis, we examine the possible origin of this spatially separated two-population model of particle distribution.

Even though the IC/CMB model was ruled out for many sources in the local universe by *Fermi* gamma-ray observations, it was still accepted to be the mechanism governing the X-ray emission from the jet of high redshift AGN. However, recent *Fermi* gamma-ray observations ruled out IC/CMB model for high redshift sources as well. In **Chapter 5**, we extend the two population model discussed in Chapter 4 to high redshift sources to interpret the MSC emission from their large-scale jets.

The motive for the work presented in **chapter 6** of this thesis is the recent discovery of a number of radio galaxies emitting in high energy and VHE band (Paliya et al., 2024). In this work, extrapolating the IC/CMB model to VHE energies, we look for the radio galaxies with misaligned jets which are probable VHE candidates for the upcoming Cherenkov Telescope Array Observatory.



# Chapter 4

## Advection of Accelerated Electrons in Radio/X-ray Knots of AGN Jets

---

### 4.1 Introduction

The knots of the AGN jet have been well resolved in radio and optical wavebands. With the advent of *Chandra*, with its superior spatial resolution, today we know most of these knots are even bright in X-rays. The mechanism responsible for radio-to-optical emission from the knots are understood to be a synchrotron process; where a relativistic electron distribution loses its energy as radiation in the jet magnetic field (Kataoka & Stawarz, 2005; Zhang et al., 2010). However, the X-ray emission process is modelled either as a synchrotron or inverse Compton scattering of soft target photons depending upon the hardness of optical-to-X-ray spectral index ( $\alpha_{ox}$ ) in comparison to radio-to-optical spectral index ( $\alpha_{ro}$ ) (Jester et al., 2006).

The X-ray emission from the knots of kilo-parsec scale jets of AGN, when attributed to the inverse Compton process; viable source of the target photons can be the synchrotron photons themselves. This is commonly referred to as Synchrotron Self Compton (SSC) process. However, this interpretation is disfavored since it demands a magnetic field that deviates largely from the equipartition condition (Harris & Krawczynski, 2006; Zhang et al., 2010). Modelling the X-ray knots through IC/CMB emission suggests this spectral component peaks at  $\gamma$ -ray energies. However, the recent observations by the *Fermi* space telescope operating at  $\gamma$ -ray energies rule out the possibilities of IC/CMB in interpreting the X-ray emission (details in section 3.2.2).

Failure of the IC/CMB model to explain the *Fermi*  $\gamma$ -ray upper limit favors the presence of a second electron population which is responsible for the observed X-ray emission from the knots. If we assume the electrons are accelerated at the knot sites by a shock front, then the particle injection into the upstream and the downstream region will be asymmetric due to the compression of the downstream fluid (Liu et al., 2015). This can develop two independent electron populations and can explain the radio-to-X-ray emission from the knots successfully. Alternatively, electrons can be accelerated to ultra-high energies at the sheared boundary of the jets in addition to the shock acceleration (Tavecchio, 2021). Under this scenario, the electrons accelerated at the shock front contribute to radio-optical emission; while the X-ray emission is produced by the electrons undergoing shear acceleration.

The drawback of the second electron population interpretation of the X-ray knots is, it demands

ultra-high energy electrons which are subject to fast cooling (Wang et al., 2020). Hence, these electrons would expend all their energy close to their production site itself and may not explain the extended X-ray emission from the knots. Wang et al. (2020), therefore, suggested a lepto-hadronic origin for the radio-to-X-ray emission for the knots. The radio-to-X-ray emission from the knot can also be explained by models involving emission from hadrons alone (Kundu & Gupta, 2014). Advantages of models involving the X-ray emission from hadrons is that they lose their energy much slower than the leptons and therefore can diffuse over long distances.

In this chapter, we present an emission scenario for the knots where the advection of electrons from the main acceleration site is considered. This can produce two distinct electron populations with a high-energy electron distribution arising from the acceleration site and a low-energy one surrounding it. The synchrotron emission from such combined electron distribution is capable of explaining the radio-to-X-ray emission from the knots of the jet of 3C 273. In the next section, we deduce the advected electron population and explain the total synchrotron spectrum. In section 3, we apply this model to the knots of 3C 273 and discuss the results. Throughout this work, we consider a cosmology where  $H_0 = 71 \text{ km s}^{-1} \text{ Mpc}^{-1}$ ,  $\Omega_m = 0.27$  and  $\Omega_\Lambda = 0.73$ .

## 4.2 The Two-Population Model

We consider a model in which the particle acceleration in the AGN knot is confined within a spherical region of size  $R_0$ . The electron distribution in this region is assumed to be a broken power-law described by

$$n_0(\gamma)d\gamma = \begin{cases} K\gamma^{-p}d\gamma & \gamma_{\min} < \gamma < \gamma_b \\ K\gamma_b^{q-p}\gamma^{-q}d\gamma & \gamma_b < \gamma < \gamma_{\max} \end{cases} \quad (4.2.1)$$

Such an electron distribution can be an outcome of multiple acceleration sites embedded within  $R_0$  (Sahayanathan, 2008; Pope & Melrose, 1994). The accelerated electrons are advected outside  $R_0$  where they do not undergo further acceleration but lose their energy through radiative processes and adiabatic cooling. We consider the magnetic field at the regions  $R < R_0$  and  $R > R_0$  as  $B_{in}$  and  $B_{out}$  respectively. The schematic diagram representing the knot model is given in Fig. 4.1.

The evolution of the electron distribution in the region  $R > R_0$  can be described by (Kardashev, 1962; Atoyan & Aharonian, 1997)

$$\frac{\partial n(\gamma, t)}{\partial t} = \frac{\partial}{\partial \gamma} [P(\gamma) n(\gamma, t)] - \frac{n(\gamma, t)}{t_{\text{esc}}(\gamma, t)} + q(\gamma) \quad (4.2.2)$$

Here,  $P(\gamma)$  is the total energy loss rate due to radiative processes and adiabatic expansion,  $t_{\text{esc}}(R)$  is the electron escape timescale at a distance  $R$  from  $R_0$  and  $q(\gamma)$  is the rate of electron injection (Ginzburg & Syrovatskii, 1964). We express the advection term in terms of  $t_{\text{esc}}$  as follows: for a constant velocity  $v$ , the advection can be expressed as  $-v \frac{\partial n}{\partial R}$  (changing variable from  $t$  to  $R$ ). Hence

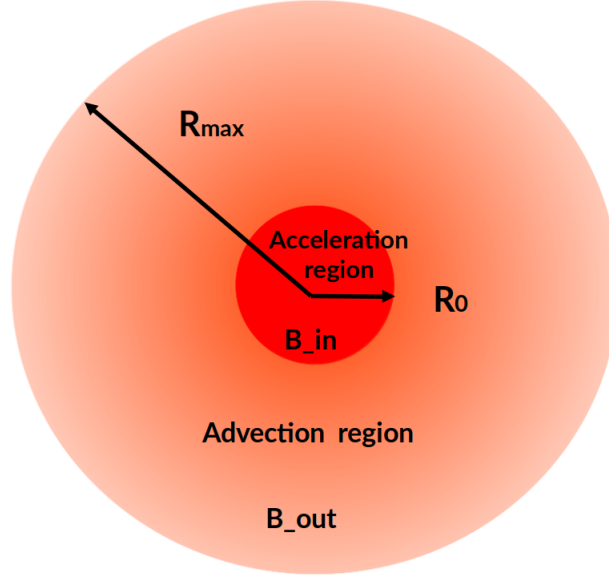


**Figure 4.1:** The schematic diagram of the knot considering the advection of particles from the sites of particle acceleration.

we get,

$$-\frac{\partial n}{\partial t} \approx -\frac{n}{t_{esc}(R)} \quad (4.2.3)$$

Considering the linear dependence of  $R$  on  $t$  and the injection of accelerated electron distribution at  $R = R_0$ , equation (4.2.2) can be expressed as

$$\frac{\partial \bar{n}(\gamma, R, R_0)}{\partial R} = \frac{\partial}{\partial \gamma} [\bar{P}(\gamma, R) \bar{n}(\gamma, R, R_0)] - \frac{\bar{n}(\gamma, R, R_0)}{R_*(R)} + n_0(\gamma) \delta(R - R_0) \quad (4.2.4)$$

where  $R_*$  is the characteristic particle escape radius corresponding to  $t_{esc}$  and

$$\begin{aligned} \bar{P}(\gamma, R) &= \frac{d\gamma}{dR} \\ &= \xi \gamma^2 + \frac{\gamma}{R} \end{aligned} \quad (4.2.5)$$

where  $\xi$  will be a function of the magnetic field and the velocity of the fluid (Rybicki & Lightman, 1986; Atoyan & Aharonian, 1997).

The solution (for  $R > R_0$ ) of equation (4.2.4) can be obtained through the Green's function method as (Atoyan & Aharonian, 1997)

$$\bar{n}(\gamma, R, R_0) = \frac{R_0 \Gamma_0^2}{R \gamma^2} n_0(\Gamma_0) \exp \left[ - \int_{R_0}^R \frac{dx}{R_*(x)} \right] \quad (4.2.6)$$

where  $\Gamma_0$  defines the energy of the electron at injection radius  $R_0$  which reduces to  $\gamma$  at  $R$  due to

radiative and adiabatic losses. From equation (4.2.5) we find

$$\Gamma_0(\gamma, R) = \frac{\gamma \frac{R}{R_0}}{1 - \xi \gamma R \ln \frac{R}{R_0}} \quad (4.2.7)$$

The maximum distance  $R_{\max}$  up to where electrons with energy  $\gamma$  will be available and can be obtained by numerically solving the transcendental equation

$$\frac{R_{\max}}{R_0} = \frac{\gamma_{\max}}{\gamma} \left[ 1 - \xi \gamma R_{\max} \ln \left( \frac{R_{\max}}{R_0} \right) \right] \quad (4.2.8)$$

and

$$R_{\max}(\gamma) \leq R_0 + \frac{1}{\xi} \left( \frac{1}{\gamma} - \frac{1}{\gamma_{\max}} \right) \quad (4.2.9)$$

where the inequality is obtained by considering only radiative losses. We assume the escape radius as

$$R_*(R) = \zeta R^\alpha \quad (4.2.10)$$

where  $\zeta$  and  $\alpha$  are constants. For  $\alpha = 1$ , the advected electron distribution in the region external to  $R_0$  will be

$$\bar{n}(\gamma, R, R_0) = \frac{R_0}{R} \frac{\Gamma_0^2}{\gamma^2} n_0(\Gamma_0) \left( \frac{R_0}{R} \right)^{1/\zeta} \quad (4.2.11)$$

In Fig. 4.2 we show the distribution of  $\bar{n}$  for different  $\frac{R}{R_0}$ . The general solution for  $\alpha \neq 1$  is given as

$$n(\gamma, R, R_0) = n_0(\Gamma_0) \frac{\Gamma_0^2}{\gamma^2} \exp \left[ \frac{-1}{\zeta(-\alpha + 1)} \left( R^{-\alpha+1} - R_0^{-\alpha+1} \right) \right] \quad (4.2.12)$$

## 4.2.1 Synchrotron Spectrum

The total number of electrons with energy  $\gamma$  from the regions  $R < R_0$  and  $R > R_0$  can be obtained from equations (4.2.1) and (4.2.11) as

$$N_{\text{tot}}(\gamma) = \frac{4}{3} \pi R_0^3 n_0(\gamma) + 4\pi \int_{R_0}^{\text{MIN}(R_{\max}, R_{\text{size}})} \bar{n}(\gamma, R, R_0) R^2 dR \quad (4.2.13)$$

where  $R_{\text{size}}$  is the size of the knot. In Fig. 4.3, we plot the distribution of the advected electron population for different choices of  $\zeta$ . The total electron distribution from the acceleration and advection region is shown in Fig. 4.4. The synchrotron emissivity at frequency  $\nu$  can be obtained by convolving the total electron distribution with the single particle emissivity  $j_{\text{syn}}(\gamma, \nu)$  (Rybicki

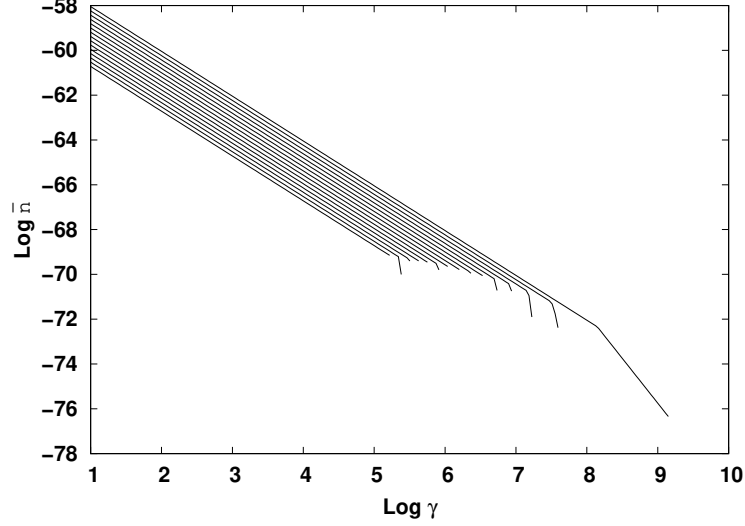


**Figure 4.2:** The advected electron distribution at different  $R > R_0$  for the values of  $\frac{R}{R_0}$  between 1 and 100. The parameters chosen are of knot A. The top most line corresponds to  $\frac{R}{R_0} = 1$

& Lightman, 1986)

$$J_{\text{syn}}(\nu) = \frac{1}{4\pi} \int_{\gamma_{\text{min}}}^{\gamma_{\text{max}}} j_{\text{syn}}(\gamma, \nu) N_{\text{tot}}(\gamma) d\gamma \quad (4.2.14)$$

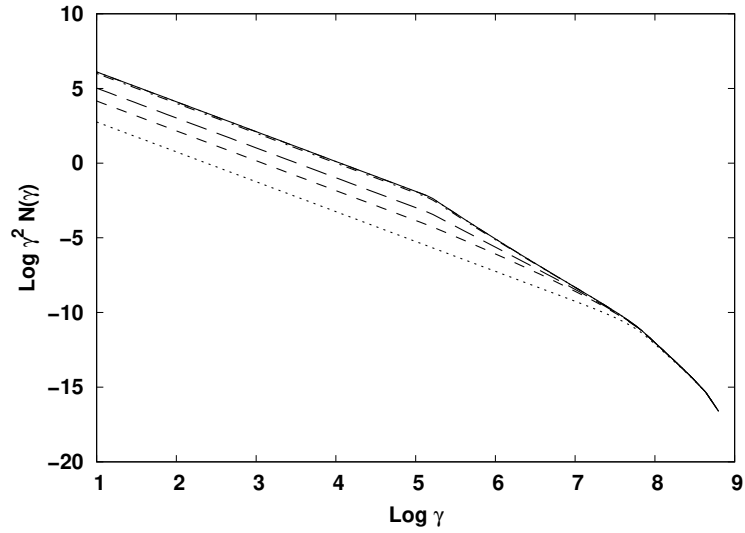


**Figure 4.3:** Advected electron population for different  $\zeta$  in the case of knot A. Solid line corresponds to  $\zeta=100$  and dotted line to  $\zeta=0.1$ . All other plots below solid line correspond to  $\zeta=50, 10, 1$  &  $0.5$ .

The observed flux on earth after accounting for the relativistic effects of jet and cosmological corrections will be

$$F_{\text{obs}}(\nu_{\text{obs}}) = \frac{\delta_D^3 (1+z)}{d_L^2} J_{\text{syn}} \left( \frac{1+z}{\delta_D} \nu_{\text{obs}} \right) \quad (4.2.15)$$

Here,  $d_L$  is the luminosity distance and  $\delta_D$  is the Doppler factor given by

$$\delta_D = \frac{1}{\Gamma(1 - \beta \cos \theta)} \quad (4.2.16)$$

with  $\Gamma$  being the bulk Lorentz factor,  $\beta c$  the velocity and  $\theta$  the viewing angle of the relativistic jet.

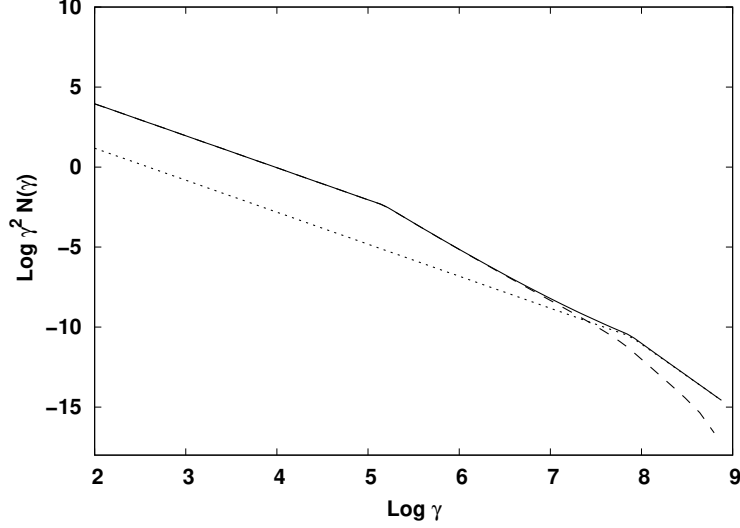


**Figure 4.4:** The electron distribution for the knot A of 3C 273. The dotted line represents accelerated particle distribution and the dashed line the advected electron distribution. The solid line is the total particle distribution.

### 4.3 Results and Discussion

The model described above, incorporating the advection of electrons from the sites of particle acceleration, is used to reproduce the radio/optical/X-ray fluxes from the knots of 3C 273. The primary accelerated electron distribution is assumed to be a broken power-law and confined within a region  $R < R_0$  with magnetic field  $B_{in}$  (equation(6.3.1)). The synchrotron emission by this electron distribution is used to model the X-ray flux from the knots of 3C 273. The advected electron distribution from the region  $R > R_0$  creates a low energy excess and the synchrotron emission from this electron population can reproduce the observed radio fluxes.

In Fig. 4.5, we show the observed radio–optical–X-ray spectrum from the knots A, B1, B2, B3, C1, C2, D1 and D2H3 along with the model curves. The dot-dash line is the synchrotron emission from the accelerated electron distribution while the dotted line is from the advected electron population. The total emission is shown as a solid line. The parameters used to reproduce the model curves are given in Table 4.1. Besides these parameters, we have assumed  $\alpha = 1$ ,  $\gamma_{min} = 10$ ,  $\gamma_{max} = 10\gamma_b$  and  $\theta = 20$  degrees.

The choice of model parameters also decides whether the IC scattering of CMB photons by the total electron distribution will exceed the *Fermi* upper limits. To verify this we estimate IC/CMB spectral component using approximate analytical solution for a monochromatic external photon field

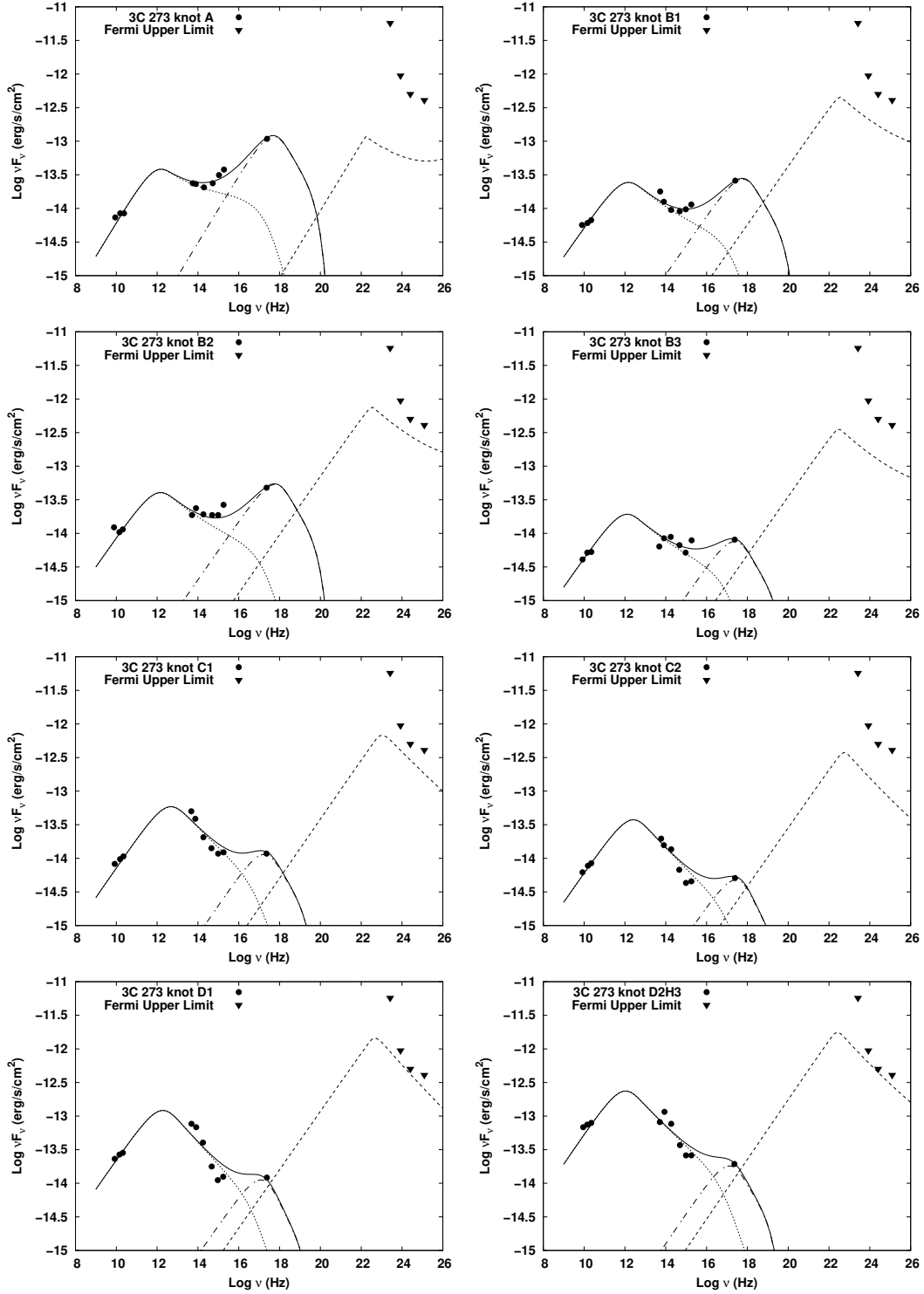


**Figure 4.5:** Observed broadband SEDs of the knots of 3C 273 together with the model curves. Solid circles represent the observed broadband SEDs of the knots of 3C 273. Dot-dash line represents the synchrotron emission from the accelerated electron population, the dotted line represents synchrotron emission from the advected electron population and the solid line represents the total synchrotron emission. The dashed line corresponds to the IC/CMB spectrum and *Fermi* upper limits are denoted by inverted triangles.

(Sahayanathan et al., 2018). The IC/CMB emissivity at frequency  $\nu$  can be expressed as

$$j_{ec}(\nu) \approx \frac{c\sigma_T U_*}{8\pi\nu_*} \sqrt{\frac{\Gamma\nu(1+\mu)}{\nu_*}} N_{\text{tot}} \left[ \sqrt{\frac{\nu}{\Gamma\nu_*(1+\mu)}} \right] \quad (4.3.1)$$

Here,  $\nu_*$  and  $U_*$  are the frequency and the energy density of the external photon field and  $\mu$  is the jet viewing angle measured in the proper frame of the AGN. In Fig. 4.5, the spectral energy distribution due to IC/CMB emission is shown as a dashed line. For the choice of parameters given in Table 4.1, the spectrum due to IC/CMB falls below the *Fermi* upper limits.

Knot	$R_0(kpc)$	$R_{size}(kpc)$	$B_{in}(10^{-5}G)$	$\omega = \frac{B_{in}}{B_{out}}$	$\gamma_b(10^7)$	$v_{ad}(10^{-2}c)$	$p$	$q$	$\Gamma$	$\zeta$
A	0.12	2.9	1.5	2.08	7.5	2.0	2.0	4.0	1.3	7.0
B1	0.10	5.5	1.8	3.3	6.5	1.6	2.13	4.0	2.0	7.0
B2	0.10	5.50	2.0	3.6	6.18	1.6	2.13	4.0	2.0	7.0
B3	0.09	5.5	1.3	2.4	4.85	1.6	2.13	4.0	2.0	7.0
C1	0.08	8.0	1.9	3.45	3.64	9.0	2.12	4.0	1.7	5.5
C2	0.05	6.0	1.9	3.17	4.70	5.0	2.13	4.2	1.7	9.5
D1	0.05	6.0	1.5	3.0	3.58	4.0	2.13	4.2	1.6	9.5
D2H3	0.05	6.5	1.1	2.4	4.62	2.5	2.11	4.0	1.3	9.5

**Table 4.1:**  $R_0$  is the size of the inner region;  $R_{size}$  is the size of the knot;  $B_{in}$  and  $B_{out}$  represent the magnetic field strength at  $R < R_0$  and  $R > R_0$  respectively. The quantities  $\gamma_b$ ,  $v_{ad}$ ,  $p$ ,  $q$ ,  $\Gamma$  and  $\zeta$  represent the break energy, advection velocity, power law indices of broken power law distribution of particles, bulk Lorentz factor and the constant defining escape radius respectively.

In this work, we have assumed the accelerated electron distribution to be a broken power law and this can be an outcome of multiple acceleration processes (Sahayanathan, 2008). For instance, if we consider the case where the particle acceleration happens due to a standing shock buried in a turbulent plasma, then the electrons injected into the shock front are already accelerated under the stochastic process. If the confinement time at the turbulent region is longer than the region in the vicinity of the shock front, the electron distribution accelerated through the stochastic process will be harder (Rieger et al., 2007). This eventually give rise to a broken power law distribution with indices governed by the ratio of acceleration to escape timescales in both regions.

The model considered here demands large electron energies to explain the X-ray emission. Such large electron energies can be achieved under moderate loss or escape time scales. If we assume the escape timescale is governed by gyro radius ( $R_g$ ), then for an electron with Lorentz factor  $10^8$ ,  $R_g$  is  $10^{-3}pc$ , which is much smaller than the size of inner region  $R_0$ . Similarly, the acceleration timescale for the given gyro-radius is approximately  $R_g/c$  and is of the order of  $10^5$  s (Inoue & Takahara, 1996; Kusunose et al., 2000). Whereas, the synchrotron radiative loss time scale for electrons of energy  $\approx 10^8$  is of orders of  $10^9$ s. Hence, the acceleration of electrons to such high energies is viable under the scenario considered here.

It is interesting to study the radial evolution of the advected electron distribution which is



governed by the synchrotron and adiabatic cooling (Fig. 4.2). The integrated distribution over  $R$  in combination with the accelerated electron distribution will then reflect a convex (concave upward) shape which can explain the radio–optical–X-ray spectrum of AGN knots (Fig. 4.4). The radial evolution of the advected electron distribution also depends up on the choice of  $\alpha$ . In the present study,  $\alpha$  is chosen to be unity for simplicity; however, the observed knot spectrum can also be explained with  $\alpha \neq 1$  and a modified set of parameters.

The synchrotron cooling time scale estimated for the radio, optical and X-ray emitting electron (for the case of  $B \approx 10^{-5}$ ) is approximately  $10^{14}$ s,  $10^{12}$ s, and  $10^{10}$ s respectively (Atoyan & Aharonian, 1997). The equivalent length scale can be estimated as 100 kpc (radio), 1 kpc (optical) and 10 pc (X-ray) for a velocity  $v \approx 0.1c$ . This suggests the radio emitting electrons will travel the extended jet before losing its energy as compared to the X-ray emitting electrons. This is consistent with the morphological feature of the source where the radio jet extends over large scales whereas the X-ray emission dies out beyond the knot locations (Harris & Krawczynski, 2006).

*Fermi* non-detection of gamma-ray emission from the knots of AGN jets favoured the two-electron population hypothesis for the radio–to–X-ray emission. Nevertheless, the IC/CMB model for the X-ray emission is still preferred for the sources which are not yet ruled out by *Fermi* observations (Ighina et al., 2021a; Worrall et al., 2020; Kharb et al., 2012). Irrespective of *Fermi* observations, the IC/CMB model for the X-ray emission fails to explain many morphological features of the AGN jet. For example, the electron energies required to produce the X-ray emission through the IC/CMB process is similar to the ones emitting radio through the synchrotron process. Hence, the radio/X-ray jet morphology should be comparable (Harris & Krawczynski, 2006). On the contrary, positional offset has been detected between the radio and X-ray maxima for the knots of many AGN (Hardcastle et al., 2003; Bai & Lee, 2003). Similarly, the IC/CMB model demands significant jet speed to explain the X-ray emission which in turn predicts one-sided jets due to relativistic debeaming of the counter jet. However, the detection of faint counterjet in Pictor A disfavors the IC/CMB origin of the X-ray emission (Hardcastle et al., 2016).

The explanation for the radio–to–X-ray flux from the knots of many AGN jets through the synchrotron process suggests the underlying electron distribution to be convex (concave upward). Production of such a distribution demands an acceleration process that can provide excessive power at high electron energies. Alternatively, the synchrotron emissions from two spatially separated electron populations are capable of explaining the radio–to–X-ray emission from the AGN knots. In this work, we show such distributions can naturally arise if we incorporate the advection of accelerated electrons from the sites of particle acceleration. The synchrotron emission received from the combination of accelerated and advected electron distributions is used to model the radio/optical/X-ray fluxes from the knots of 3C 273. The model parameters are chosen to reproduce the observed fluxes while the predicted IC/CMB emission falls within the *Fermi* upper limits.

The model assumes the accelerated electron distribution to occupy a spherical region and the advected electrons in a spherical shell around it. If we relax this spherical symmetry, the proposed model is also capable of explaining the observed offsets between the radio, optical and X-ray knot

positions. Reproduction of the radio, optical and X-ray observations of the knots of 3C 273 using this model suggests the spectral energy distribution of these knots to peak at infrared frequencies. High-resolution observation at this frequency in future has the potential to constrain/rule out the model presented in this work.

# Chapter 5

## X-ray Emission from Large Scale Jets of AGNs at High Redshifts

---

### 5.1 Introduction

The AGN population at high redshifts have been widely studied to uncover our understanding of the early universe (Fan et al., 2020; Bañados et al., 2016; Jiang et al., 2016; Shen et al., 2020; Zhang et al., 2022). Even though a large population of quasars was discovered at high redshifts; only a few radio-loud AGNs are known so far (Sbarrato et al., 2022). It is well established that, at lower redshifts, 10% – 20% of the quasars are radio-loud. The radio-loud fraction of quasars is suggested to be a function of both optical luminosity and redshift (Padovani, 1993; La Franca et al., 1994; Hooper et al., 1995). However, certain studies also find that there is no evolution of the radio-loud fraction with redshift (Bañados et al., 2015). Similarly, studies on the FSRQ population has been performed to understand their space density evolution. While Ajello et al. (2009) suggest it peaks at a redshift of  $4.3 \pm 0.5$ ; a later study on a different sample shows an evolutionary peak at  $z \sim 1 - 2$  (Toda et al., 2020). Nevertheless, bolometric quasar luminosity studies were done for radio-quiet sources up to a redshift of  $z = 7$  (Hopkins et al., 2007; Shen et al., 2020).

The observed superluminal motion in the jet suggests they are relativistic and also gives clues on the viewing angle (Rybicki & Lightman, 1986; Ghisellini et al., 1993). AGNs whose jet is aligned at larger angles to the observer are classified as misaligned active galactic nuclei (MAGN) (Urry & Padovani, 1995; Antonucci, 1993). Because of their orientation, MAGNs are well projected into the sky plain, and their extended morphology is visible and resolved in various wavebands. Interestingly, two extreme radio-loud quasars at high redshift ( $z > 4$ ) namely, J1420+1205 and J2220+0025 were classified as blazars based on their X-ray emission properties (Sbarrato et al., 2015). Nevertheless, the VLBI observations of these two sources suggest their radio characteristics were quite distinct from those of blazars. Their morphologies resemble a double-lobed radio AGN, suggesting their jets to be oriented at larger angles to the line of sight (Cao et al., 2017). This inconsistency showcases the difficulties in exploring the jet orientation at high redshifts.

The MSC observations of the population of misaligned AGN sources are mostly done in the nearby universe ( $z < 1$ ). Recently, kilo-parsec scale jets at higher redshifts have been identified and studied (Belladitta et al., 2020; Hodges-Kluck et al., 2021; Snios et al., 2021; Ighina et al., 2022;

Kreuzinger et al., 2022). Moreover, Schwartz et al. (2020) reported the detection of extended X-ray emission from two high redshift radio quasars namely, J1405+0415 ( $z = 3.208$ ) and J1610+1811 ( $z = 3.118$ ), with no signature of continuous radio jets. Such discrepancies highlight the need for multiwavelength observations and detailed SED modelling of the large-scale jet.

Unlike the nearby universe, at high redshifts, the IC/CMB interpretation of X-ray emission is still preferred due to the increase in CMB energy density ( $U_{CMB} \propto (1+z)^4$ ) (Harris & Krawczynski, 2002). Hence, studies on jets of AGN at high redshifts can be a tool to explore the validity of this model (Snios et al., 2021; Zhang et al., 2022; Snios et al., 2022). The resolved X-ray jet of PKS J1421-0643 at  $z = 3.69$  was modelled with the IC/CMB interpretation (Worrall et al., 2020). Recently, *Chandra* detected the X-ray observation from the most distant kilo-parsec jet at  $z = 6.1$  and find the emission to be consistent with the IC/CMB model (Ighina et al., 2022).

3C 273 is the first large-scale jet for which IC/CMB interpretation was ruled out with  $\gamma$ -ray flux upper limit values deduced from *Fermi*/LAT observations (Meyer & Georganopoulos, 2014). Later, the  $\gamma$ -ray flux upper limits of various other sources were estimated especially in the nearby universe (Meyer et al., 2015; Breiding et al., 2017). Recently, Breiding et al. (2023) examined the IC/CMB interpretation for 45 extra-galactic X-ray jets and they found that the IC/CMB model is questioned in 27 MSC X-ray jets due to over-prediction for the observed MeV-GeV  $\gamma$ -ray flux. Interestingly, in their sample, three jets were located at higher redshifts ( $z > 3.5$ ). Out of these three sources, the IC/CMB interpretation of X-ray emission from J1510+5702 and J1421-0643 is ruled out considering the estimated  $\gamma$ -ray flux upper limits.

In our previous work (Rahman et al., 2022), we developed a model considering the advected electron distribution from the sites of particle acceleration. The composite emission from the accelerated and advected electron distribution is used to interpret the radio-optical-X-ray observations from the knots of large-scale AGN jets. Particularly, the synchrotron emission from accelerated electron distribution explains the X-ray emission, whereas the advected electron distribution explains the radio emission. In this work, we apply this model to the two high redshift sources J1510+5702 and J1421-0643 to explain their MSC jet emissions. Throughout this work, we consider a cosmology where  $H_0 = 71 \text{ km s}^{-1} \text{ Mpc}^{-1}$ ,  $\Omega_m = 0.27$  and  $\Omega_\Lambda = 0.73$ .

## 5.2 Source Selection

For this study, we have chosen the sources with MSC jets at high redshifts ( $z > 3.5$ ) and for which IC/CMB interpretation of the X-ray emission is ruled out by flux upper limit values deduced from *Fermi*/LAT  $\gamma$ -ray observations. We could identify two such sources, namely, J1510+5702 and J1421-0643 (Breiding et al., 2023).

### 5.2.1 J1510+5702 (GB 1508+5714)

The extended (kilo-parsec scale) X-ray emission from the high redshift ( $z=4.3$ ) quasar GB 1508+5714 was reported initially by Siemiginowska et al. (2003) and Yuan et al. (2003). Later, its radio

counterpart was discovered by Cheung (2004) using the archival VLA data. The X-ray emission feature is located at 3-4 arcsecs away from the quasar core and was initially interpreted as IC/CMB radiation.

For this study, we used the compiled archival data in radio, optical and X-ray (Breiding et al., 2023; Siemiginowska et al., 2003; Yuan et al., 2003; Cheung, 2004). Even though this source was not listed in the 3FGL catalog, it later appeared in the 4FGL catalog. This data was used to estimate the flux upper limits in the  $\gamma$ -rays, and thereby the IC/CMB model is ruled out for this high redshift source (Breiding et al., 2023). Interestingly, this is the highest red-shift source for which the *Fermi*  $\gamma$ -ray upper limit values are estimated so far.

## 5.2.2 J1421-0643 (PKS 1418-064)

The X-ray emission from the kilo-parsec scale jet of PKS 1418-064 ( $z = 3.69$ ) was first detected by the *Chandra* AO8 program (PI: Cheung) in 2007. X-ray emission from this jet was initially measured using the Bayesian multi-scale image reconstruction method (McKeough et al., 2016). Later, the observation was re-analyzed and a continuous jet was identified that extends up to 4.5 arcsecs (32 kpc projected length) (Worrall et al., 2020).

We use the MSC data of the jet from Breiding et al. (2023), which was compiled from Worrall et al. (2020) and the VLA L/C-band images for the radio flux densities. Initially, the IC/CMB model was proposed for the X-ray emission from this source (McKeough et al., 2016; Worrall et al., 2020); however, the *Fermi* flux upper limit values estimated questioned this interpretation (Breiding et al., 2023).

## 5.3 Electron Acceleration and Advection Model

We consider a model where the electron distribution responsible for the broadband emission is composed of accelerated and advected electron distributions. The details of the model are described in the previous chapter (Rahman et al., 2022). It assumes the particle acceleration in the AGN knot to be confined within a spherical region of size  $R_0$  and populated with a broken power law electron distribution; possibly arising due to multiple acceleration mechanisms (Sahayanathan, 2008; Pope & Melrose, 1994). The accelerated electrons advect out and lose their energy through radiative and adiabatic expansion processes. The magnetic field in regions  $R < R_0$  and  $R > R_0$  are considered to be different and denoted as  $B_{in}$  and  $B_{out}$  respectively. The advected electron distribution is significantly different from the accelerated electron distribution and satisfies the requirement of the second electron population.

## 5.4 Results and Discussion

We applied the electron acceleration and advection model described above to reproduce the radio–optical–X-ray fluxes from the kilo-parsec scale jets of J1510+5702 and J1421-0643. The synchrotron emission from the broken power-law electron distribution confined within region  $R < R_0$  successfully interprets the X-ray flux. Whereas, the advected electron distribution from the region  $R > R_0$  dominates the low energy electron distribution and the synchrotron emission from this population reproduces the observed radio fluxes. In Fig.5.1, we show the observed radio–optical–X-ray fluxes from the jets along with the model. The blue short-dash line is the synchrotron emission from the accelerated electron distribution while the red short-dash line indicates synchrotron emission from the advected electron population. The combination of the emission spectra from both these regions will result in a concave upward nature. The total synchrotron emission (accelerated and advected electron population) is shown as a green solid line.

To estimate the IC/CMB spectral component using the approximate analytical solution for a monochromatic external photon field, we used the IC/CMB emissivity at a frequency  $\nu$  given by (Dermer et al., 1992; Sahayanathan et al., 2018),

$$j_{ec}(\nu) \approx \frac{c\sigma_T U_*}{8\pi\nu_*} \sqrt{\frac{\Gamma\nu(1+\mu)}{\nu_*}} N_{\text{tot}} \left[ \sqrt{\frac{\nu}{\Gamma\nu_*(1+\mu)}} \right] \quad (5.4.1)$$

Here,  $U_*$  and  $\nu_*$  are the energy density and frequency of the external photon field and  $\mu$  is the cosine of the jet viewing angle measured in the proper frame of the AGN. For the chosen set of parameters that reproduce the radio–optical–X-ray fluxes of the jet, the IC/CMB spectrum falls below the *Fermi* upper limits. In Fig.5.1, the long-dash blue and red lines correspond to the IC/CMB emission from the accelerated and advected electron distributions respectively. The black long-dash line represents the total emission curve (IC/CMB and synchrotron emission from both advected and accelerated electrons). The synchrotron self Compton (SSC) emission corresponding to the accelerated particle distribution is shown using the magenta dashed lines. The flux associated with SSC is much lower compared to the other radiations and its contribution will be further reduced in the advection region.

The model parameters used to reproduce the multi-spectral component emission are obtained through eye fit and are given in Table.5.1. The parameter  $R_{\text{size}}$  corresponds to the typical size of the knot and depends upon the observed photon frequency. This parameter can be constrained from the observed radio contours of the source. The magnetic field in the acceleration ( $B_{\text{in}}$ ) and advection ( $B_{\text{out}}$ ) regions are chosen to be different with a relatively larger field in the acceleration region. If we assume the acceleration region encompasses shock, then the shock will energise the particle distribution as well as the magnetic field in the region (Beresnyak et al., 2009; Hu et al., 2022). Reproduction of the radio fluxes demands the advection velocity to be mildly relativistic of the order of  $\sim 10^{-2}c$ . The parameters  $\gamma_b$ ,  $p$  and  $q$  represent the break energy, lower and high energy indices associated with the broken power law particle distribution and are constrained by reproducing the

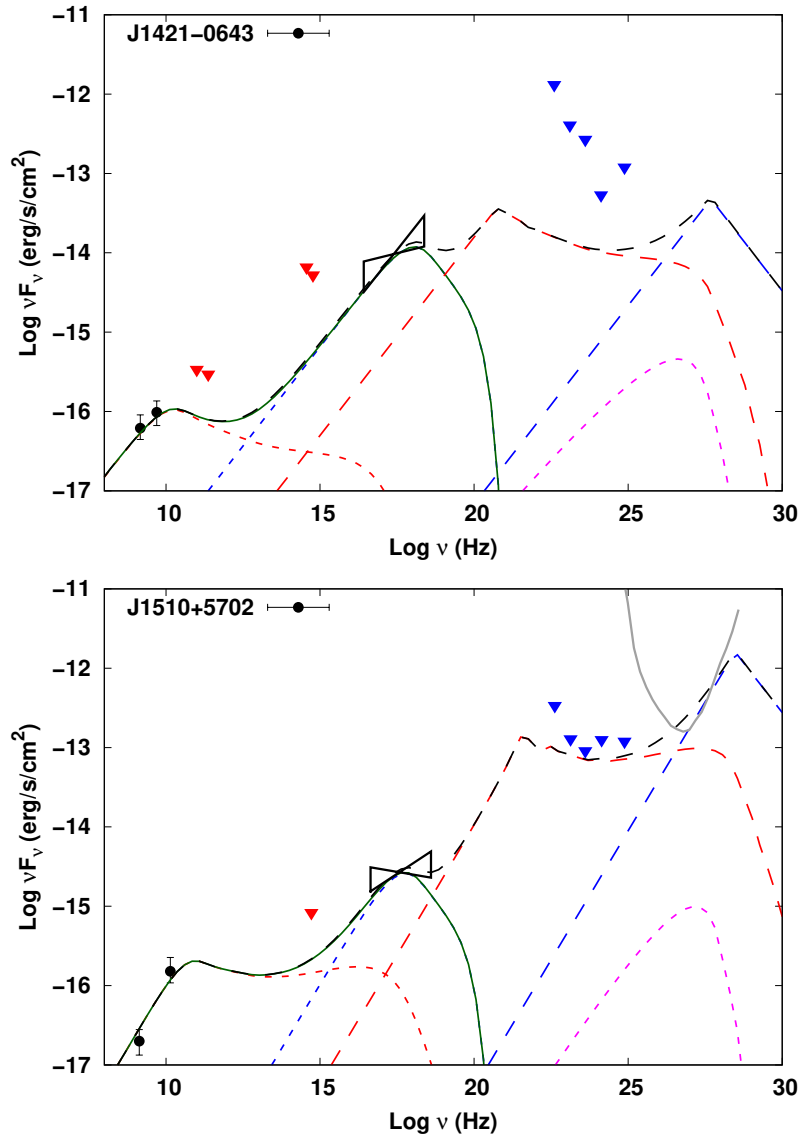


**Figure 5.1:** Observed broadband SEDs in radio (black solid circles) and X-ray (butterfly diagrams) of the jets along with the model curves. The red inverted triangles correspond to upper limit values estimated in the optical waveband. The blue and red short-dash line represents the synchrotron emission from accelerated and advected electron populations respectively. The green solid line is the total synchrotron emission (accelerated+advected electron distribution). The blue and red long-dashed line corresponds to IC/CMB emission corresponding to the accelerated and advected electron distribution respectively. The *Fermi* upper limits are denoted by blue inverted triangles. The black long-dash line represents the sum of synchrotron and IC/CMB emissions. The short-dashed magenta line represents the SSC emission associated with the accelerated particle distribution. The grey line shows the differential sensitivities of the CTAO-Northern array ( 50 hr-Omega configuration).

observed fluxes. Moreover, we have assumed  $\gamma_{\min} = 10$  and the  $\gamma_{\max}$  ( $\gtrsim 10^8$ ) is chosen to a large value to extend the spectra to X-ray energies. The viewing angle of the jet is chosen to be  $\theta = 15^\circ$ .

The Lorentz factor of the electron responsible for the X-ray emission is  $\gamma \sim 10^8$ . The Larmor radius of the electrons with such energy in a magnetic field of the order  $10^{-5}$  G is ( $r_L(\gamma) \sim \frac{\gamma mc^2}{eB}$ )  $\sim 10^{-3}$  pc. This is much less than the size of the acceleration region considered in our model. Hence, with the presence of an efficient accelerator, electrons with such energies can be confined within the acceleration region (Hillas criterion; Hillas (1984)). Further, the acceleration time scale corresponding to an electron of Lorentz factor  $10^8$  will be of the order of  $t_{acc}(\gamma) \sim \frac{r_L(\gamma)}{c} \sim 10^5$  s (Inoue & Takahara, 1996) and the synchrotron radiative loss time-scale is of the order of  $10^9$  s. Hence, acceleration of electrons to such high energies is possible under the scenario considered here. The kinetic power of the jet can be estimated as  $P_{jet} = \pi R^2 \Gamma^2 \beta c (U_B + U_e + U_p)$  where  $U_B$ ,  $U_e$  and  $U_p$  are the co-moving energy densities of the magnetic field, electrons and protons respectively (Celotti et al., 1997; Celotti & Ghisellini, 2008). Under the leptonic emission scenario, the protons are assumed to be cold and do not participate in the radiative processes. Approximate jet power is obtained by assuming the number of cold protons to be equal to the non-thermal electrons. For the chosen set of parameters, we find the jet power to be  $10^{40}$  erg/s.

The X-ray to radio luminosity ratio for blazars is found to increase with redshift (Toda et al., 2020; Shen et al., 2020; Ajello et al., 2009; Hopkins et al., 2007). The contribution of IC/CMB emission towards this increase were of particular interest (Zhu et al., 2019; Hodges-Klucck et al., 2021). Wu et al. (2013) did a systematic study on 17 highly radio-loud quasars (HRLQs: radio-loud quasars that fall in the top 5 % in terms of radio loudness) at  $z > 4$  and found X-ray emission enhancement by a factor of  $\sim 3$  when compared to HRLQs at lower redshifts. HRLQs at redshifts 3 – 4 also showed a similar trend supporting their argument. To explain this, a fractional IC/CMB interpretation was proposed. According to this, the CMB interaction contributes a small fraction ( $\sim 3\%$ ) at low redshifts ( $z \sim 1$ ) and becomes dominant with an increase in redshift. Later, Ighina et al. (2021b) tested this interpretation on a statistically complete sample of blazars covering a large redshift range from  $z = 0.5$  to  $z = 5.5$ . Their study satisfactorily explains the observed redshift-dependent trend of the X-ray-to-radio luminosity ratios.

The quasar J1510+5702 has an X-ray to radio luminosity ratio  $\rho_{xr} > 100$  (Cheung, 2004) which is proportional to the ratio of the energy density of target photons (CMB) to the magnetic field energy density;

$$\rho_{xr} \propto \frac{U_{CMB}}{U_B} \quad (5.4.2)$$

$$\propto \frac{(1+z)^4}{(\delta/B)^2} \quad (5.4.3)$$

The large value of  $\rho_{xr}$  is consistent with the  $(1+z)^4$  amplification based on the IC/CMB interpretation (Schwartz, 2002). Additionally, the X-ray photon index of this source is relatively harder ( $< 1.6$ ) (McKeough et al., 2016); suggesting the dominance of jet emission in X-ray. Even though these



two studies confirm the X-ray emission originating from the kpc scales dominated by the IC/CMB process; the recently estimated *Fermi*  $\gamma$ -ray flux upper limits rule out this interpretation (Breiding et al., 2023). The single population IC/CMB model also predicts the radio spectral index to match with the X-ray spectral index, since the same electron distribution is responsible for the emission at these energy bands. However, the observed X-ray spectral index of the jet in J1510+5702 is harder than the radio, which disfavors this model. In the model assumed in this work, the electron distribution responsible for the dominant radio and X-ray emission are different and hence, can support different spectral indices.

In the model presented here to explain the second electron population, we have only considered the advection of electrons and neglected the diffusion. Incorporating diffusion will include the second-order term in the governing equation (Rahman et al., 2022) in the form

$$\frac{\partial}{\partial r} \left[ K \frac{\partial n}{\partial r} \right]$$

where  $K$  is the spatial diffusion coefficient. An order of magnitude estimation for the diffusion timescale can then be obtained as

$$t_{\text{diff}} \sim \frac{R^2}{K} \quad (5.4.4)$$

Approximating  $K \sim r_g c$  where,  $r_g$  is the gyro-radius for an electron with Lorentz factor  $10^5$  (equivalent to that of the electron responsible for synchrotron radio emission at frequency  $10^{11}$  Hz), and for magnetic field  $\sim 10^{-5}$  G, we obtain  $K \sim 10^{23} \text{cm}^2/\text{s}$ . Since the observed knot size is of the order kpc, we find the  $t_{\text{diff}} \sim 10^{18}$  s. On the other hand, the advection timescale can be expressed as

$$t_{\text{ad}} \sim \frac{R}{v_{\text{ad}}} \quad (5.4.5)$$

and for  $v_a \approx 0.01c$  we obtain  $t_{\text{ad}} \sim 10^{12}$  s. Clearly, the rate of advection should be much faster than the diffusion in order to explain the kpc-sized knots. Hence, the model considered in the present work is consistent with the observed features of the kpc scale jets of AGN.

The shear acceleration process on the AGN jet can also produce a second population that is capable of explaining the radio-optical-X-ray emission from the large-scale jets (Tavecchio, 2021; Rieger, 2019). Such a model was adopted to interpret the X-ray emission from many jets, including PSO J0309+27 (Ighina et al., 2022), the farthest X-ray jet discovered so far. The IC/CMB emission by these two populations also satisfies the *Fermi*  $\gamma$ -ray upper limit conditions. According to this model, at higher redshifts, the IC/CMB dominates since the IC/CMB cooling time scale is shorter compared to the shear acceleration time scales of electrons. This results in the quenching of synchrotron emission from second high-energy population produced via shear acceleration. Therefore, in terms of this model, the second electron population dominate the X-ray emission of low- $z$  jets, while IC/CMB emission contribute majorly at high redshift (Ighina et al., 2022).

Lately, Meyer et al. (2023) reported the X-ray variability in large-scale AGN jets adopting a

Source	$R_0$ (kpc)	$R_{\text{size}}$ (kpc)	$B_{\text{in}}(10^{-5}G)$	$\frac{B_{\text{in}}}{B_{\text{out}}}$	$\gamma_b(10^7)$	$v_{\text{ad}}(c)$	$p$	$q$	$\Gamma$	$\zeta$
J1510+5702	0.17	5.0	0.8	1.14	28.0	0.01	1.7	4.0	1.02	7.0
J1421-0643	0.10	5.0	12.0	10.0	9.0	0.01	2.0	4.0	1.10	7.0

**Table 5.1:**  $R_0$  is the size of the inner region;  $R_{\text{size}}$  is the size of the knot;  $B_{\text{in}}$  and  $B_{\text{out}}$  represent the magnetic field strength at  $R < R_0$  and  $R > R_0$  respectively. The quantities  $\gamma_b$ ,  $v_{\text{ad}}$ ,  $p$ ,  $q$ ,  $\Gamma$  and  $\zeta$  represent the break energy, advection velocity (fluid velocity), low and high indices of broken power law distribution of particles, bulk Lorentz factor and the constant defining escape radius respectively.

statistical analysis of 53 jets. Under the IC/CMB interpretation of X-ray emission, this variability is not expected. However, synchrotron emission by a second population of electrons with energies up to TeV is compatible with these observations. Moreover, the electron acceleration and advection model (Rahman et al., 2022) considers a smaller spherical volume (with a radius of a few hundred parsecs) where particles accelerate up to multi-TeV energies and emit via synchrotron mechanism to produce X-rays. These highly energetic electrons confined to a small emitting volume can interpret the variability time scales of months to years (Meyer et al., 2023).

Another peculiar observation of AGN knots is the positional offsets, which indicate that the centroid of the knot measured in different wavebands are not co-spatial (Marchenko et al., 2017; Reddy et al., 2023). The IC/CMB model assumes low energy electrons (lower than the one responsible for radio flux) in the jet up-scattering the CMB photons to X-ray energies. Hence, X-ray emission is expected to persist downstream of the radio knot due to the longer lifetime of these electrons (Harris & Krawczynski, 2007). However, the X-ray peaks well before the radio emission in many of the resolved MSC jets (Siemiginowska et al., 2007; Kataoka et al., 2008; Clautice et al., 2016; Marchenko et al., 2017). A physically separated two population model as described in this paper has the potential to address this signature observed in knots by assuming an asymmetric advection. Nevertheless, the lack of X-ray counts in the jets is another difficulty in measuring the offset. Dedicated *Chandra* observations in the future will contribute to a better understanding of the jet structure, morphological features and associated emission mechanisms.

# Chapter 6

## Probing IC/CMB Interpretation for the X-ray Knots of AGN through VHE Observations

---

### 6.1 Introduction

The X-ray flux from the knots, when interpreted as an IC/CMB process, the Compton spectrum peaks at GeV energy with significant radiation at gamma-ray energies. Hence, *Fermi* observations play a crucial role in validating this emission scenario (Georganopoulos et al., 2006). However, even after a decade of observations, *Fermi* failed to detect any appreciable  $\gamma$ -ray photons from some sources and the upper limits drawn fall significantly below the flux predicted by the IC/CMB emission model (Meyer & Georganopoulos, 2014; Meyer et al., 2015). Particularly, the  $\gamma$ -ray studies of the *Chandra* detected sources namely, 3C 273(CDQ), PKS 0637-752(CDQ), PKS 1136-135(LDQ), PKS 1229-021(CDQ), PKS 1354+195(CDQ) and PKS 2209+080(CDQ) (Meyer & Georganopoulos, 2014; Meyer et al., 2015; Breiding et al., 2017) have strongly ruled out the IC/CMB interpretation but favour a scenario where synchrotron emission from a second population of relativistic electrons is responsible for the observed X-ray emission (Liu et al., 2015; Tavecchio, 2021; Harris & Krawczynski, 2002; Atoyan & Dermer, 2004; Kataoka & Stawarz, 2005). In Chapter 4, we show that the advection of electrons from the regions of particle acceleration can naturally produce two distinct populations which can successfully explain the X-ray emission from the kpc scale knots of 3C 273 (Rahman et al., 2022).

Though recent observational evidence, including  $\gamma$ -ray upper limits, disfavour the IC/CMB interpretation of X-ray emission (Breiding, 2018), it is still a preferred model for those sources which are not yet ruled out by *Fermi* observations (Kharb et al., 2012; Godfrey et al., 2012; Stanley et al., 2015). Zhang et al. (2010) present the analysis of 22 hotspots and 45 knots to conclude that the IC/CMB model can explain the X-ray emission from the majority of the jet components. This study was then extended to a larger number of jet components and the jet power is estimated under IC/CMB and SSC emission scenarios for the observed X-ray fluxes (Zhang et al., 2018). The jet power estimated considering IC/CMB strongly correlates with the jet kinetic power obtained through radio studies. Whereas, the SSC interpretation did not exhibit any significant correlation. These findings further supported the IC/CMB as a promising mechanism to explain the high-energy emission from the knots.

Lucchini et al. (2017) revisited some aspects of the IC/CMB model to show the role of electron

cooling in shaping the spectrum. They suggest, the overproduction of gamma-rays can be avoided by suppressing the high-energy end of the emitting particle population. They applied this model for the case of PKS 0637-752 and demonstrated that IC/CMB can still be a valid explanation for the high energy production from the large-scale knots of AGN. In this context, it will be useful to explore the alternative techniques which can supplement the Fermi studies to test the plausibility of the IC/CMB interpretation for the high energy emission.

Modelling the X-ray emission from kilo-parsec scale jets using IC/CMB model also suggests this spectrum can extend up to very high energies (VHE)(Meyer et al., 2021, 2019; Georganopoulos et al., 2006). Hence, future VHE observation of these sources can provide further constraints in addition to the ones drawn through *Fermi* observations. The operational ground-based VHE telescopes employing imaging atmospheric Cherenkov techniques have already detected six radio galaxies with misaligned jets at GeV/TeV energies (Aleksić et al., 2012; Aharonian et al., 2009, 2006; Holder, 2011; Dyrda et al., 2015; Aleksić et al., 2010; Rulten, 2022). Among these sources, four belong to the FRI class of radio galaxies (M 87, Cen A, NGC 1275, and 3C 264) while the other two (PKS 0625-35 and IC 310) show the properties of radio galaxy and blazar as well (Wakely & Horan, 2008). If IC/CMB is a viable emission process for the X-ray knots, then this suggests many misaligned jets may be a potential TeV candidate. Alternatively, VHE studies can also be a tool to validate this emission scenario in tandem with the *Fermi* observations.

Considerable advancement in the stereoscopic imaging atmospheric Cherenkov techniques have led to new generation VHE telescopes whose sensitivity is appreciable even at a few tens of GeV. Particularly, with the inputs from the upcoming Cherenkov Telescope Array (CTA), it may be possible to verify the IC/CMB interpretation of the X-ray knots which were not been ruled out through *Fermi* observations. In the present work, we selected all the kilo-parsec scale X-ray jets for which the IC/CMB emission process is favoured. We model the radio and optical fluxes from these sources as synchrotron emission from a broken power-law electron distribution. The source parameters are constrained considering the equipartition between the magnetic field and the particle energy density. The IC/CMB spectrum is then extrapolated to VHE energies and compared with the CTA sensitivity curves. The chapter is organised as follows: In section 2, we describe the source selection and in section 3, the spectral models used in the paper. In section 4 we present our results and discussion. Throughout this work we consider a cosmology where  $H_0 = 71 \text{ km s}^{-1} \text{ Mpc}^{-1}$ ,  $\Omega_m = 0.27$  and  $\Omega_\Lambda = 0.73$ .

## 6.2 Source Selection

*Chandra* during its two decades of operation was able to resolve nearly 150 X-ray extended features from AGN (Xjet:<https://hea-www.harvard.edu/XJET/>). Many of these extended jet features showed bright knots and hotspots which are coincident (near-coincident) with radio/optical maxima. Spectral energy distribution (SED) of these knots (and unresolved jet features) in radio, optical and X-ray have been already analysed and reported in earlier works (Schwartz et al., 2006; Siemiginowska et al.,

Source	Type	Knot	$z^a$	$\text{Log}(F_{\text{obs}}^r)^b$	$\text{Log}(F_{\text{obs}}^o)^c$	$\text{Log}(F_{\text{obs}}^x)^d$	Reference
3C 15	FRI	K C	0.073	-24.63	-28.85	-31.87 <sup>+0.119</sup> <sub>-0.108</sub>	Dulwich et al. (2007)
3C 17	hybrid	S 3.7	0.22	-24.51	-28.66	-32.19 <sup>+0.256</sup> <sub>-0.168</sub>	Massaro et al. (2009)
3C 17	hybrid	S 11.3	0.22	-24.10 <sup>+0.04</sup> <sub>-0.04</sub>	-29.64 <sup>+0.07</sup> <sub>-0.07</sub>	-32.27 <sup>+0.15</sup> <sub>-0.15</sub>	Massaro et al. (2009)
3C 111	FR II	K 22	0.049	-25.42 <sup>+0.05</sup> <sub>-0.06</sub>	-29.38 <sup>+0.19</sup> <sub>-0.18</sub>	-32.40 <sup>+0.12</sup> <sub>-0.12</sub>	Clautice et al. (2016)
3C 111	FR II	K 30	0.049	-24.86	-28.04	-31.13	Clautice et al. (2016)
3C 111	FR II	K 61	0.049	-24.43	-28.78 <sup>+0.12</sup> <sub>-0.11</sub>	-31.38	Clautice et al. (2016)
3C 120	FRI	K 4	0.033	-24.45	-28.73	-31.52 <sup>+0.06</sup> <sub>-0.06</sub>	Harris et al. (2004)
3C 120	FRI	S 2	0.033	-24.88 <sup>+0.05</sup> <sub>-0.05</sub>	-28.62 <sup>+0.06</sup> <sub>-0.06</sub>	-32.54 <sup>+0.17</sup> <sub>-0.17</sub>	Harris et al. (2004)
PKS 1354+195	CDQ	S 4.0	0.720	-24.96	-30.07 <sup>+0.09</sup> <sub>-0.09</sub>	-32.27 <sup>+0.06</sup> <sub>-0.06</sub>	Harris et al. (2017)
PKS 1354+195	CDQ	S 5.3	0.720	-25.54 <sup>+0.04</sup> <sub>-0.04</sub>	-30.23 <sup>+0.09</sup> <sub>-0.09</sub>	-32.78 <sup>+0.11</sup> <sub>-0.11</sub>	Harris et al. (2017)
3C 346	FRI	K C	0.161	-24.16	-28.40 <sup>+0.13</sup> <sub>-0.13</sub>	-31.81 <sup>+0.05</sup> <sub>-0.06</sub>	Worrall & Birkinshaw (2005)
3C 454.3	CDQ	K A	0.859	-24.39	-29.92 <sup>+0.09</sup> <sub>-0.10</sub>	-31.24 <sup>+0.08</sup> <sub>-0.11</sub>	Tavecchio et al. (2007)
3C 454.3	CDQ	K B	0.859	-23.71 <sup>+0.04</sup> <sub>-0.04</sub>	-29.31 <sup>+0.03</sup> <sub>-0.03</sub>	-31.25 <sup>+0.11</sup> <sub>-0.10</sub>	Tavecchio et al. (2007)
PKS 2101-490	CDQ	K 6	1.040	-25.12 <sup>+0.02</sup> <sub>-0.02</sub>	-29.89	-32. <sup>+0.11</sup> <sub>-0.11</sub>	Godfrey et al. (2012)
PKS B0106+013	CDQ	K 1	2.11	-24.86	-30.50	-33.08	Kharb et al. (2012)
PKS B0106+013	CDQ	K 2	2.11	-24.62	-30.41	-33.37	Kharb et al. (2012)
PKS B0106+013	CDQ	K 3	2.11	-23.74	-30.62	-33.53	Kharb et al. (2012)
PKS 1045-188	CDQ	K C	0.590	-24.62 <sup>+0.09</sup> <sub>-0.09</sub>	-30.09 <sup>+0.05</sup> <sub>-0.05</sub>	-32.11	Stanley et al. (2015)

**Table 6.1:** List of AGNs with Jet Knots/components included in our source list. Notes:  $^a z$ , redshift;  $^b$  (col V),  $^c$  (col VI),  $^d$  (col VII) are the average observed fluxes in radio, optical and X-ray energies respectively. The energy range over which these fluxes are averaged is mentioned in references (col VIII).

2007; Wilson et al., 2001; Chartas et al., 2000). Due to less number of counts, spectral resolution at these energies cannot be achieved and the fluxes were reported only for one or few energy bins (Massaro et al., 2011, 2018; Stuardi et al., 2018). However, convoluting the X-ray instrumental response with a power-law source spectrum, constraints on the spectral index can be obtained and this can be helpful in identifying the emission process.

Among the sample of extended X-ray jets collected from the literature, we selected 18 X-ray knots/components with radio-optical-X-ray observations and a harder X-ray spectrum (spectral index less than 2 or the X-ray flux value larger than high-energy extension of the radio-to-optical synchrotron spectrum). The X-ray emission from these knots was interpreted as IC/CMB. Additionally, for these sources, the IC/CMB model was not ruled out by *Fermi* studies until 2023. In Table 6.1 we provide the list of complete sources and knots.

### 6.3 Emission Models

The radio/optical/X-ray knot buried in the AGN jet is considered to be a spherical region of size  $R_{\text{knot}}$  governed by its radio contour. We assume this region is uniformly populated with a broken power-law electron distribution of the form given by

$$N(\gamma)d\gamma = \begin{cases} K\gamma^{-p}d\gamma & \gamma_{\min} < \gamma < \gamma_b \\ K\gamma_b^{q-p}\gamma^{-q}d\gamma & \gamma_b < \gamma < \gamma_{\max} \end{cases} \quad (6.3.1)$$

where  $K$  is the normalisation,  $\gamma$  is the Lorentz factor of the electron and  $\gamma_b$  is the radiative cooling break. The electrons lose their energy through synchrotron and inverse Compton radiative processes. If we consider  $P_{\text{rad}}(\gamma, \nu)$  as the single particle emissivity due to these radiative processes, then the total emissivity from the knot can be obtained as (Rybicki & Lightman, 1986)

$$J_{\text{rad}}(\nu) = \frac{1}{4\pi} \int_{\gamma_{\min}}^{\gamma_{\max}} P_{\text{rad}}(\gamma, \nu) N(\gamma) d\gamma \quad (6.3.2)$$

Here,  $P_{\text{rad}}$  additionally depend on the magnetic field in the case of synchrotron (rad  $\rightarrow$  syn) while in the case of the inverse Compton process, it depends on the target photon energy and distribution (rad  $\rightarrow$  ic).

We assume a tangled magnetic field configuration which is in equipartition with the electron distribution (condition that indicates total energy of the system is minimum (Burbidge, 1959));

$$\frac{B^2}{8\pi} = m_e c^2 \int_{\gamma_{\min}}^{\gamma_{\max}} N(\gamma) \gamma d\gamma \quad (6.3.3)$$

Under delta function approximation for single particle emissivity, an approximate emissivity for synchrotron emission can be obtained as (Dermer & Menon, 2009; Sahayanathan & Godambe,

2012)

$$J_{\text{syn}}(\nu) \approx \frac{c\sigma_T B^2}{48\pi^2} \nu_L^{-\frac{3}{2}} N \left( \sqrt{\frac{\nu}{\nu_L}} \right) \nu^{\frac{1}{2}} \quad (6.3.4)$$

Since the X-ray emission is interpreted as an IC/CMB process, we can arrive at an analytical form of the IC emissivity by considering the CMB distribution as a monochromatic photon field and a delta function approximation for the  $P_{\text{ic}}$  (Dermer & Menon, 2009; Sahayanathan et al., 2018)

$$J_{\text{ic}}(\nu) \approx \frac{c\sigma_T U_*}{8\pi\nu_*} \sqrt{\frac{\Gamma\nu(1+\mu)}{\nu_*}} N \left[ \sqrt{\frac{\nu}{\Gamma\nu_*(1+\mu)}} \right] \quad (6.3.5)$$

Here,  $\nu_*$  and  $U_*$  are the frequency and energy density of the external photon field,  $\Gamma$  is the bulk Lorentz factor of the jet and  $\mu$  is the cosine of the jet viewing angle measured in the proper frame of the AGN. In the observer's frame, the total flux due to these radiative processes can be obtained after considering the relativistic and cosmological effects (Begelman et al., 1984; Dermer, 1995)

$$F_{\text{obs}}(\nu_{\text{obs}}) = \frac{\delta_D^3 (1+z)}{d_L^2} V J_{\text{syn/ic}} \left( \frac{1+z}{\delta_D} \nu_{\text{obs}} \right) \quad (6.3.6)$$

Here,  $V = 4/3 \pi R_{\text{knot}}^3$  is the volume of the emission region,  $z$  is the source redshift,  $d_L$  is the luminosity distance and  $\delta_D = 1/[\Gamma(1 - \beta\mu)]$  is the jet Doppler factor.

### 6.3.1 Source Parameters

The observed spectrum due to the IC/CMB model is mainly governed by 8 source parameters with 4 of them  $K$ ,  $p$ ,  $q$  and  $\gamma_b$  governing the electron distribution, and the rest are the size of the emission region  $R_{\text{knot}}$ , magnetic field  $B$ , jet Lorentz factor  $\Gamma$  and the jet viewing angle  $\theta$ . Besides these, the parameters  $\gamma_{\text{min}}$  and  $\gamma_{\text{max}}$  do not govern the source fluxes but rather decide the low and high energy end of the radiation spectrum (see section 6.4). The limited amount of information available in radio, optical and X-ray bands do not let us to draw stringent constraints on these parameters. However, modest constraints can be imposed by assuming equipartition between the magnetic field and particle energy densities (equation 6.3.3) and the emission region size of kilo-parsec scale order which is consistent with the typical radio contours of the knots.

The synchrotron flux at radio/optical in combination with equation 6.3.3 can effectively constrain  $B$  and  $K$  while the spectral indices can be used to identify  $p$  and  $q$ . The synchrotron spectral peak frequency can be expressed in terms of the source parameters as

$$\nu_{\text{p,syn}} = \frac{\delta_D}{1+z} \gamma_b^2 \frac{eB}{2\pi m_e c} \quad (6.3.7)$$

For a given  $\delta_D$ ,  $\gamma_b$  can be estimated from the approximate peak frequency. With these constraints, we will be left with the parameters  $\Gamma$  and  $\theta$  which can be fine-tuned to reproduce the X-ray flux due to IC/CMB process. The approximate analytical expressions for the synchrotron and IC/CMB fluxes

are used only to estimate the source parameters. The final model spectrum is produced numerically using the exact functional form of the single particle emissivities and compared with the observed fluxes.

An upper limit on the angle of the jet to the line of sight ( $\theta$ ) can be drawn from the apparent superluminal motion obtained through VLBI observations. Breiding et al. (2023) estimate the upper limits on  $\theta$  for 3C 111, 3C 120, PKS 1045-188 and 3C 454.3 to be  $13.5^\circ$ ,  $12.6^\circ$ ,  $10.5^\circ$  and  $4.5^\circ$  respectively. An upper limit of  $13^\circ$  is estimated for the jet inclination angle of PKS B0106+013 (Kharb et al., 2012). Harris et al. (2017) using the apparent superluminal proper motions of pc-scale jet estimate that the kpc-scale jet of PKS 1354+195 is aligned at  $\theta \leq 12^\circ$ . Dulwich et al. (2009) calculate the viewing angle of 3C 346 to be  $\theta = 14 \pm 8^\circ$ . The apparent velocity measurements of 3C 15 is not available. However, Leahy et al. (1997) found its jet/counter-jet flux density ratio and puts a constraint of  $\theta \approx 45^\circ - 50^\circ$  for  $\beta \geq 0.9$ . But, to explain the X-ray emission through the IC/CMB model, the jet inclination should be less than the angle constraint drawn from the jet/counter-jet ratio. Therefore in this work,  $\theta$  is chosen such that the model curve fits with the observations. The apparent velocity or jet/counter-jet measurements for sources 3C 17 and PKS 2101-490 are not available. Therefore, the viewing angle for these sources is chosen such that the IC/CMB model curve can fit with the radio-optical-X-ray observations of the knots. The sizes of individual knots are constrained using radio data and the value is listed in Table 5.1.

## 6.4 Results and Discussion

We apply the IC/CMB model to reproduce the X-ray flux of 18 knots/jet components from the sources which are not ruled out by initial *Fermi* observations (Table 6.1). As mentioned earlier, the initial guess parameters are derived from approximate analytical expressions for the emissivity functions and are then fine-tuned to reproduce the radio-optical-X-ray fluxes using the exact numerical solutions. The best-fit model parameters (chi-by-eye) for these knots are given in Table 6.2 with their corresponding SEDs shown in Figures 6.1 and 6.2.

The parameters  $\gamma_{min}$  and  $\gamma_{max}$  cannot be constrained from the available information and we have fixed these quantities at 50 and  $10^3 \times \gamma_b$  ( $\sim 10^8 - 10^9$ ) respectively for all the SEDs. The Compton up-scattered photon energy scales as  $\gamma^2$  and hence this choice of  $\gamma_{max}$  assures the Compton spectral component extends up to the sixth order from the spectral peak. The gyro-radius of the electron corresponding to  $\gamma_{max}$  is  $\sim 10^{-2} - 10^{-1}$  pc, which is much less than the assumed size of the knot. Therefore, this ensures that such high-energy electrons can still be confined within the emission region. The equipartition magnetic field depends on  $\gamma_{min}$ , since the particle energy density is largely decided by the electrons at this energy. However, we noted that moderate variation in  $\gamma_{min}$  (within the same order) does not alter our conclusions significantly.

To predict the VHE flux from these knots/jets, we extended the IC/CMB model spectrum to VHE. The VHE photons produced from distant sources undergo significant attenuation through the pair production process with the EBL. To account for this, we have considered the EBL spectrum



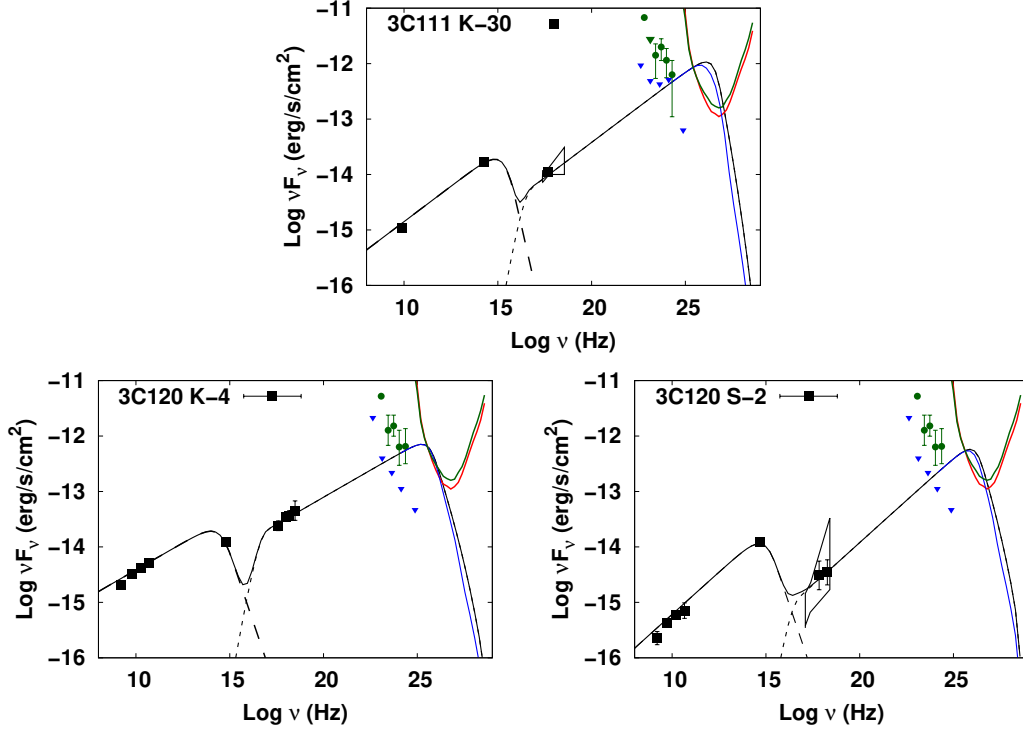


**Figure 6.1:** Large-scale knots falling within the detection threshold of CTAO. The dashed line and densely dashed line are the synchrotron and IC/CMB model curves respectively. The black solid line represents the synchrotron+IC/CMB curve. Solid squares are the multi-wavelength observational data of the knots. The red solid line and green solid line is the differential sensitivities of CTAO-Northern array Omega(50-hour) and Alpha configuration respectively. The blue solid line is the IC/CMB model curve corrected for EBL absorption. Inverted triangles(green) and solid circles(green) are the *Fermi* upper limit values and the *Fermi* observations(Xue et al., 2017). Inverted triangles(blue) are the updated *Fermi* upper limit values (Breiding et al., 2023). *Fermi*-LAT points(solid circles) correspond to the total observed emission, while the upper limits(inverted triangles) were derived specifically for the emission from the extended jet.

provided by Franceschini & Rodighiero (2017) and the attenuated VHE spectrum is compared with the 50-hour sensitivity curve of CTAO obtained from the CTAO webpage (<https://www.cta-observatory.org/science/cta-performance/>). In Fig 6.1 and 6.2, the blue solid line is the VHE spectrum after accounting for the EBL-induced attenuation. The red, green and magenta solid lines are the 50-hour CTAO differential sensitivities of Omega (Northern array), Alpha (Northern array) and Omega configuration (Southern array) respectively. The *Fermi* gamma-ray upper limits/detections are shown as green inverted triangles/solid circles. Out of all the knots studied, we find the knots of 3C 111 (K 30), 3C 120 (K 4) and a section of 3C 120 jet (S 2) fall within the detection threshold of CTAO. The SED corresponding to these knots/jets is shown in Fig. 6.1 along with the CTAO sensitivity curve. The knots whose VHE model flux fall below the CTAO sensitivity curve is shown in Fig. 6.2. Moreover, both 3C 120 and 3C 111 can be detected from the Northern site of the CTA at reasonable zenith angles.

Among the two sources predicted as a CTAO VHE candidate under the IC/CMB model, 3C 111

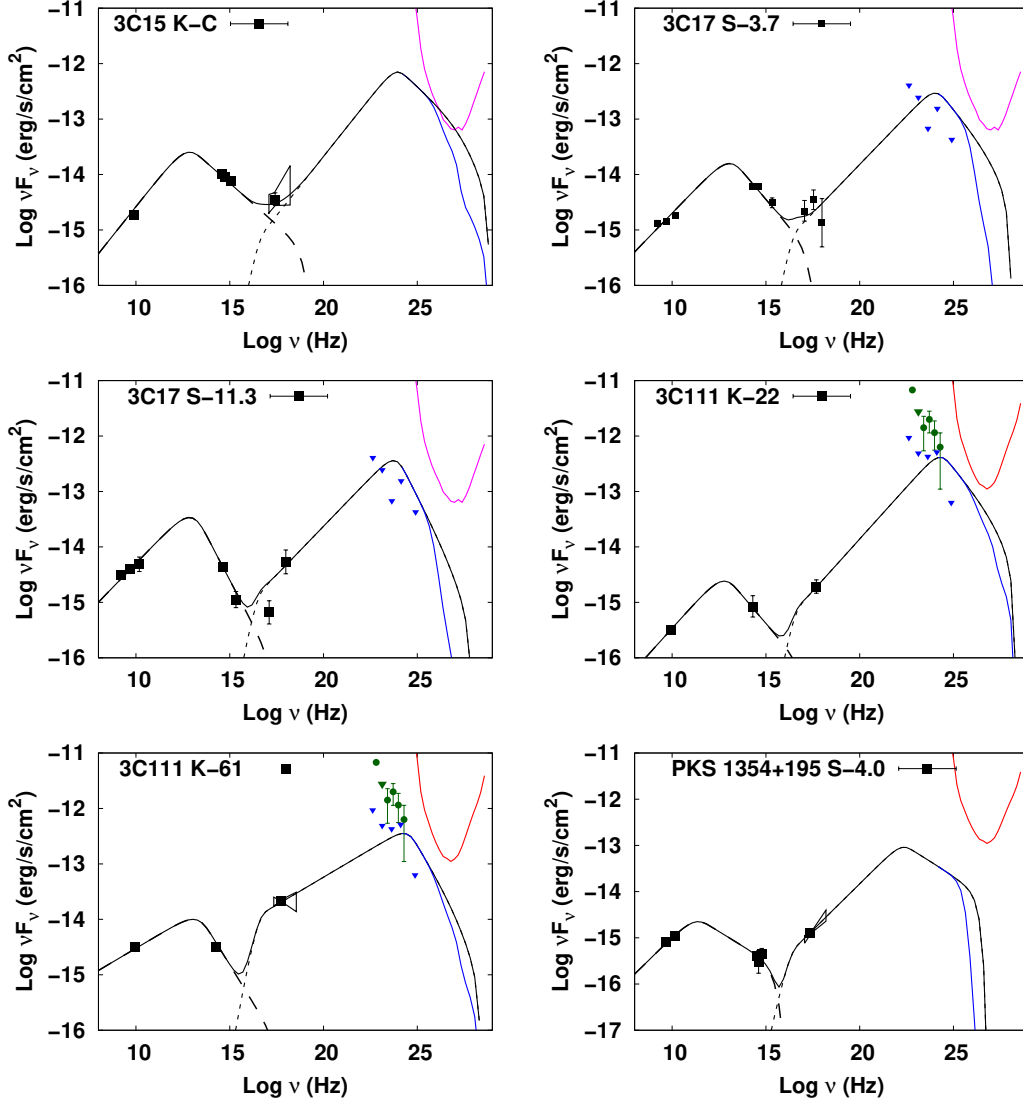


**Figure 6.2:** Large-scale knots that do not fall within the detection threshold of CTAO. Dashed line and densely-dashed line are the synchrotron and IC/CMB model curves respectively. The black solid line represents the synchrotron+IC/CMB curve. The dotted lines represent the SSC model curve. Solid squares are the multiwavelength observational data of the knots. The blue solid line is the IC/CMB model curve corrected for EBL absorption. The red solid line and the green solid line are the differential sensitivities of the CTAO-Northern array Omega(50-hour) and Alpha configuration respectively. The magenta solid curve corresponds to differential sensitivities of the CTAO-Southern array Omega configuration (50-hour). Inverted triangles (green) and solid circles (green) are the *Fermi* upper limit values and *Fermi* observations for 3C 111 and 3C 454.3 (Xue et al., 2017; Zhang et al., 2015). Blue inverted triangles/solid circles are the recent *Fermi* upper limit values/observations (Breiding et al., 2023). *Fermi*-LAT points (solid circles) correspond to the total observed emission, while the upper limits (inverted triangles) were derived specifically for the emission from the extended jet.

belongs to FR II morphology (Fanaroff & Riley, 1974) located at  $z=0.049$ . The radio observation suggests a 100 kilo-parsec long jet and *Chandra* was able to resolve nearly 10 knots with at least eight which are prominent in X-rays (Clautice et al., 2016). Among them, the knots K 22, K 30 and

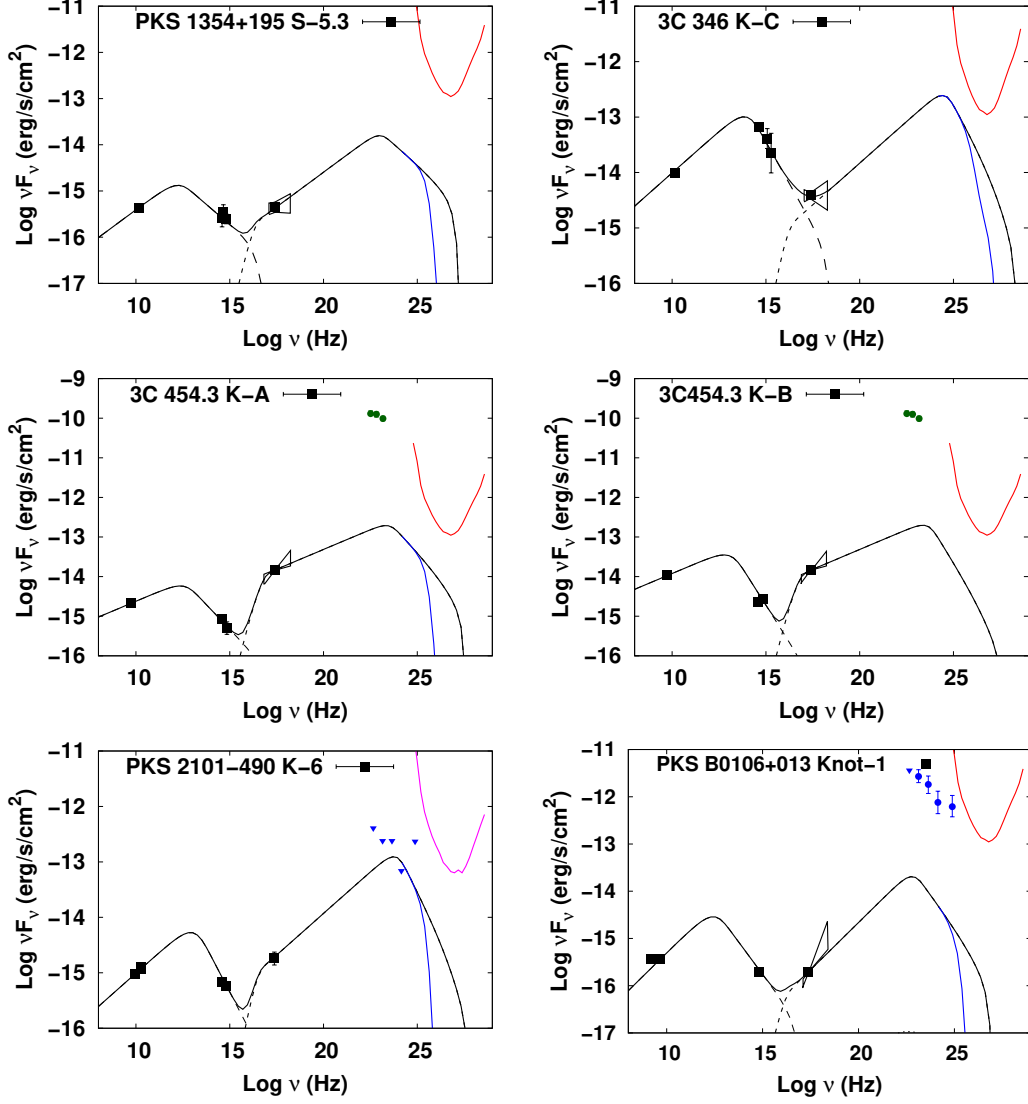


**Figure 6.3:** Fig 6.2 continued

K 61 indicate a hard X-ray spectrum suggesting an inverse Compton origin of the X-ray emission. Whereas, the knots K 9, K 14, K 38, K 45, K 51, K 97 and K 107 have steeper X-ray spectra supporting a synchrotron origin (Zhang et al., 2018). Hence, for the present work, we have considered only the three X-ray knots K 30, K 61 and K 22, with K 30 being the brightest among them. Modelling the X-ray emission as IC/CMB mechanism predicts significant VHE flux for the knot K 30 which can be examined by future CTAO observations. The predicted VHE flux of K 61 and K 22 fall below the CTAO sensitivity even though the X-ray flux of K 61 is comparable with K 30. We anticipate the reason for this being the steep X-ray spectrum of K 61 as compared to K 30.

Recently, Breiding et al. (2023) ruled out the IC/CMB interpretation of the X-ray emission for 3C 111 considering the knot K 61 through the updated *Fermi* upper limits (these upper limits are shown as blue inverted triangles in Fig. 1 and 2). However, the steep X-ray index of the knot K 61 is not consistent with the model spectrum and this can cause ambiguity (Breiding et al., 2023). On the other hand, the X-ray spectrum of K30 is hard and can provide better constraints. Comparing

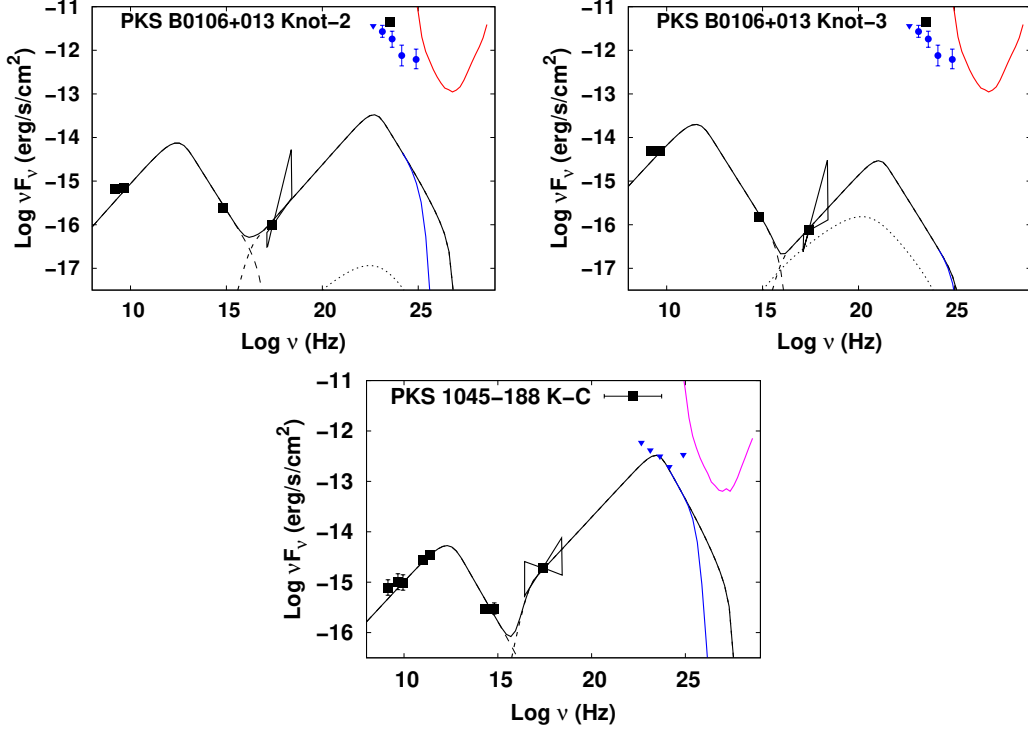


**Figure 6.4:** Fig 6.2 continued

the predicted gamma-ray flux of this knot with the updated *Fermi* upper limits again disfavours the IC/CMB interpretation. Nevertheless, studying this source at VHE will be an additional confirmation to this conjecture or may provide stronger constraints on the emission model if detected.

The second source predicted as a VHE candidate for CTAO under the IC/CMB model is 3C 120 located at  $z=0.033$  is a broad line radio galaxy initially classified as Seyfert I (Sahakyan et al., 2015). The radio morphology of the source is similar to FR I class with radio structures extending up to 100 kpc and superluminal components identified with VLBI studies (Walker et al., 2001, 1987). The X-ray jet consists of four bright knots K4, K7, K25 and K80 and two sections of the jet S 2 and S 3 are bright in X-rays (Harris et al., 1999). The X-ray spectrum for the knot K 7 and the jet component S 3 is steep supporting a synchrotron origin while K 4 and S 2 suggest IC/CMB origin due to hard X-ray spectrum. The knots K 25 and K 80 are not well resolved in optical wavebands (Harris et al., 2004). Hence, in this work we have considered only the knot K 4 and the jet component S 2, and modelled their X-ray emission through the IC/CMB process. Extrapolating this emission model to VHE suggests, that the gamma-ray flux from these regions fall within the 50-hour sensitivity of CTAO. In Fig. 1, we show the model spectrum corresponding to synchrotron and IC/CMB emission processes along with the observed radio–optical–X-ray fluxes. The CTAO sensitivity curve is shown in a red solid line while the *Fermi* gamma-ray upper limits/detections are shown as green colour inverted triangles/solid circles. Though the model curve falls within this *Fermi* upper limits, recent upper limits (blue inverted triangles in Fig. 6.1) derived from 12 years of observation again disfavours the IC/CMB model for this source also (Breiding et al., 2023).

The analytical approximation for the inverse Compton emissivity (equation (6.3.5)) is arrived

Source	<i>Knot</i>	<i>p</i>	<i>q</i>	$R_{knot}$	$\Gamma$	$\theta$	$\gamma_b(10^6)$	$B(10^{-6}G)$
3C 15	K C	2.15	3.60	3.0	6.0	9	0.27	4.10
3C 17	K S3.7	2.30	3.80	5.9	4.0	10	0.39	5.32
3C 17	K S11.3	2.30	4.3	4.5	6.0	10	0.29	7.78
3C 111	K 22	2.25	3.8	4.0	8.0	9	0.44	1.53
3C 111	K 30	2.49	6.0	5.5	4.0	9	5.92	2.34
3C 111	K 61	2.60	4.1	4.4	6.0	9	0.52	3.45
3C 120	K 4	2.61	5.0	3.0	8.0	8	1.68	3.63
3C 120	K S2	2.40	6.0	1.0	7.0	8	4.28	2.32
PKS 1354+195	K S4.0	2.20	3.5	9.0	7.5	11	0.55	6.56
PKS 1354+195	K S5.3	2.40	3.7	3.8	8.0	11	0.13	11.98
3C 346	K C	2.40	4.2	1.8	6.0	9	0.57	15.77
3C 454.3	K A	2.60	4.0	4.0	4.7	4.5	0.13	14.51
3C 454.3	K B	2.60	4.5	2.2	4.7	4.5	0.15	35.50
PKS 2101-490	K K6	2.40	4.3	4.3	6.0	10	0.29	14.63
PKS B0106+013	Knot 1	2.20	4.1	2.0	3.0	13	0.12	44.73
PKS B0106+013	Knot 2	2.01	4.40	3.0	4.0	13	0.10	60.52
PKS B0106+013	Knot 3	2.05	4.40	1.0	2.0	13	0.02	255.75
PKS 1045-188	K C	2.20	4.30	5.0	9.0	8	0.16	6.69

**Table 6.2:** Fit parameters of radio-optical-X-ray spectrum.  $p$  and  $q$  are the power-law indices of particle distribution;  $R_{knot}$  is the radius of the knot in kpc;  $\Gamma$ ,  $\theta$  and  $\gamma_b$  are the bulk Lorentz factor, viewing angle of the jet and break energy of particle spectrum respectively.  $B$  is the magnetic field in the micro-Gauss unit.

considering the scattering process to happen in Thomson regime. However, at VHE the scattering may be inelastic and better described by the Klein-Nishina cross section. In order to investigate this, we draw limits on the target photon energy beyond which the scattering process deviates from the Thomson condition (Ghisellini & Tavecchio, 2009). This happens when the target photon energy measured in the electron rest frame exceeds (or equal to) the rest mass energy (Blumenthal & Gould, 1970). Using this condition along with the scattered photon energy estimated under the Thomson regime, one can arrive at the condition on target photon frequency as (Ghisellini & Tavecchio, 2009; Sahayanathan & Godambe, 2012)

$$\begin{aligned}
\nu^* &\lesssim \frac{1}{\nu(1+z)} \left( \frac{\delta_D}{\Gamma} \right) \left( \frac{mc^2}{h} \right)^2 \\
&\lesssim 10^{14} \left( \frac{\delta_D}{\Gamma} \right) \left( \frac{\nu}{10^{26}} \right)^{-1} \text{ Hz}
\end{aligned} \tag{6.4.1}$$

where,  $\nu^*$  is the frequency of the target photon in the AGN frame,  $\nu$  is the scattered photon (VHE) frequency in the observer frame and  $\delta_D/\Gamma \approx 1.5$  (for  $\Gamma = 4.0$  and  $\theta = 9^0$  corresponding to the knot K 30 of 3C 111). For IC/CMB process the target photon frequency is  $\approx 1.6 \times 10^{11}$  Hz and the

scattering falls within the Thomson regime. Nevertheless, in the numerical code used to reproduce the model spectrum we have considered the exact Klein-Nishina cross section for the IC scattering (Dermer & Schlickeiser, 1993).

The jet components (or knots) considered in this work are located at kilo-parsec scale distances from the AGN core. For instance, the jet components that fall within the detection threshold of CTAO, K 4 and S 2 of 3C 120 are at distances larger than 2.5 kpc from their core (Harris et al., 1999). The knot K 30 of 3C 111 is approximately at a distance of 60 kpc from the core (Claudius et al., 2016). At these large scale distances, the dominant photon field is CMB radiation compared to other photon fields associated with galaxy. Additionally, the relativistic boosting increases the energy density of the CMB in the jet frame by  $\Gamma^2$  while, another external photon field like starlight, thermal infrared radiation from the dusty torus and emission from the accretion disk fall behind the relativistic motion of the emission region and hence, their energy density will be reduced by  $\approx \Gamma^2$  (Begelman et al., 1984). Hardcastle & Croston (2011) has modelled the TeV  $\gamma$ -ray emission from M 87 and Cen A considering inverse Compton scattering of various photon fields by the high-energy electrons responsible for the synchrotron X-rays on kiloparsec scale. However, for this study, they have considered only the inner jet region which falls within a kpc from the core and the contribution of photon fields other than CMB is also substantial.

In this work, we attempt to study the AGN with misaligned jets which are the probable VHE candidates for CTAO. Such misaligned AGN jets have already been studied at VHE and the first significant detection was the FR I source M87 located at a distance 16 Mpc ( $z = 0.0043$ ) (Aharonian et al., 2006). Observations of this source from 2003 till 2006 by H.E.S.S. witness the flux variability in the timescale of a few days. Constraints on the emission region size drawn from this variability timescale suggest the VHE emission to be arising very close to the central engine. The plausible locations are the bright innermost knot HST-1 or the nucleus of M 87. Different emission models have been proposed favouring either of these regions albeit a consensus was never arrived (Rieger & Aharonian, 2008; Lenain et al., 2008; Levinson & Rieger, 2011; Hardcastle & Croston, 2011; Fraija et al., 2012; Rieger, 2012).

The other misaligned AGN which is detected in VHE are Cen A (Aharonian et al., 2009), NGC 1275 (Aleksić et al., 2012), 3C 264 (Holder, 2011), PKS 0625-354 (HESS Collaboration et al., 2018) and IC 310 (Aleksić et al., 2010). An important challenge often encountered while explaining the VHE emission from these sources is the necessity of substantial Doppler boosting. In the case of blazars, the jet is aligned close to the line of sight and hence the emission is significantly Doppler-boosted. This allows the gamma-ray emission to overcome the pair production losses since the rest frame photon energy is less than the observed energy (Dondi & Ghisellini, 1995). In case of misaligned AGN, the Doppler boosting will be minimal due to the large viewing angle of the jet. This introduces strong constraints on the choice of the bulk Lorentz factor of the jet and the viewing angle (Singal, 2016). However, the viewing angle inferred from studying the broadband spectral energy distribution of the source often conflicts with the ones obtained through radio morphological studies (Reynoso et al., 2011; Fujita & Nagai, 2017).

The low energy tail of the electron distribution upscattering the CMB photons to X-ray energies are also responsible for the radio emission through the synchrotron process. This predicts the knots observed at these energy bands to be co-spatial. However, the observed offset between X-ray and radio centroids of the knots from the large-scale jets contradicts this co-spatiality (Reddy et al., 2021). The relatively longer cooling time of low energy electrons also suggests the X-ray emission to be persistent downstream in the jet along with radio. However, in many cases, X-ray emission is localized and do not show continuity similar to radio maps (Harris et al., 2006). These observational features advocate against the IC/CMB interpretation of the X-ray emission.

Another line of evidence challenging IC/CMB is the detection of X-ray counter jet in Pictor A (Hardcastle et al., 2016). The jet counter-jet ratio for this source suggests the jet viewing angle  $\theta < 45^\circ$  and the jet velocity  $v \leq 0.5c$ . The IC/CMB models for the X-ray emission; on the other hand, demands larger jet velocity to boost the CMB photons significantly in the frame of the emission region. Accordingly, smaller viewing angles are also assumed. Similarly, the high degree of X-ray polarisation witnessed in certain knots (Cara et al., 2013), the knot flux variability (Hardcastle et al., 2016) and the deficit of correlation between the ratio of X-ray to radio jet luminosity with the source redshift (Snios et al., 2021) pose strong challenges to the IC/CMB interpretation of the X-ray emission. Observation of the sources 3C 111 and 3C 120 in VHE can further verify this emission model and in addition, provide clues regarding the high energy emission process.

# Chapter 7

## Summary and Recommendations

---

The two decades of *Chandra* X-ray observations led to the discovery of large-scale jets from many powerful quasars. The mechanism responsible for this high energy emission from the extended jets at the kilo-parsec scale is still being debated. The hard X-ray emission from the knots of kpc scale AGN jet is often interpreted as the inverse Compton up-scattering of Cosmic microwave background radiation by relativistic particles in the jet (IC/CMB). However, the gamma-ray upper limits derived from the long-term observation of these sources by *Fermi* disfavour this interpretation.

This thesis focuses on the study of high energy emissions from the large-scale jets of Active Galactic Nuclei. We study the origin of the two-population model of particle distribution to explain the hard X-ray emission associated with the knots/jet of AGN. Considering the advection of particles from the sites of particle acceleration in knots, we explain the origin of two populations. The particle distribution arising from the advected and accelerated regions are different and is capable of explaining the hard X-ray emission from the jets. Besides this, we examine the IC/CMB model for various jets showing hard X-ray behaviour. The emission model is extrapolated to VHE and then compared with the CTAO sensitivity. We explore the possibilities of VHE studies as a tool to validate the emission scenario in the case of large-scale jets of AGN in tandem with the *Fermi* observations. In 7.1 a brief summary of this thesis and in 7.2 recommendations for future research is presented.

### 7.1 Summary

In **Chapter 1** a brief introduction on AGN and their jets extending from parsec to mega-parsec scale distance is presented. **Chapter 2** discusses particle distribution (power law and broken power law) and non-thermal emissions (synchrotron, SSC and IC/CMB) relevant to the work presented in this thesis. This chapter also briefly explains the equipartition magnetic field and gamma-ray attenuation due to EBL absorption.

In **Chapter 3** a detailed review of the recent advancements related to the high energy emission from large-scale jets is presented. This chapter discusses the multi-wavelength observations and theoretical interpretation for the resolved jet. The recent studies relating to implications of *Fermi* observations on the IC/CMB model, the spine-sheath model for interpreting X-ray emission, the positional offset observed between radio-X-ray knots, the X-ray variability and polarisation observation of jets are explained in this chapter. Moreover, recent works and findings on relativistic MHD simulations and VHE emission from large-scale AGN jet also presented.



The recent X-ray and gamma-ray observations of large-scale knots/jets suggest a two-population model for interpreting the MSC emission from large-scale jets. In **Chapter 4** we find the possible origin of two populations considering the advection of particles from the sites of particle acceleration. The results of this work are summarised below:

- By incorporating the advection of accelerated electrons from the sites of particle acceleration, we developed a physically separated two populations of electrons. This distribution is convex (concave upward) in nature and has the potential to explain the hard X-ray emission observed in large-scale jets.
- The synchrotron emission from the combination of accelerated and advected electron distributions can model the radio/optical/X-ray fluxes from all the prominent knots of 3C 273.
- For the chosen combination of the model parameters, the IC/CMB emission associated with the advected and accelerated particle distribution fall within the *Fermi* upper limits.

The X-ray emission from the jet of high redshift sources was interpreted using the IC/CMB model due to the increase in CMB energy density with redshift. This explanation was not examined with *Fermi*  $\gamma$ -ray flux values due to limited observation. The recently estimated  $\gamma$ -ray flux upper limits of two high redshift sources ( $z > 3.5$ ), namely J1510+5702 and J1421-0643, do not comply with the IC/CMB predictions. In **Chapter 5**, we interpret the MSC emission from these two jets using the electron acceleration and advection model presented in the previous chapter. The results of this work are summarised below:

- The synchrotron emission from the composite electron distribution from the regions of acceleration as well as an advected external region is capable of explaining the radio/optical/X-ray emissions from the jets of high redshift sources.
- The IC/CMB spectrum of this composite electron distribution satisfies the constraints drawn from *Fermi* observations.
- The two-population model presented in this work can be better constrained with high-resolution observations at optical wavelengths. Dedicated observation of the high redshift large scale AGN jet, using James Webb Space Telescope, can be of particular interest.

In **Chapter 6**, we performed a detailed multiwavelength modelling of the knots of the AGN jets using the synchrotron and IC/CMB processes. The emission model is extrapolated to VHE and then compared with the CTAO sensitivity. The results of this work are summarised below:

- We find that the VHE model fluxes of certain knots/jet components of two sources, 3C 111 and 3C 120, fall well above the CTAO sensitivity.
- The sources in our study, if detected at VHE, would probably favour the second population interpretation for the high-energy emission rather than IC/CMB because the recently updated *Fermi* upper limits again disfavour the IC/CMB interpretation.

- If IC/CMB is a viable emission process for the X-ray knots, then this suggests many misaligned jets may be potential TeV candidates. Alternatively, VHE studies can also be a tool to validate this emission scenario in tandem with the *Fermi* observations.

## 7.2 Recommendations

The high energy emission mechanisms associated with large scale-scale jets of AGNs are less explored due to various observational limitations. However, the advancements in technology has put forth various open questions yet to be explored.

- The observed positional offset between radio and X-ray intensity peaks in the knot shows emitting regions are not co-spatial. The offset has been observed as different types namely, X-ray upstream of radio (X-f type) and X-ray downstream of radio (R-f type). The proposed two-population model in this thesis can be further modified to explain this observation considering the jet to be cylindrical with differences in advection velocity upstream and downstream of the jet.
- The archival analysis of multiple observations of kiloparsec-scale X-ray jets reports the detection of X-ray variability. This observation contradicts the IC/CMB mechanism and advocates the synchrotron origin of high energy emissions. The electron acceleration and advection model presented in this thesis considers spherical volume with a radius of a few hundred parsecs as the region of particle acceleration and the particles accelerate up to multi-TeV energies and emit via synchrotron mechanism to produce X-rays. These highly energetic electrons, confined to a small emitting volume, can interpret the observed X-ray variability on time scales of months to years (Meyer et al., 2023). The presented model, along with improved observation has the potential to interpret the X-ray variability observed in large-scale jets.
- The combination of multiband imaging and polarimetry can be an effective diagnostic tool for understanding jet emission processes. Even though enormous progress has been made in jet physics through timing and spectral studies, polarimetry can shed light on the magnetic field structures associated with it. With upcoming X-ray polarimetry instruments (eg: IXPE), we can better understand the emission mechanisms associated with AGN jets.
- While most of the recent *Fermi* gamma-ray upper limit estimates on X-ray jets rule out the IC/CMB model, OJ 287 and PKS 151-089 stand exceptional with their minimum-detected gamma-ray flux level in agreement with the IC/CMB model prediction (Meyer et al., 2019). Recently Greenwell et al. (2024) presented the *NuSTAR* observation of a hotspot that coincides with a radio-bright lobe of 4C 74.26. This hard X-ray observation hints the presence of high energy particles even at large-scale distances from the core of the galaxy. Modelling their emission poses real challenges or alternatively, this can also validate the existing models.

- *Fermi*/LAT detected 20 radio galaxies in high energy gamma range. Out of them, 6 were found as VHE emitters. The possible origin of VHE emission from large-scale jets can be further investigated.
- A detailed study on the effects of electron diffusion along with advection on particle distribution can be studied in future.

# Bibliography

- Ackermann M., et al., 2012, *Science*, 338, 1190
- Aharonian F., et al., 2006, *Science*, 314, 1424
- Aharonian F., et al., 2009, *ApJ*, 695, L40
- Ajello M., et al., 2009, *ApJ*, 699, 603
- Aleksić J., et al., 2010, *ApJ*, 723, L207
- Aleksić J., et al., 2012, *A&A*, 539, L2
- Antonucci R., 1993, *ARA&A*, 31, 473
- Atoyan A. M., Aharonian F. A., 1997, arXiv e-prints, pp astro-ph/9711129
- Atoyan A., Dermer C. D., 2004, *ApJ*, 613, 151
- Bañados E., et al., 2015, *ApJ*, 804, 118
- Bañados E., et al., 2016, *ApJS*, 227, 11
- Bai J. M., Lee M. G., 2003, *The Astrophysical Journal*, 585, L113
- Baldi R. D., Capetti A., 2009, *A&A*, 508, 603
- Baldi R. D., Capetti A., Giovannini G., 2015, *A&A*, 576, A38
- Baldi R. D., Capetti A., Massaro F., 2018, *A&A*, 609, A1
- Begelman M. C., Cioffi D. F., 1989, *ApJ*, 345, L21
- Begelman M. C., Blandford R. D., Rees M. J., 1984, *Reviews of Modern Physics*, 56, 255
- Belladitta S., et al., 2020, *A&A*, 635, L7
- Beresnyak A., Jones T. W., Lazarian A., 2009, *ApJ*, 707, 1541
- Berezhko E. G., 1981, *Soviet Journal of Experimental and Theoretical Physics Letters*, 33, 399
- Blandford R. D., Payne D. G., 1982, *MNRAS*, 199, 883
- Blandford R. D., Znajek R. L., 1977, *MNRAS*, 179, 433
- Blandford R., Meier D., Readhead A., 2019, *ARA&A*, 57, 467
- Blumenthal G. R., Gould R. J., 1970, *Reviews of Modern Physics*, 42, 237

Boettcher M., Mause H., Schlickeiser R., 1997, *A&A*, 324, 395

Bonchi A., La Franca F., Melini G., Bongiorno A., Fiore F., 2013, *MNRAS*, 429, 1970

Bragg W., Bragg W., 1962, *The Universe of Light*. Scientific Book Guild, <https://books.google.co.in/books?id=CRGt18q2vnkC>

Breiding P., 2018, PhD thesis, University of Maryland, Baltimore County

Breiding P., Meyer E. T., Georganopoulos M., Keenan M. E., DeNigris N. S., Hewitt J., 2017, *ApJ*, 849, 95

Breiding P., Meyer E. T., Georganopoulos M., Reddy K., Kollmann K. E., Roychowdhury A., 2023, *MNRAS*, 518, 3222

Bromberg O., Levinson A., 2009, *ApJ*, 699, 1274

Burbidge G. R., 1959, *ApJ*, 129, 849

Burns J. O., Price R. M., 1983, *Scientific American*, 249, 50

Cao H. M., Frey S., Gabányi K. É., Paragi Z., Yang J., Cseh D., Hong X. Y., An T., 2017, *MNRAS*, 467, 950

Cara M., et al., 2013, *ApJ*, 773, 186

Carilli C. L., Bartel N., Linfield R. P., 1995, *Astronomy Data Image Library*,

Celotti A., Ghisellini G., 2008, *MNRAS*, 385, 283

Celotti A., Padovani P., Ghisellini G., 1997, *MNRAS*, 286, 415

Chartas G., et al., 2000, *ApJ*, 542, 655

Cheung C. C., 2004, *ApJ*, 600, L23

Clautice D., et al., 2016, *ApJ*, 826, 109

Curtis H. D., 1918, *Publications of Lick Observatory*, 13, 9

Davis S. W., Tchekhovskoy A., 2020, *ARA&A*, 58, 407

Dermer C. D., 1995, *ApJ*, 446, L63

Dermer C. D., Atoyan A., 2004, *ApJ*, 611, L9

Dermer C. D., Menon G., 2009, *High Energy Radiation from Black Holes: Gamma Rays, Cosmic Rays, and Neutrinos*

Dermer C. D., Schlickeiser R., 1993, *ApJ*, 416, 458

Dermer C. D., Schlickeiser R., Mastichiadis A., 1992, *A&A*, 256, L27

Dondi L., Ghisellini G., 1995, *MNRAS*, 273, 583

Dulwich F., Worrall D. M., Birkinshaw M., Padgett C. A., Perlman E. S., 2007, *MNRAS*, 374, 1216

Dulwich F., Worrall D. M., Birkinshaw M., Padgett C. A., Perlman E. S., 2009, *MNRAS*, 398, 1207

Dyrda M., Wierzcholska A., Moderski R., Ostrowski M., Stawarz L., 2015, in 34th International Cosmic Ray Conference (ICRC2015). p. 801 (arXiv:1509.06851), doi:10.22323/1.236.0801

Eddington A. S., 1933, *Nature*, 132, 406

Esch D. N., Connors A., Karovska M., van Dyk D. A., 2004, *ApJ*, 610, 1213

Fan L., Chen W., An T., Xie F.-G., Han Y., Knudsen K. K., Yang J., 2020, *ApJ*, 905, L32

Fanaroff B. L., Riley J. M., 1974, *MNRAS*, 167, 31P

Fermi E., 1949, *Physical Review*, 75, 1169

Fraija N., González M. M., Pérez M., 2012, in Gamma-Ray Bursts 2012 Conference (GRB 2012). p. 131 (arXiv:1212.4424), doi:10.22323/1.152.0131

Franceschini A., Rodighiero G., 2017, *A&A*, 603, A34

Franceschini A., Foffano L., Prandini E., Tavecchio F., 2019, *A&A*, 629, A2

Fujita Y., Nagai H., 2017, *MNRAS*, 465, L94

Georganopoulos M., Perlman E. S., Kazanas D., McEnery J., 2006, *ApJ*, 653, L5

Georganopoulos M., Meyer E. T., Perlman E. S., 2016, *Galaxies*, 4, 65

Ghisellini G., 2000, in Casciari B., Fortunato D., Francaviglia M., Masiello A., eds, *Recent Developments in General Relativity*. p. 5 (arXiv:astro-ph/9905181)

Ghisellini G., 2011, in Aharonian F. A., Hofmann W., Rieger F. M., eds, *American Institute of Physics Conference Series Vol. 1381, 25th Texas Symposium on Relativistic Astrophysics (Texas 2010)*. AIP, pp 180–198 (arXiv:1104.0006), doi:10.1063/1.3635832

Ghisellini G., Svensson R., 1990, in *Baryonic Dark Matter*. pp 395–400

Ghisellini G., Tavecchio F., 2009, *MNRAS*, 397, 985

Ghisellini G., Padovani P., Celotti A., Maraschi L., 1993, *ApJ*, 407, 65

Ginzburg V. L., Syrovatskii S. I., 1964, *The Origin of Cosmic Rays*

Ginzburg V. L., Syrovatskii S. I., 1965, *ARA&A*, 3, 297

Giri G., Vaidya B., Fendt C., 2023, *ApJS*, 268, 49

Godfrey L. E. H., et al., 2012, *ApJ*, 755, 174

Goldschmidt P., Kukulka M. J., Miller L., Dunlop J. S., 1999, *ApJ*, 511, 612

Greenwell C. L., et al., 2024, arXiv e-prints, p. arXiv:2404.17637

HESS Collaboration et al., 2018, *MNRAS*, 476, 4187

Hardcastle M. J., 2018, *MNRAS*, 475, 2768

Hardcastle M. J., Croston J. H., 2011, *MNRAS*, 415, 133

Hardcastle M. J., Birkinshaw M., Worrall D. M., 2001, *MNRAS*, 326, 1499

Hardcastle M. J., Worrall D. M., Kraft R. P., Forman W. R., Jones C., Murray S. S., 2003, *ApJ*, 593, 169

Hardcastle M. J., et al., 2016, *MNRAS*, 455, 3526

Harris D. E., Krawczynski H., 2002, *ApJ*, 565, 244

Harris D. E., Krawczynski H., 2006, *ARA&A*, 44, 463

Harris D. E., Krawczynski H., 2007, in *Revista Mexicana de Astronomia y Astrofisica*, vol. 27. p. 188 (arXiv:astro-ph/0604527), doi:10.48550/arXiv.astro-ph/0604527

Harris D. E., Hjorth J., Sadun A. C., Silverman J. D., Vestergaard M., 1999, *ApJ*, 518, 213

Harris D. E., Mossman A. E., Walker R. C., 2004, *ApJ*, 615, 161

Harris D. E., Cheung C. C., Biretta J. A., Sparks W. B., Junor W., Perlman E. S., Wilson A. S., 2006, *ApJ*, 640, 211

Harris D. E., et al., 2017, *ApJ*, 846, 119

Harrison R., Gottlieb O., Nakar E., 2018, *MNRAS*, 477, 2128

Hillas A. M., 1984, *ARA&A*, 22, 425

Hodges-Kluck E., Gallo E., Ghisellini G., Haardt F., Wu J., Ciardi B., 2021, *MNRAS*, 505, 1543

Holder J., 2011, in *International Cosmic Ray Conference*. p. 137 (arXiv:1111.1225), doi:10.7529/ICRC2011/V12/H11

Hooper E. J., Impey C. D., Foltz C. B., Hewett P. C., 1995, *ApJ*, 445, 62

Hopkins P. F., Richards G. T., Hernquist L., 2007, *ApJ*, 654, 731

Hu Y., Xu S., Stone J. M., Lazarian A., 2022, ApJ, 941, 133

Ighina L., et al., 2021a, arXiv e-prints, p. arXiv:2111.08632

Ighina L., Caccianiga A., Moretti A., Belladitta S., Della Ceca R., Diana A., 2021b, MNRAS, 505, 4120

Ighina L., et al., 2022, A&A, 659, A93

Inoue S., Takahara F., 1996, ApJ, 463, 555

Jester S., Harris D. E., Marshall H. L., Meisenheimer K., 2006, ApJ, 648, 900

Jiang L., Fan X., Ivezić Ž., Richards G. T., Schneider D. P., Strauss M. A., Kelly B. C., 2007, ApJ, 656, 680

Jiang L., et al., 2016, ApJ, 833, 222

Jones F. C., 1968, Physical Review, 167, 1159

Kaiser C. R., Alexander P., 1997, MNRAS, 286, 215

Kardashev N. S., 1962, Soviet Ast., 6, 317

Kataoka J., Stawarz Ł., 2005, ApJ, 622, 797

Kataoka J., et al., 2008, ApJ, 685, 839

Kellermann K. I., Sramek R., Schmidt M., Shaffer D. B., Green R., 1989, AJ, 98, 1195

Kembhavi A. K., Narlikar J. V., 1999, Quasars and active galactic nuclei : an introduction

Kharb P., Lister M. L., Marshall H. L., Hogan B. S., 2012, ApJ, 748, 81

Komissarov S. S., 1999, MNRAS, 308, 1069

Komissarov S., Porth O., 2021, New A Rev., 92, 101610

Kreuzinger M., et al., 2022, ApJS, 260, 49

Kundu E., Gupta N., 2014, MNRAS, 444, L16

Kusunose M., Takahara F., Li H., 2000, ApJ, 536, 299

La Franca F., Gregorini L., Cristiani S., de Ruiter H., Owen F., 1994, AJ, 108, 1548

Lacy M., Laurent-Muehleisen S. A., Ridgway S. E., Becker R. H., White R. L., 2001, ApJ, 551, L17

Leahy J. P., Black A. R. S., Dennett-Thorpe J., Hardcastle M. J., Komissarov S., Perley R. A., Riley J. M., Scheuer P. A. G., 1997, MNRAS, 291, 20



Lenain J. P., Boisson C., Sol H., Katarzyński K., 2008, *A&A*, 478, 111

Levinson A., Rieger F., 2011, *ApJ*, 730, 123

Liu W.-P., Chen Y. J., Wang C.-C., 2015, *ApJ*, 806, 188

Liu R.-Y., Rieger F. M., Aharonian F. A., 2017, *ApJ*, 842, 39

Lucchini M., Tavecchio F., Ghisellini G., 2017, *MNRAS*, 466, 4299

Mannheim K., 1993, *Phys. Rev. D*, 48, 2408

Marchenko V., Harris D. E., Ostrowski M., Stawarz Ł., Bohdan A., Jamrozny M., Hnatyk B., 2017, *ApJ*, 844, 11

Marshall H. L., et al., 2001, *ApJ*, 549, L167

Marshall H. L., Miller B. P., Davis D. S., Perlman E. S., Wise M., Canizares C. R., Harris D. E., 2002, *ApJ*, 564, 683

Marshall H. L., et al., 2010, *ApJ*, 714, L213

Martí J. M., Müller E., Font J. A., Ibáñez J. M. Z., Marquina A., 1997, *ApJ*, 479, 151

Massaro F., Harris D. E., Chiaberge M., Grandi P., Macchetto F. D., Baum S. A., O’Dea C. P., Capetti A., 2009, *ApJ*, 696, 980

Massaro F., Harris D. E., Cheung C. C., 2011, *ApJS*, 197, 24

Massaro F., et al., 2018, *ApJS*, 234, 7

Mazin D., Raue M., 2007, *A&A*, 471, 439

McKeough K., et al., 2016, *ApJ*, 833, 123

Meenakshi M., Mukherjee D., Bodo G., Rossi P., 2023, *MNRAS*, 526, 5418

Meyer E. T., Georganopoulos M., 2014, *ApJ*, 780, L27

Meyer E. T., Georganopoulos M., Sparks W. B., Godfrey L., Lovell J. E. J., Perlman E., 2015, *ApJ*, 805, 154

Meyer E. T., Iyer A. R., Reddy K., Georganopoulos M., Breiding P., Keenan M., 2019, *ApJ*, 883, L2

Meyer E., Roychowdhury A., Georganopoulos M., 2021, in *American Astronomical Society Meeting Abstracts*. p. 238.05

Meyer E. T., et al., 2023, *Nature Astronomy*, 7, 967

Mignone A., Rossi P., Bodo G., Ferrari A., Massaglia S., 2010, *MNRAS*, 402, 7

Miraghaei H., Best P. N., 2017, MNRAS, 466, 4346

Mukherjee D., Bodo G., Mignone A., Rossi P., Vaidya B., 2020, MNRAS, 499, 681

Ndung'u S., Grobler T., Wijnholds S., Karastoyanova D., Azzopardi G., 2023, New Astronomy Reviews, 97, 101685

O'Dea C. P., Owen F. N., 1986, ApJ, 301, 841

Padovani P., 1993, MNRAS, 263, 461

Padovani P., 1997, in Giraud-Heraud Y., Tran Thanh van J., eds, Very High Energy Phenomena in the Universe; Moriond Workshop. p. 7 (arXiv:astro-ph/9704002), doi:10.48550/arXiv.astro-ph/9704002

Padovani P., 2017, Nature Astronomy, 1, 0194

Paliya V. S., Saikia D. J., Domínguez A., Stalin C. S., 2024, arXiv e-prints, p. arXiv:2410.10192

Park J., Algaba J. C., 2022, Galaxies, 10, 102

Perlman E. S., Biretta J. A., Zhou F., Sparks W. B., Macchetto F. D., 1999, AJ, 117, 2185

Perlman E. S., et al., 2011, ApJ, 739, 65

Perlman E. S., Clautice D., Avachat S., Cara M., Sparks W. B., Georganopoulos M., Meyer E., 2020, Galaxies, 8, 71

Perucho M., Martí J. M., 2007, MNRAS, 382, 526

Perucho M., Martí J.-M., Quilis V., 2019, MNRAS, 482, 3718

Pope M. H., Melrose D. B., 1994, PASA, 11, 175

Proctor D. D., 2011, The Astrophysical Journal Supplement Series, 194, 31

Rafter S. E., Crenshaw D. M., Wiita P. J., 2009, AJ, 137, 42

Rahman A. A., Sahayanathan S., Subha P. A., 2022, MNRAS, 515, 1410

Rahman A. A., Sahayanathan S., Malik Z., Subha P. A., 2023, MNRAS, 524, 3335

Rahman A. A., Sahayanathan S., Subha P., 2024a, Journal of High Energy Astrophysics, 42, 156

Rahman A. A., Sahayanathan S., Subha P. A., 2024b, PoS, HEPROVIII, 017

Razzaque S., Dermer C. D., Finke J. D., 2009, ApJ, 697, 483

Reddy K., Georganopoulos M., Meyer E. T., 2021, ApJS, 253, 37

Reddy K., Georganopoulos M., Meyer E. T., Keenan M., Kollmann K. E., 2023, *ApJS*, 265, 8

Rees M. J., 1966, *Nature*, 211, 468

Reynoso M. M., Medina M. C., Romero G. E., 2011, *A&A*, 531, A30

Rieger F. M., 2012, in Aharonian F. A., Hofmann W., Rieger F. M., eds, *American Institute of Physics Conference Series Vol. 1505, High Energy Gamma-Ray Astronomy: 5th International Meeting on High Energy Gamma-Ray Astronomy*. pp 80–87 (arXiv:1210.6847), doi:10.1063/1.4772223

Rieger F. M., 2019, *Galaxies*, 7, 78

Rieger F. M., Aharonian F. A., 2008, *A&A*, 479, L5

Rieger F., Levinson A., 2018, *Galaxies*, 6, 116

Rieger F. M., Bosch-Ramon V., Duffy P., 2007, *Ap&SS*, 309, 119

Rulten C., 2022, *Galaxies*, 10, 61

Rybicki G. B., Lightman A. P., 1986, *Radiative Processes in Astrophysics*

Sahakyan N., Zargaryan D., Baghmany V., 2015, *A&A*, 574, A88

Sahayanathan S., 2008, *MNRAS*, 388, L49

Sahayanathan S., Godambe S., 2012, *MNRAS*, 419, 1660

Sahayanathan S., Misra R., Kembhavi A. K., Kaul C. L., 2003, *ApJ*, 588, L77

Sahayanathan S., Sinha A., Misra R., 2018, *Research in Astronomy and Astrophysics*, 18, 035

Sambruna R. M., Urry C. M., Tavecchio F., Maraschi L., Scarpa R., Chartas G., Muxlow T., 2001, *ApJ*, 549, L161

Sambruna R. M., Maraschi L., Tavecchio F., Urry C. M., Cheung C. C., Chartas G., Scarpa R., Gambill J. K., 2002, *ApJ*, 571, 206

Sambruna R. M., Gambill J. K., Maraschi L., Tavecchio F., Cerutti R., Cheung C. C., Urry C. M., Chartas G., 2004, *ApJ*, 608, 698

Sbarrato T., Ghisellini G., Tagliaferri G., Foschini L., Nardini M., Tavecchio F., Gehrels N., 2015, *MNRAS*, 446, 2483

Sbarrato T., Ghisellini G., Tagliaferri G., Tavecchio F., Ghirlanda G., Costamante L., 2022, *A&A*, 663, A147

Schmidt G. D., Peterson B. M., Beaver E. A., 1978, *ApJ*, 220, L31

Schwartz D. A., 2002, ApJ, 569, L23

Schwartz D. A., 2020, in IAU General Assembly. pp 53–60 (arXiv:1901.00462), doi:10.1017/S1743921319003454

Schwartz D. A., et al., 2000, ApJ, 540, 69

Schwartz D. A., et al., 2006, ApJ, 647, L107

Schwartz D. A., et al., 2020, ApJ, 904, 57

Shastri P., Wilkes B. J., Elvis M., McDowell J., 1993, ApJ, 410, 29

Shen X., Hopkins P. F., Faucher-Giguère C.-A., Alexander D. M., Richards G. T., Ross N. P., Hickox R. C., 2020, MNRAS, 495, 3252

Shu F. H., 1991, The physics of astrophysics. Volume 1: Radiation.

Siemiginowska A., Smith R. K., Aldcroft T. L., Schwartz D. A., Paerels F., Petric A. O., 2003, ApJ, 598, L15

Siemiginowska A., Stawarz Ł., Cheung C. C., Harris D. E., Sikora M., Aldcroft T. L., Bechtold J., 2007, ApJ, 657, 145

Sikora M., Begelman M. C., Rees M. J., 1994, ApJ, 421, 153

Singal A. K., 2016, ApJ, 827, 66

Snios B., et al., 2021, ApJ, 914, 130

Snios B., et al., 2022, ApJ, 934, 107

Stanev T., Franceschini A., 1998, ApJ, 494, L159

Stanley E. C., Kharb P., Lister M. L., Marshall H. L., O’Dea C., Baum S., 2015, ApJ, 807, 48

Stecker F. W., de Jager O. C., 1993, ApJ, 415, L71

Stein N. M., van Dyk D. A., Kashyap V. L., Siemiginowska A., 2015, ApJ, 813, 66

Stoche J. T., Morris S. L., Weymann R. J., Foltz C. B., 1992, ApJ, 396, 487

Strittmatter P. A., Hill P., Pauliny-Toth I. I. K., Steppe H., Witzel A., 1980, A&A, 88, L12

Stuardi C., et al., 2018, ApJS, 235, 32

Sun X.-N., Yang R.-Z., Rieger F. M., Liu R.-Y., Aharonian F., 2018, A&A, 612, A106

Sunder Sahayanathan B., 2011, arXiv e-prints, p. arXiv:1109.0618

Swain M. R., Bridle A. H., Baum S. A., 1998, *ApJ*, 507, L29

Tavecchio F., 2021, *MNRAS*, 501, 6199

Tavecchio F., Ghisellini G., 2015, *MNRAS*, 451, 1502

Tavecchio F., Maraschi L., Ghisellini G., 1998, *ApJ*, 509, 608

Tavecchio F., Maraschi L., Sambruna R. M., Urry C. M., 2000, *ApJ*, 544, L23

Tavecchio F., Maraschi L., Wolter A., Cheung C. C., Sambruna R. M., Urry C. M., 2007, *ApJ*, 662, 900

Toda K., Fukazawa Y., Inoue Y., 2020, *ApJ*, 896, 172

Turner R. J., Shabala S. S., 2015, *ApJ*, 806, 59

Uchiyama Y., et al., 2006, *ApJ*, 648, 910

Urry C. M., Padovani P., 1995, *PASP*, 107, 803

Wakely S. P., Horan D., 2008, in *International Cosmic Ray Conference*. pp 1341–1344

Walker R. C., Benson J. M., Unwin S. C., 1987, *ApJ*, 316, 546

Walker R. C., Benson J. M., Unwin S. C., Lystrup M. B., Hunter T. R., Pilbratt G., Hardee P. E., 2001, *ApJ*, 556, 756

Wals M., Boyle B. J., Croom S. M., Miller L., Smith R., Shanks T., Outram P., 2005, *MNRAS*, 360, 453

Wang Z.-J., Zhang J., Sun X.-N., Liang E.-W., 2020, *ApJ*, 893, 41

Weisskopf M. C., et al., 2022, *Journal of Astronomical Telescopes, Instruments, and Systems*, 8, 026002

White R. L., et al., 2000, *ApJS*, 126, 133

Wilson A. S., Young A. J., Shopbell P. L., 2001, *ApJ*, 547, 740

Worrall D. M., 2009, *A&A Rev.*, 17, 1

Worrall D. M., Birkinshaw M., 2005, *MNRAS*, 360, 926

Worrall D. M., Birkinshaw M., Marshall H. L., Schwartz D. A., Siemiginowska A., Wardle J. F. C., 2020, *MNRAS*, 497, 988

Wu J., Brandt W. N., Miller B. P., Garmire G. P., Schneider D. P., Vignali C., 2013, *ApJ*, 763, 109

Xue Z.-W., Zhang J., Cui W., Liang E.-W., Zhang S.-N., 2017, *Research in Astronomy and Astrophysics*, 17, 090

Yang J., Wang J., 2010, *A&A*, 522, A12

Yang X., et al., 2022, *ApJ*, 933, 98

Yuan W., Fabian A. C., Celotti A., Jonker P. G., 2003, *MNRAS*, 346, L7

Zhang J., Bai J. M., Chen L., Liang E., 2010, *ApJ*, 710, 1017

Zhang J., Xue Z.-W., He J.-J., Liang E.-W., Zhang S.-N., 2015, *ApJ*, 807, 51

Zhang J., Du S.-s., Guo S.-C., Zhang H.-M., Chen L., Liang E.-W., Zhang S.-N., 2018, *ApJ*, 858, 27

Zhang Y., An T., Frey S., Gabányi K. É., Sotnikova Y., 2022, *ApJ*, 937, 19

Zhu S. F., Brandt W. N., Wu J., Garmire G. P., Miller B. P., 2019, *MNRAS*, 482, 2016